The Hashemite Kingdom of Jordan Scientific Research Support Fund The Hashemite University

JJEES

Jordan Journal of Earth and Environmental Sciences

Volume (13) Number (4)

Cover photo © Prof. Eid Al Tarazi

JJEES is an International Peer-Reviewed Research Journal

ISSN 1995-6681 jjees.hu.edu.jo December 2022

Jordan Journal of Earth and Environmental Sciences (JJEES)

JJEES is an International Peer-Reviewed Research Journal, Issued by Deanship of Scientific Research, The Hashemite University, in corporation with, the Jordanian Scientific Research Support Fund, the Ministry of Higher Education and Scientific Research.

Submission address:

Manuscripts should be submitted electronically to the following e-mail:

jjees@hu.edu.jo

For more information and previous issues:

www.jjees.hu.edu.jo

Hashemite Kingdom of Jordan

Scientific Research Support Fund

Hashemite University

Jordan Journal of Earth and Environmental Sciences

JJEES

An International Peer-Reviewed Scientific Journal

Financed by the Scientific Research Support Fund

Volume 13 Number (4)

http:// jjees.hu.edu.jo/

ISSN 1995-6681

*Water Recharge, Natural Groundwater Harvesting, Wadi Deir Al Kahef, near Tal Hassan Volcano, Northeast Jordan.
Photographed by Prof. Eid Al Tarazi

JJEES

JJEES (2022) 13 (4): 232-241
ISSN 1995-6681

Jordan Journal of Earth and Environmental Sciences

Historic Management of the Dynamic Landscape in the Surroundings of Petra, Jordan

Nizar Abu-Jaber[1*], Catreena Hamarneh[2],
Mohammad Al Farajat[3], Abdulla Al-Rawabdeh[4] and Sahar al Khasawneh[5]

[1] Center for the Study of Natural and Cultural Heritage, German Jordanian University
[2] German Protestant Institute for Archaeology in Amman
[3] Department of Archaeology, Al Hussein Bin Talal University
[4] Department of Earth and Environmental Sciences, Yarmouk University
[5] Department of Conservation and Management of Cultural Resources, Yarmouk University

Received 6th February 2022; Accepted 28th March 2022

Abstract

Terracing and the construction of a flood control system in Petra has allowed a unique opportunity to examine landscape conditions and changes beginning with the Late Iron Age. The study area is the Hremiyyeh catchment that flows into the core of the archaeological city of Petra and therefore constitutes an important key to understanding the human settlement of the area. The location was chosen as a focal point for intensive investigation and the study of human response to environmental change. This study involved careful documentation of the topography, geology, and archaeology of the site. In addition, samples were taken for the dating of terrace construction and changes in the landscape. The study indicates that the hydrological interventions began in the Late Iron Age, and intensified during the Nabataean and Early Roman periods. At the time, some of the drainage areas were already deeply gullied, while other parts had recently accumulated sediments. The lower terraces became filled with water-logged sediments, leading to the deposition of carbonates. The upper terraces changed the drainage pattern and deposition of the sediments. The sediments trapped there seem to have been less water-logged. The abandonment of the system at the end of the Byzantine to Early Islamic periods led to partial collapses, gullying, and bedrock downcutting. Due to soil accumulation, the upper terraces were restored and enhanced with new ones around the 11th. Century CE, probably due to partial reclamation of the area by nomadic settlers, with charred botanical evidence found indicating the burning of wild vegetation in favor of domesticated cereal and legumes, with relatively humid conditions.

Keywords: *Petra; Jordan; Landscape evolution; Human Responses; climate*

1. Introduction

The area of Petra in southern Jordan (Figure 1) is a tectonically and climatically challenging place for a major urban and trade center. Specifically, the area is characterized by an arid climate, high relief, flash floods, and earthquakes. Despite this, the area has been well harnessed since the Edomite (Iron Age II) period onwards (Bienkowski, 2013), with the local environment providing water, food, and other necessities for human habitation with sufficient control of the natural hazards that characterize the dynamic landscape.

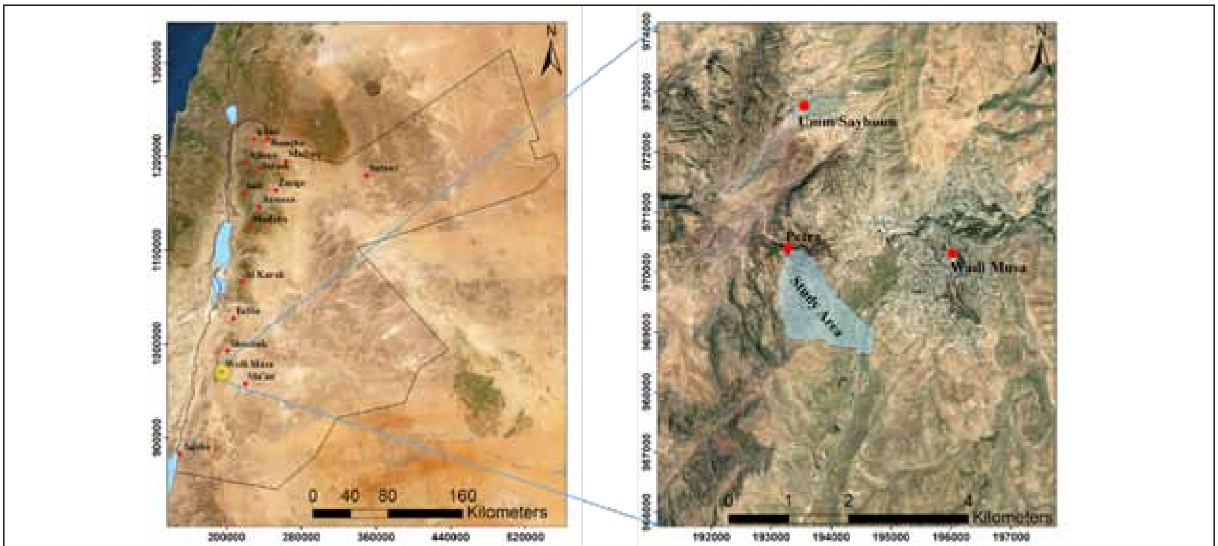

Figure 1. Location of the study area concerning Petra and Wadi Musa.

* Corresponding author e-mail: nizar.abujaber@gju.edu.jo

Historic Petra has witnessed significant environmental changes over the last three millennia. Three factors have led to this change, i.e. climate fluctuations, tectonic movements, and anthropogenic interventions. These can be detected through the architectural landscape, where humans intervened by building water management and soil control features, better known as terraces. Terraces store climatic, topographic, and agricultural evidence through their very presence as well as in the sediments accumulated behind them. Moreover, they also provide potential clues to more sustainable management approaches for flood control, soil protection, and agriculture, even under different prevailing sociopolitical and economic conditions.

Recently, researchers have addressed various aspects of environmental change in the Petra area. It has been shown that a lacustrine environment prevailed in the area in the late Pleistocene and the early Holocene, and subsequent tectonism in the area changed the drainage pattern from a southerly direction to a westerly one (Abu-Jaber et al, 2020a). Hamarneh (2022) has surveyed the variety of terraces in Petra, discussing their ages, functions, and aspects of their environmental imperatives. Varieties in terrace function reflect site-specific priorities and included objectives such as flood control (Al Qudah et al., 2016; Abdelal et al., 2021), agriculture (Kouki, 2012), water collection, soil conservation and infrastructure protection (Hamarneh, 2022). Moreover, materials collected behind the terrace walls can contain important climatological materials that can help understand land-use practices in the past (Hamarneh, 2022, Bäumler, 2020).

The slopes and valleys around the ancient Nabataean city of Petra are heavily covered by terraces. These terraces were not constructed all at the same time but do reflect human response and adaptation to the concurring environmental events, mainly droughts, landslides, or floods.

1.1 Terraces as proxies for dynamicity:

Terraces are man-made dry walls constructed from natural stones without the use of any binding material to preserve and accumulate soil, mitigate flooding, and expand agrarian activities on steep slopes (Spencer and Hale, 1961; Treacy and Denevan, 1994). Terraces are sometimes built on bedrock, but more often they are built on accumulated soil or constructed to confine accumulated soil. In some areas, the soil was brought from other locations and dumped behind terrace walls. In such cases, the nature of the soil, and the dip of the accumulated layers can lead to the understanding of the history of the fill (Frederick and Krahtopoulou, 2000). Naturally accumulated soil fill might contain other evidence of practiced activities, surrounding ecology, and environmental conditions. Thus, part of the archival nature of terraces is encapsulated in the sediments and soils accumulated behind the terrace walls.

Terrace foundation elevations mark the location of the ground levels at the time of construction. And while the discussion may occur about how much change has occurred to the ground level behind the terrace wall (i.e. is the soil older than the terrace or not), the fronts of terraces certainly mark the ground levels at the time of construction. Thus, the down cutting of the stream level in front of the wall is clear evidence of the stream down cutting and back cutting that occurred since the structure was built. The ages of the sediments below, in front of and behind the terraces, differ, reflecting the sequence of events. While the soil behind the terraces remains sealed, with disturbances occurring only in the topsoil, the soil under the terrace riser remains sealed as long as the riser wall remains intact, unlike the soil in front of the riser which can be washed away, re-deposited, or cut into. Moreover, it is possible to determine the locations of terraces that have been destroyed using characteristic carbonate deposits that were left behind (Abu-Jaber et al., 2020b). Thus, it is possible to determine stream level elevation drops based on downcutting into these carbonates and underlying bedrock.

Terrace construction location, the longevity of exploitation, expansion, and abandonment patterns can be considered to be responses to prevailing conditions, especially when the study of these patterns is combined with analysis of accumulated sediments and their trapped paleoclimatic and paleoenvironmental proxies. Thus, even when another cultural material is lacking (such as monumental buildings), terraces can provide a wealth of evidence on prevailing conditions at the times of their building and exploitation. Furthermore, their sturdy and stable walls have made them ideal proxies in various parts of the world for studying the history of anthropogenic landscapes (Kiesow and Bork, 2017). And since these terraces in Petra extend in time from the Iron Age until now, much might be learned from studying them.

The evolution of human settlement patterns and changes in human daily activity were generally used as indicators of changes in climatic conditions. However, this is too simplified an explanation as socioeconomic and political factors influence human settlements (Jones et al., 2019). After undertaking an intensive survey in the area of Petra, the drainage basin of Hremiyyeh was selected for a detailed study (Figure 2). This includes the determination of the ages of human interventions in the area, changes in geomorphology as evidenced by carbonate deposits, down cutting, and terrace collapse, and changes in the vegetative cover through the study of plant remains (phytoliths). This study aims to show how a detailed examination of these terraces can increase understanding of their construction as responses to changes in environmental conditions through time.

1.2 The study area

Petra lies in the south of Jordan along the margin of the Dead Sea transform fault. The tectonism in the area affected a lithological sequence that spans from the Precambrian basement rock through the Late Cretaceous carbonate shallow marine platform rocks (Barjous, 2003). This tectonism began with epeirogenic uplift in the Late Eocene or Early Oligocene and continues throughout the Quaternary in the form of uplift, folding, faulting, and volcanism (Barjous and Mikbel, 1990). This now manifests in a series of sub-parallel normal faults and remnant rift basins that generally trend NNE-SSW. This is called the Quwayra Fault Zone (Barjous, 2003), and part of this zone includes the Wadi Musa fault.

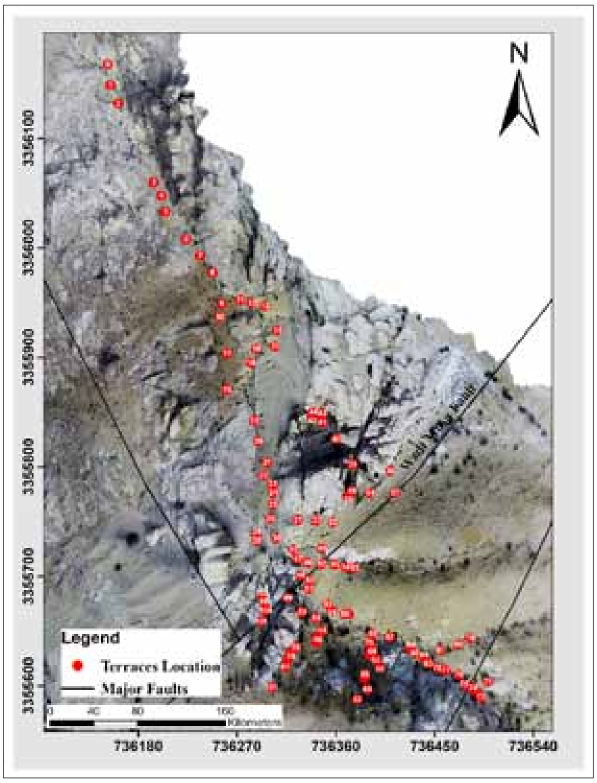

Figure 2. Wadi Hremiyyeh, showing the distribution of terraces, as well as the faults cutting through the area.

The drainage basin of Wadi Hremiyyeh, which was examined in this study, is on the eastern margin of the Dead Sea rift zone, with the Wadi Musa Fault cutting through it. The lower part of the drainage basin consists of Palaeozoic sandstone deposits (Red-varicolored Cambrian Umm Ishrin Sandstone overlain by white Ordovician Disi Sandstone; Barjous, 2003) and the Pleistocene lacustrine deposits in the lower (western) sections (Abu-Jaber et al., 2020a). Lower Cretaceous Kurnub Sandstone and Upper Cretaceous marine limestone and marl sequences crop out to the east of the fault (Figure 3). In addition, overlying undated Quaternary alluvium and colluviums are seen in the upper (eastern) sections (Barjous, 2003).

Thus, the Quaternary deposits include Pleistocene and Holocene colluvium, gravel, and soils on the slopes overlooking Petra (Barjous, 2003), as well as fluvio-lacustrine deposits within the main rift basin at the lower elevations below the 1060 masl contour line (Abu-Jaber et al., 2020a). Recent deposits also include a variety of terrestrial carbonates (Abu-Jaber et al., 2020b) and occasionally significant loess deposits, particularly related to abandoned archaeological sites (Lucke et al., 2019a,b).

The area is within the Qwaira fault zone, mostly a segment called the Wadi Musa Fault which runs NS, and defines a boundary between Palaeozoic Sandstone to the west and the Upper Cretaceous marine limestones and marls to the east. It also marks a break in the topography and the beginning of a steeper slope.

A group of springs issued from the Upper Cretaceous limestone formations in the upper reaches of the basin. Recharge occurs in the upper Ash-Sharah Mountain Plateau, and springs are mostly situated at the cliffs overlooking Petra (Al-Farajat and Salameh, 2010). The natural course of the permanent water flow from Braq spring (at 1300 masl) above Wadi Hremiyyeh is through the Hremiyyeh stream, although the spring has now dried up. A Nabataean estate (Dalman, 1908; Tholbecq et al., 2018), complete with a significant set of agricultural terraces that control water flow and soil movement lies there. A Nabataean aqueduct connected the spring water from Braq to the center of Petra to Qasr il Bent (Dalman, 1908; Lindner and Hübl, 1997; Bellwald, 2008).

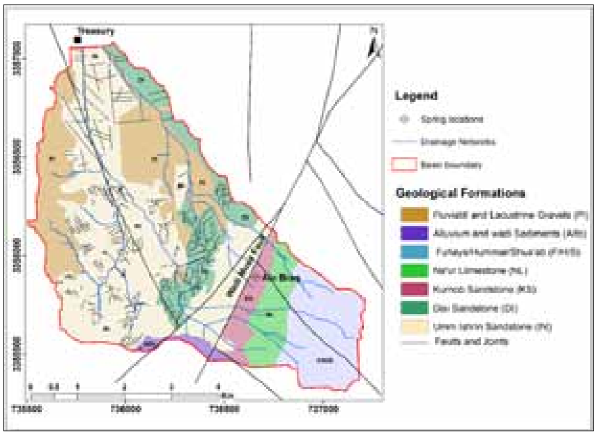

Figure 3. Geology of the study area (After Barjous, 2003).

A cliff within this segment of the tributary within the higher Upper Cretaceous limestone outcrops drops the elevation down to a ledge at 1300 masl, upon which a modern highway links Wadi Musa with At-Tayyiba. This highway has caused the diversion of most of the upstream runoff from the Braq/Hremiyyeh tributary to the adjacent Wadi Al-Madras tributary (and then to the Siq). Immediately below the ledge, the elevation continues the drop-down to the level of the Wadi Musa fault (1100 masl; Figure 4).

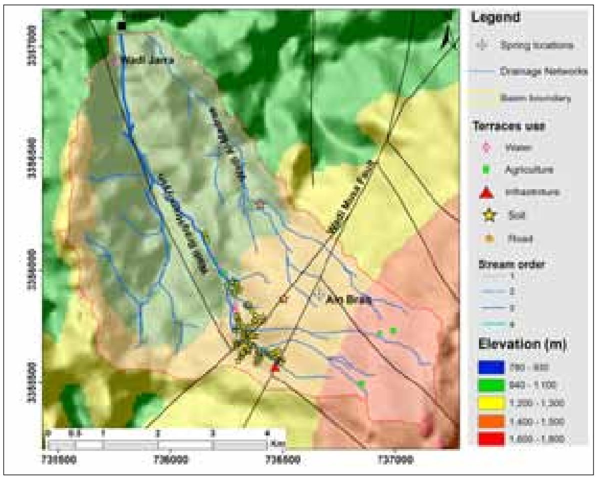

Figure 4. Topography of the study area (modified after Royal Jordanian Geographic Center).

2. Materials and Methods

A multi-disciplinary approach was used to understand the climate/tectonic/human nexus in the area. Intensive geological, hydrological, geomorphological, and archaeological surveys were conducted in the study area, coupled with soil samples gathering for texture, phytolith, and dating purposes.

2.1 Archaeology

An intensive survey of the terrace typology, method of construction, and distribution within the landscape, including spatial analysis, was conducted. Each terrace was drawn, recorded by GPS points, and described. Cultural material in association with the terraces (pot sherds) was collected, studied, and drawn.

2.2 Geomorphology

Under the geographic information system environment (GIS), a geodata base was established to organize and manage the enormous field surveys. The collected dataset contains the terraces' location using real kinematic GNSS (RTK), terrace types and usages as well as geological and hydrological information. This digital geodata base and all the necessary mapping were used to understand the geographical distribution relationship between the terrain elevation, geology, drainage, and terraces.

The watershed morphometric analysis of this study was based on the derived DEM with a spatial resolution of 2m as extracted from airborne Light detection and ranging (LiDAR), Royal Jordanian Geographic Centre (RJGC), for the selected study area. This was calibrated and referenced against a drone survey of the lower part of the drainage of Wadi Hremiyyeh. This allowed for the determination of the locations of the terraces, and the location and extent of gullying, undercutting, and carbonate deposits allowing for the inferring of how the landscape changed through time.

2.3 Soil

A recently vandalized terrace (terrace 90) at the site exposed a well-preserved burnt organic-rich horizon which allowed for the identification of botanical remains. Laboratory examination of samples obtained from the horizon provided data on seeds, pollens, and phytoliths. Phytolith separation was done using heavy liquids, whereas the seeds were separated using floatation. The pollens were extracted through chemical digestion. All of the extraction and identification of botanical remains were done at the Phytolith Research Institute in Pune, India.

In addition, samples were taken for ^{14}Cdating of charcoal from the same horizon. This was analyzed at the AMS of the A.E. LaLonde Laboratory at the University of Ottawa in Canada. Sample preparation for CO_2 purification and graphitization was conducted using the equipment and protocols outlined by (St-Jean et al., 2017). Analysis was conducted using a High Voltage Engineering (HVE) 3MV Tandem Accelerator Mass Spectrometer.

2.4 OSL ages

Conventional luminescence dating technique was applied to sediment deposits near terraces' walls in Wadi Hremiyyeh. Two sediment samples were collected from a trench dug in the slope of the wadi Hremiyyeh site (WHr1 and WHr2) at depths 50 and 80 cm. another sample was taken from a trench dug 40 cm below the former (WHr3) (Figure 5). The three samples fill at depths 50, 80, and 100 cm respectively form the surface of the first trench. The samples are assumed to represent the sediment deposited gradually by water wash along the slope of the Wadi. Water wash is expected to give full bleaching of the OSL signal before deposition. Any post-deposition disturbance will be observed by the scattering of the ages or existing age inversions. Samples were taken using metal tubes inserted horizontally in the trenches' sections. For each sample, another 200 g of sediments were taken for the environmental dose rate measurements.

Figure 5. Pits excavated for OSL dating at terrace 6.

The samples were chemically treated using 10% HCl and 30% H_2O_2 to remove calcites and organics respectively. 40% HF was used to remove any feldspars and remove the alpha outer shell for sand-sized quartz grains. Luminescence measurements and equivalent doses estimation were carried out using Risø TL/OSL reader (Model TL-DA20) equipped with blue LEDs emitting at 470 nm (~80mW.cm^{-2}) and calibrated $^{90}Sr/^{90}Y$ beta source delivering 0.076 Gy.s^{-1}. The luminescence signals were detected through a 7.5 mm Hoya U-340 glass filter (pass band centered on 370 nm) (Meyer et al., 2020).

Quartz luminescence signals were dominated by fast components, as shown in Figure 6 (Thomsen et al., 2008; Jain et al., 2003). Quartz equivalent doses (D_e) were estimated using the single-aliquot regenerative dose (SAR) protocol (Hansen et al., 2015). The suitability of the SAR protocol was tested using both dose recovery tests and internal performance checks. The dose recovery test was performed by bleaching twice the luminescence signals for 18 aliquots at room temperature and using blue light and intervening 10ks pause. A given dose of 15.2 Gy was given to the aliquots. SAR protocol was then applied to all aliquots using preheat/ cut the heat of 220/180 ^{o}C. The dose recovery ratio between the measured dose and the given dose was 1.021±0.007 (n=18). This proves the suitability of SAR protocol to accurately measure a known dose before any thermal treatment, therefore, all D_e estimates were measured using SAR with preheat/ cut the heat of 220/180 ^{o}C. The thermal transfer was almost negligible for the three samples (0.007±0.003 (n=9; 3 aliquots each sample). During D_e estimates, the average recycling ratio was within 10% of unity (1.018±0.011, (n=36)). The average recuperation value was ((3.5±1)%, n=36) (Murray and Wintle, 2003; Wintle and Murray, 2006).

Dose rates were measured by determining radionuclide concentrations (^{238}U, ^{232}Th, ^{226}Ra, and ^{40}K) using high-resolution gamma spectrometry. The radionuclides concentrations were then converted to infinite matrix dose rates using the updated conversion factors of Guérin et al. (2011). An internal alpha dose rate contribution of 0.020±0.002 Gy/ka in quartz (Vandenberghe et al., 2008). The cosmic dose rate was calculated following (Prescott and Hutton, 1994) an uncertainty of 5%.

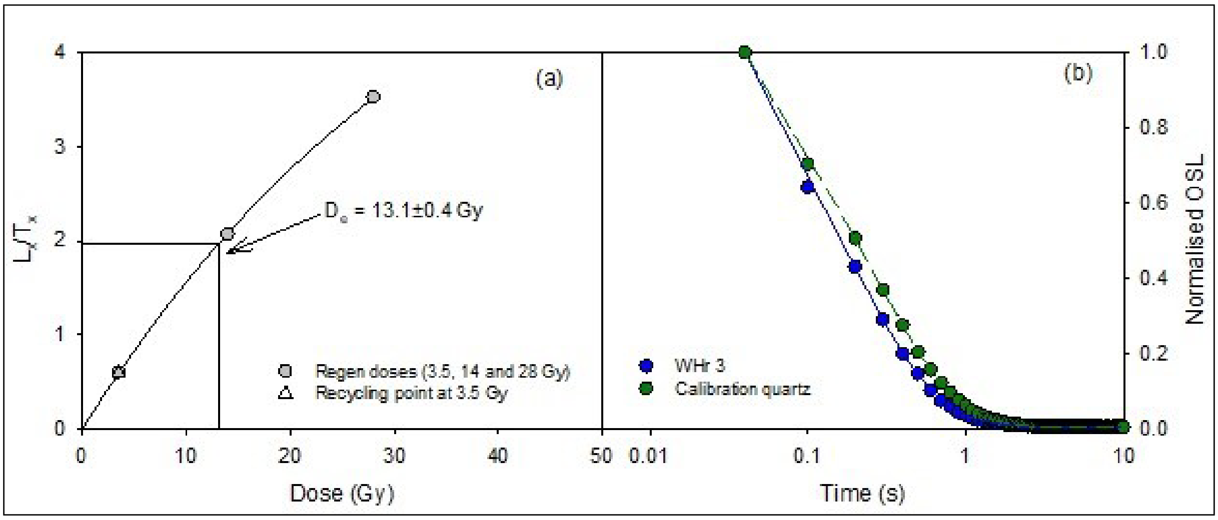

Figure 6. (a) Representative dose-response curves showing the regen doses and interpolated De for sample WHr3. (b) a typical stimulation curve for the same sample (blue continuous line) compared to a normalized stimulation curve from calibration quartz (green dashed line) using preheat/ cut the heat of 220/180 °C.

2.5 Ground Penetrating Radar

Behind terrace 88 (the upper part of the study area) a large flat area was excavated surrounded by a set of terraces to the east, south, and north (Figure 7). This area was dissected at the southeastern side by a gully and a cliff on its southwestern side. Sediment accumulation and stratigraphy were examined using a Ground Penetrating Radar (GPR) to attempt to elucidate the soil slope before the building of the terraces and to reconstruct the relationship between terrace construction and existing soil strata.

Figure 7. Lines of the GPR survey.

3. Results

A sypsometric curve allows for the understanding of the erosion state of the watershed and is used to infer the stage of development of the drainage network. Here the hypsometric curve approaches the so-called maturity stage, at least according to this degree erosion classification associated with the age of the basin (Figure 8). The Wadi Hremiyyeh hypsometric integral value is 0.37. Hypsometric integrals vary from 0 to 1, with values close to 0 being in highly eroded regions and values close to 1 in slightly eroded regions (Sarp et al., 2011; Pedrera et al., 2009).

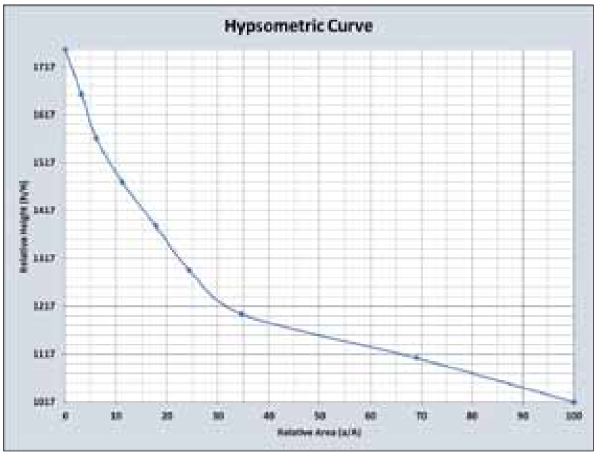

Figure 8. A hypsometric graph for Wadi Hremiyyeh. The slope break at the relative area of 37 indicates shows intermediate levels of geomorphic evolution.

The scatter pottery helped give an overall assessment of human exploitation of the studied landscape. This analysis allows relative dating as well as understanding the nature of landscape use during different periods. Figure 9 shows some of the pottery types found in the area.

The pottery sherds showed an even distribution of the surface, with a very high concentration of pottery in the middle catchment area (around terraces 29, 30). A small number of sherds were of the Iron Age II mainly around terraces 72, 73,74,76, and 84, while the dominant sherds were of E Nabataean period, with an equal amount of L Nabataean to E. Roman periods, with a very small amount of E Byzantine. Fragments of Mamluk common ware pottery were concentrated in the upper catchment area mainly in the western area around terraces (29, 30, 49, 104, 105), with a clear absence of pottery from any other Islamic periods.

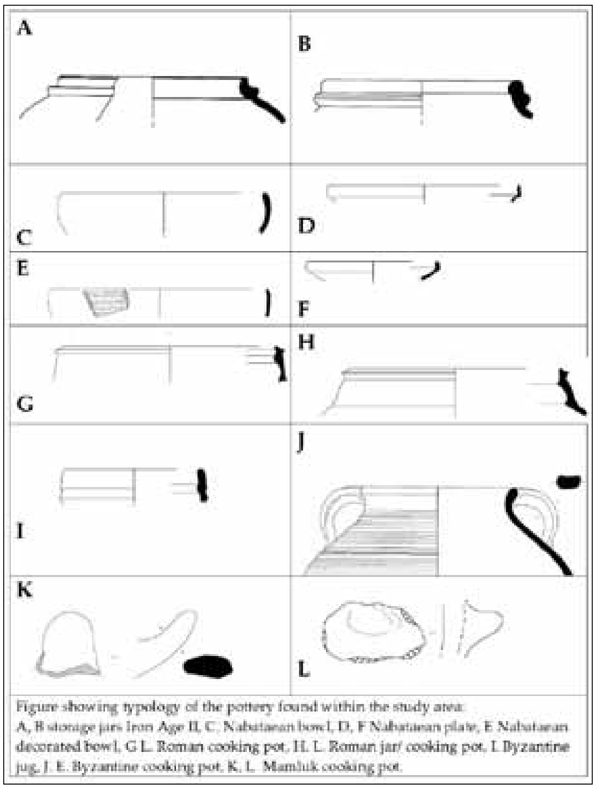

Figure 9. Pottery types found at Wadi Hremiyyeh.

The area under consideration consists of two tributary branches that merge near terrace 30. The northern branch is smaller, yet contains several terraces (46, 52, and 95). The southern branch contains larger and more numerous terraces (49-88). In addition, the soil cover between the two branches contains a few terraces as does the southern slope that drains into the southern branch. Undercutting is seen under all of the terraces (check dams) that cross the two branches but is less clear on the slopes and in the area between them. Beyond the confluence of the branches at terrace30 (at the Wadi Musa Fault), there is evidence of both downcutting as well as carbonate deposits related to the terraces. However, the extent of the downcutting is less pronounced, as the entire slope becomes more gentle. Figure 10 shows three examples of profiles across the wadi in front of the terraces. Terrace 5 is in the lower part of the catchment, and shows slightly less than 1 m of downcutting below the terrace. Similarly, terrace 13 shows little downcutting in front of the terrace. By contrast, terrace 89 shows almost 3 m of downcutting, clearly showing a more dynamic segment of the drainage basin.

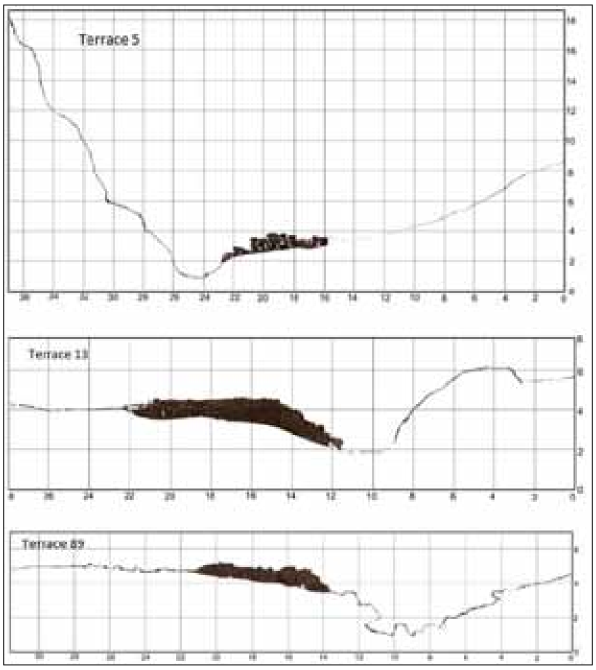

Figure 10. Profiles extracted from the 3-D scanning of the terrace system, showing the extent of downcutting below the terraces in the lower (terrace 5), middle (terrace 13), and upper (terrace 89) parts of the drainage area, All dose rate information, D_e, and calculated ages are summarized in Table 1.

Table 1. Details of the OSL measurements from the three samples behind terrace 6.

Sample	Water content	Depth (cm)	^{238}U (Bq/kg)	^{226}Ra (Bq/kg)	^{232}Th (Bq/kg)	^{40}K (Bq/kg)	γ dose rate (Gy/ka)	β dose rate (Gy/ka)	Dose rate (Gy/ka)	D_e (Gy)	Age (Ka)
WHr1	1.6	50	25±9	14.8±0.8	15.9±0.8	200±9	0.45±0.02	0.76±0.03	1.36±0.06	200±9	2.5±0.2
WHr2	2.3	80	17±6	17.2±0.5	14.9±0.5	141±7	0.41±0.02	0.63±0.02	1.18±0.05	141±7	2.8±0.3
WHr3	3.9	100	24±7	26.3±0.6	24.4±0.6	239±9	0.66±0.02	1.03±0.02	1.75±0.08	239±9	2.8±0.4

The luminesce ages from the two trenches at terrace 6 (Table 1) have parallel depositional records, and the samples are all consistent with each other (2.7±0.09, n=3). The highest sample is 2.5 ka, compared to the lower samples which were approximately 400 years older. Thus, deposition was active before the initiation of terrace construction.

The charred layer that was analyzed from terrace 90 (a terrace between the two branches) dated to 900-1100 CE, according to the ^{14}C analysis.

The GPR data profiles that were conducted were oriented E-W and NE-SW. The W-E profile shows the variation in the sediment accumulation thickness. It is noted that the sediment layers are compacted below a depth of 0.90m. However, from depths between 0.30-0.80m, three thick sediment layers probably reflect from three consecutive heavy floods. The NE-SW profile shows a more intense water flow/ depositional events of a relatively recent event (Figure 11). The radar cross-section suggests that the sediments behind terrace 68 are bedded towards the northeast, in the same direction of flow that existed before the construction of the terrace.

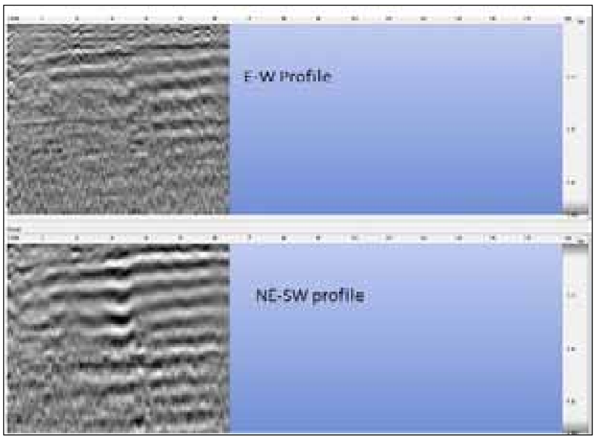

Figure 11. GPR profiles. The upper E-W profile loses evidence of stratigraphy below 90cm and shows at least 3 depositional events above. The lower NE-SW profile shows that recent depositional events as thicker and deeper, perhaps all post-dating terrace construction.

The botanic data from the charred layer contains a mix of chloridoid, festucoid, long-pointed trichome, and short-shaft dumbbell phytoliths. The dominating species were pointed trichomephytoliths followed by variants of short shaft dumbbell which is typical of grassland (Figure 12).

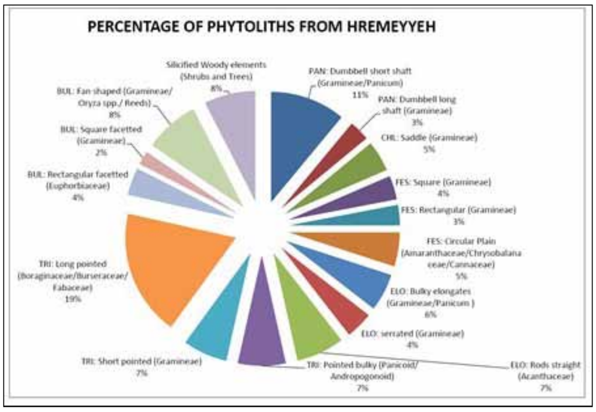

Figure 12. The various types of phytoliths found at terrace 90 at Hremiyyeh.

Half of the sample was comprised of a variety of (setaria and scirpus) wetland grasses, followed by a smaller percentage of wild species of Asphodelus and minor evidence of woods and shrubs, for example, Ziziphun seeds (Figure 13).

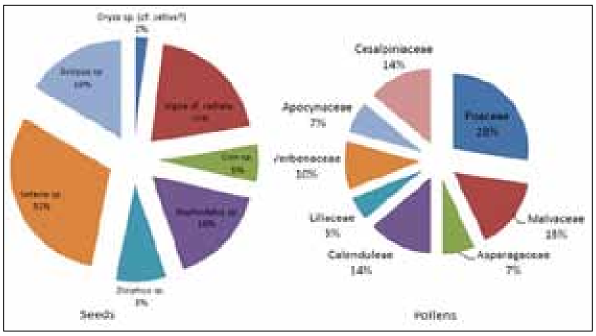

Figure 13. The seed and pollen types found at Hremiyyeh (terrace 90).

In addition to the wild grasses, evidence of cultivated plants was present by Coix, Orza Sativa, Vigna cf. Radiata (mug bean), all of which require abundant water to be grown or at least the presence of standing water. In addition to them, Asphodelus, and setaria (staple crops) were also identified. All these plants reflect a wet and warm region, which is an indication of standing water bodies that could be achieved by dams and terraces.

A small percentage of plant pollen was identified within the charred soil. Their typology confirmed the findings from both the phytoliths and seeds showing a variety of tree arboreal pollen, shrubs, and grasses. Their state of preservation was poor, probably to the alkaline nature of the soil and the high aridity which prevents their preservation. Again, the most abundant finds were for grass species of Poaceae and Malvaceae types. The arboreal species were represented by Apocynaceae and Cesalpiniaceae types (Figure 13). In addition, flowering plants were represented by the typology of Asparagaceae, Calenduleae, Liliaceae, and Verbenaceae. As pollen preservation is short, particularly in arid areas, these could represent the last phases of vegetation during the abandonment of the area and the restoration of the wild vegetation of the area.

4. Discussion

The concentration of Late Iron Age pottery in the higher areas of the drainage basin is consistent with the model put forward by Abu-Jaber et al. (2020a), whereby they viewed the absence of early evidence of human habitation in the basin as evidence of late denudation of sediments remaining from Lake Elji. Viewed in this context, it seems that the bulk of denudation at Wadi Hremiyyeh began in the Iron Age. The OSL dates of the sediments behind terrace 6 are consistent with this hypothesis. Thereafter, the terrace system was devised to manage the dynamic nature of the landscape. Initially, the interventions by terrace construction were conducted at the upper catchment area, based upon the dominant Edomite/ Iron II pottery found in the area, probably for surface water control. However, this was not enough during the Nabataean period, where the whole catchment was now the focus of larger-scale human expansion and exploitation.

Intensive terrace construction was implemented both at the upper catchment area and the lower part of the drainage basin at Hremiyyeh (Figure 2), the Wadi Musa fault defines a change in slope and the boundary between the Cretaceous and the Palaeozoic stratigraphic units in the area. Particularly, the small cracks and lateral fault zones through which water flow was extensively terraced to prevent water surface flow and to accumulate sediments. The runoff would increase on the smooth Disi sandstone dominating this area (al Qudah et al., 2016), the danger of which would affect the Khazneh Plaza, which was probably constructed as early as the second half of the first century BC (Farajat and Nawafleh, 2005). Thus the interventions at the upper catchment would fall around the second half of the 1st century BC to the first half of the 1st century AD, which is corroborated by the pottery found at the site.

In the area between the tributaries, there is little evidence for undercutting. Moreover, the amount of modern gullying is limited, despite damage to the terraces. On the contrary, the GPR profile shows that the pattern of sediment deposition changed after the terrace was built. Soil preservation and accumulation in this area is in evidence through the charred horizon preserved behind one of these terraces. The date of this horizon (10th to 11th century CE) indicates that the terraces continued accumulating sediment until that time. Moreover, the nature of botanical material found on the horizon (crops requiring abundant water) indicates that the terraces were used for agriculture at that point. Soil layers give interesting insights into the nature of these interventions as the soil layers were dipping towards the NNE from the upper SW hill towards the lower point of the valley. Owing to these factors, the Nabataeans intervened by constructing terraces into the existing soil and on the southern and western slopes of the hill. This helped stabilize the soil at these slopes.

Based on the phytolith and other botanical evidence there are indications of the climatic shift to more humid conditions, probably causing flash floods. During that time a gully seems to have developed at the western part of the middle catchment (between terrace 29 and terrace 49). During the L. Nabataean to E Roman period intensified terrace construction started within that branch to control the widening and migration of the gullying. These terraces seem to have gathered sediments towards the Byzantine period, as evidence of human settlement and agrarian activity intensification seem to occur.

The agricultural activity seems to intensify in the upper catchment during the 10th to 11th centuries, as evidenced by burning the wild bushes to create a larger area for agricultural activity as evidenced by the botanical data from the charred layer at terrace 90. These data also suggest a more humid phase in the area's history. It also seems to mark the time when some semblance of stability developed in the basin by the evidence of continued exploitation of the area until the Mamluk period.

Evidence for changes in the landscape morphology since the abandonment of the flood control system is seen in the down cutting below the terraces and the form of distinctive carbonate deposits marking the previous locations of terraces (Abu-Jaber et al., 2020b). At Wadi Hremiyyeh, the down cutting into the underlying bedrock is most pronounced in the upper tributaries to the east of the Wadi Musa Fault. Here, the interventions were the most extensive, with numerous massive check dams and terraces on the overlooking slopes. After abandonment, the siltation of the check dams was followed by breaches, gullying into the accumulated sediments, and ultimately cutting into the underlying sandstone bedrock.

The terraces built to the west of the fault retain sediments that predate the terraces themselves. This indicates that these were built into the sediment to prevent their mobilization. Here, carbonate deposits are evident behind places where the terraces had failed and the clastic sediments were moved (Figure 14). It is interesting to note that there are no carbonate deposits in front of the terraces, where presumably there were sediments before the terraces were built. Thus, the carbonate deposits were deposited as a result of the terrace building. The role of water in the deposition of carbonate has been noted previously (Abu-Jaber et al., 2020b), which suggests that the amount of water trapped in the sediments behind the dams increased significantly after the terraces were built. It is noteworthy that the terraces to the east show less carbonate deposition. This suggests that the terraces were not operational as long, or that they never became as waterlogged as the lower ones to the west.

Figure 14. Remains of terrace 25. Note the carbonate crust between the sediments and the bedrock upstream of the flow.

It is noteworthy that the drainage basin was accumulating sediment before the terracing (500-800 years BCE), and continued after the terraces were built. However, later neglect and deterioration of the terrace system resulted not only in sediment removal but also down cutting into the underlying bedrock. This is seen in the downcutting below the level of carbonate coating the sandstone substrate.

Evidence of dynamicity has been witnessed in other terraced areas of Petra. At Wadi Ghurab the soil underneath the terrace riser dates between (750-90 BCE), however, the fill in front of the terrace riser dates ranged from (110-740 CE) at 1.5m depth and (550-910CE) at 0.65m depth (Beckers et al., 2013), clearly indicating the erosion and redeposition of sediments in front of the terraces. At Wadi Sweig, the OSL dates of the sediment below the terrace riser yielded a date range between 950 and 1590 CE, while the terrace fill was older, ranging between 700 and 980 CE. An explanation for the fill being older than the riser through gully activity that caused the incision of younger sediments below the terrace riser and rebuilding activity of the riser has been put forward (Beckers et al., 2013). It is clear, however, that the terracing was done in an active wadi, and the riser was constructed to confine accumulated older terraces in the area or reconstruct an older collapsed terrace.

5. Conclusions

Iron age settlers seem to have had little influence on the topography, concentrating their efforts on the upper areas, as little of the lower catchment had been exposed, and was still buried. The Nabataeans, in what seems to have been a concerted effort to stabilize the dynamic drainage basin at Wadi Hremiyyeh, constructed a system of terraces to protect the Treasury Plaza from floods and sediments. This system came in the form of check dams to the west of the Wadi Musa Fault, terraces, gabions, and check dams in the two tributaries in the more rugged area to the east of the fault.

Gullying played an important role in reshaping the landscape and shifting the sediments, based on the huge efforts to construct dams and check dams to prevent their flow. It is plausible that headwater retreat may have grown more severe with time, making the task increasingly difficult and the effort ever more frantic.

Thus, human interventions in Wadi Hremiyyeh resulted in the modification of the landscape. This temporary stabilization resulted in delayed and then enhanced down cutting, the creation of agricultural fields, and the accumulation of carbonates. Studying terraces allow the tracing of all of these events. On a broader picture, it illustrates that the area was a site of early human interventions, trying to stop denudation at the site when the Nabataeans of Petra were benefiting from freshly exposed Palaeozoic sandstones downstream, carving their magnificent city into it.

The study clearly shows that terraces are good proxies for the reconstruction of the evolution of topographic and environmental change through time even in a confined catchment area. This is seen from the fact that they were constructed in the first place, their locations, and elevations at the time of construction, and the nature of deposits found behind and beneath them.

Acknowledgment

We are thankful to the Petra Development Tourism Regional Authority for their help in facilitating this research. We also would like to thank Sanjay Eksambekar for his analysis of the botanical remains.

Funding

This project was funded by the Scientific Research and Innovation Fund of Jordan (grant WE/1/6/2017).

References

Abdelal, Q., Al-Rawabdeh, A., Al Qudah, K., Hamarneh, C. and Abu-Jaber, N., 2021. Hydrological assessment and management implications for the ancient Nabataean flood control system in Petra, Jordan. Journal of Hydrology, p.126583.

Abu-Jaber, N., Al Khasawneh, S., Alqudah, M., Hamarneh, C., Al-Rawabdeh, A. and Murray, A., 2020a. Lake Elji and a geological perspective on the evolution of Petra, Jordan. Palaeogeography, Palaeoclimatology, Palaeoecology, 557, p.109904.

Abu-Jaber, N., Rambeau, C., Hamarneh, C., Lucke, B., Inglis, R. and Alqudah, M., 2020b. Development, distribution, and palaeoenvironmental significance of terrestrial carbonates in the Petra region, southern Jordan. Quaternary International, 545, pp.3-16.

Aitken, M. J. 1985: Thermoluminescence dating. 359 pp. Academic Press, London.

Al-Farajat, M. and Salameh, E., 2010. Vulnerability of the drinking water resources of the Nabataeans of Petra, Jordan. Jordan Journal of Civil Engineering, 4(4): 321-335.

Al Khasawneh, S., Murray, A., Thomsen, K., AbuAzizeh, W., & Tarawneh, M., 2019a. Dating a near eastern desert hunting trap (kite) using rock surface luminescence dating. Archaeological and Anthropological Sciences, 11(5), pp.2109-2119.

Al Khasawneh, S., Murray, A. and Abudanah, F., 2019b. A first radiometric chronology for the Khatt Shebib megalithic structure in Jordan using the luminescence dating of rock surfaces. Quaternary Geochronology, 49, pp.205-210.

Al Khasawneh, S., Abu-Jaber, N., Hamarneh, C. and Murray, A., 2022. Age determination of runoff terrace systems in Petra, Jordan, using rock surface luminescence dating. Archaeological and Anthropological Sciences, 14(3), pp.1-12.

Al Qudah, K., Abdelal, Q., Hamarneh, C. and Abu-Jaber, N., 2016. Taming the torrents: The hydrological impacts of ancient terracing practices in Jordan. Journal of Hydrology, 542, pp.913-922.

Barjous, M.O., 2003. The Geology of Petra and Wadi Al Lahyana Area: Map Sheets No.3050-I and 3050-IV. Natural Resources Authority, Amman, Jordan.

Barjous, M. and Mikbel, S., 1990. Tectonic evolution of the Gulf of Aqaba-Dead Sea transform fault system. Tectonophysics 180 (1), 49–59.

Bäumler, R., Lucke, B., Birk, J., Keilholz, P., Hunt, C.O., Laparidou, S., Abu-Jaber, N., Kouki, P. and Fiedler, S., 2020, May. The terraces of Petra, Jordan: archives of a lost agricultural hinterland. In EGU General Assembly Conference Abstracts (p. 306).

Beckers, B., Schütt, B., Tsukamoto, S., Frechen, M. ,2013. Age determination of Petra's engineered landscape-optically stimulated luminescence (OSL) and radiocarbon ages of runoff terrace system in the Eastern Highlands of Jordan, Journal of Archaeological Science,40, 333–348.

Bellwald, U., 2008. The Hydraulic Infrastructure of Petra–A Model for Water Strategies in Arid Land. Cura aquarum in Jordanien, 12, pp.47-94.

Bienkowski, P., 2013. The Iron Age in Petra and the issue of continuity with Nabataean occupation. Men on the rocks. The formation of Nabataean Petra. Logos, Berlin, pp.23-34.

Dalman, G., 1908. Petra und seine Felsheiligtümer. JC Hinrichs.

Farajat, S. and Nawafleh, S., 2005. Report on the Al-Khazneh courtyard excavation at Petra (2003 season), Annual of the Department of Antiquities of Jordan, 49, pp. 373–393.

Frederick, C., and Krahtopoulou, A., 2000. Deconstructing agricultural terraces: Examining the influence of construction method on stratigraphy, dating and archaeological visibility', in Halstead, P., Frederick, C. (eds.) Landscape and land use in postglacial Greece, Sheffield studies in Aegean archaeology. Sheffield: Sheffield Academic Press, pp. 79–94.

Galli, A., Panzeri, L., Rondini, P., Poggiani Keller, R., & Martini, M., 2020. Luminescence Dating of Rock Surface. The Case of Monoliths from the Megalithic Sanctuary of Ossimo-Pat (Valle Camonica, Italy). Applied Sciences, 10(21), p7403.

Guérin, G., Mercier, N. and Adamiec, G., 2011. Dose-rate conversion factors: update. Ancient Tl, 29(1), pp.5-8.

Hamarneh, C., 2022. Investigating man-made terraces of Petra, Jordan. Ph.D. Dissertation. Von Humboldt University, Berlin, Germany.

Hansen, V., Murray, A., Thomsen, K., Jain, M., Autzen, M. and Buylaert, J.-P., 2015: Towards the origins of over-dispersion in beta source calibration. Radiation Measurements 120, pp. 157–162

Jain, M., Murray, A. S. and Bøtter-Jensen, L., 2003. Characterization of blue-light stimulated luminescence components in different quartz samples: implications for dose measurement. Radiation Measurements 37, pp. 441–449.

Jones, M.D., Abu-Jaber, N., AlShdaifat, A., Baird, D., Cook, B.I., Cuthbert, M.O., Dean, J.R., Djamali, M., Eastwood, W., Fleitmann, D. and Haywood, A., 2019. 20,000 years of societal vulnerability and adaptation to climate change in southwest Asia. Wiley Interdisciplinary Reviews: Water, 6(2), p.e1330.

Kiesow, S. and Bork, H.R., 2017. Agricultural terraces as a proxy to landscape history on Madeira island, Portugal. LerHistória, (71), pp.127-152.

Kinnaird, T., Bolos, J., Turner, A. and Turner, S., 2017. Optically-stimulated luminescence profiling and dating of historic agricultural terraces in Catalonia (Spain). Journal of Archaeological Science, 78, pp.66-77.

Kouki, P., 2012. The Hinterland of a city: rural settlement and land use in the Petra region from the Nabataean-Roman to the Early Islamic period. Ph.D. Dissertation, Faculty of Arts, University of Helsinki, Finland.

Lindner, M. and Hübl, H., 1997. Where Pharao's Daughter Got Her Drinking Water From. The'Ēn Brāk Conduit to Petra. Zeitschrift des Deutschen Palästina-Vereins (1953-), pp.61-67.

Lucke, B., Roskin, J., Vanselow, K.A., Bruins, H.J., Abu-Jaber, N., Deckers, K., Lindauer, S., Porat, N., Reimer, P.J., Bäumler, R. and Erickson-Gini, T., 2019. Character, rates, and environmental significance of Holocene Dust accumulation in archaeological Hilltop Ruins in the southern Levant. Geosciences, 9(4), p.190.

Lucke, B., Sandler, A., Vanselow, K.A., Bruins, H.J., Abu-Jaber, N., Bäumler, R., Porat, N. and Kouki, P., 2019. Composition of Modern Dust and Holocene Aeolian Sediments in Archaeological Structures of the Southern Levant. Atmosphere, 10(12), p.762.

Meyer, M., Gliganic, L., & May, J. H., 2020. Direct dating of lithic surface artefacts using luminescence and application potential in geomorphology. In EGU General Assembly Conference Abstracts. p 19195.

Murray, A.S. and Wintle, A.G., 2003. The single aliquot regenerative dose protocol: potential for improvements in reliability. Radiation Measurements 37, pp. 377–381.

Pedrera, A., Pérez-Peña, J.V., Galindo-Zaldívar, J., Azañón, J.M. and Azor, A., 2009. Testing the sensitivity of geomorphic indices in areas of low-rate active folding (eastern Betic Cordillera, Spain). Geomorphology, 105(3-4), pp.218-231.

Prescott, J.R. and Hutton, J.T., 1994. Cosmic ray contributions to dose rates for luminescence and ESR dating: large depths and long-term time variations. Radiation measurements, 23(2-3), pp.497-500.

Rhodius, C., Kadereit, A., Siegel, U., Schmidt, K., Eichmann, R. and Khalil, L.A., 2017. Constraining the time of construction of the irrigation system of Tell Hujayrat al-Ghuzlan near Aqaba, Jordan, using high-resolution optically stimulated luminescence (HR-OSL) dating. Archaeological and Anthropological Sciences, 9(3), pp.345-370.

Sarp, G., Gecen, R., Toprak, V. and Duzgun, S., 2011, April. Morphotectonic properties of Yenicaga basin area in Turkey. In 34th International symposium on remote sensing of environment (ISRSE34) (pp. 10-15).

Spencer, J.E. and Hale, G.A., 1961. The origin, nature, and distribution of agricultural terracing. Pacific viewpoint, 2(1), pp.1-40.

St-Jean, G., Kieser, W.E., Crann, C.A. and Murseli, S., 2017. Semi-automated equipment for CO2 purification and graphitization at the AE Lalonde AMS Laboratory (Ottawa, Canada). Radiocarbon, 59(3), pp.941-956.

Tholbecq, L, Abudaneh, F. , Al- Salameen, Z. and Kurdy, M., 2018. 3.4 Pétra- Une Première campagne de documentation du sanctuaire de source de khirbatBraq (Wadi Musa, Jordanie) in "Mission ArchéologiqueFrançaise À PÉTRA, Rapport des campagnesarchéologiques 2017-2018, Edite par Laurent Tholbecq, Breuxelles, p117-138.

Thomsen, K.J., Jain, M., Murray, A.S., Denby, P.M., Roy, N. and Bøtter-Jensen, L., 2008. Minimizing feldspar OSL contamination in quartz UV-OSL using pulsed blue stimulation. Radiation Measurements, 43(2-6), pp.752-757.

Treacy, J.M. and Denevan, W.M., 1994. The creation of cultivable land through terracing. The archaeology of garden and field, University of Pennsylvania Press, pp.91-110.

Vandenberghe, D., De Corte, F., Buylaert, J.P. and Kučera, J., 2008. On the internal radioactivity in quartz. Radiation Measurements, 43(2-6), pp.771-775.

Wintle, A.G. and Murray, A.S., 2006. A review of quartz optically stimulated luminescence characteristics and their relevance in single-aliquot regeneration dating protocols. Radiation Measurements, 41(4), pp.369-391.

JJEES

JJEES (2022) 13 (4): 242-246
ISSN 1995-6681

Jordan Journal of Earth and Environmental Sciences

Drainage Pattern Analysis for Sustainable Environmental Planning, Himachal Pradesh, India

C Prakasam[1, *], Saravanan R[2],

[1]Department of Geography, School of Earth sciences, Assam University, Diphu campus, Diphu, Karbi Anglong Assam, India
[2]Ecofirst Services Limited, Tata Consulting Engineering Limited, Bangalore, Karnataka, India

Received 9th January 2022; Accepted 7th April 2022

Abstract

The Beas River inducts in the upper Himalayas beginning at Beas Kund contiguous Rohtang Pass in Himachal Pradesh and streams in the east-west course in Himachal Pradesh. Binwa hydropower project, a small potential project is situated in the Kangra district along the tributaries of the Beas River basin. To design the suitable ecological planning and management of rivers, structures acknowledge a dominant occupation. The sustainability of the ecological cycles is sufficient to make changes in morpho-units of the landscapes. To plan base guide from ASTERDEM will be utilized. In the analysis of drainage, Strahler's stream-area methodology of stream demand will be associated. To separate the Sub-basin of Beas River orchestrated distinctive thematic layers of the basin will be used. The morphometric parameter, for example, stream request, number, length, drainage thickness, bifurcation ration, surface, and so forth, are quantitatively investigated. The investigation destinations come into focus on the utilization of the nature of environmental resources, and hydrological planning to build up a system for figuring out the reasonableness for changed usages of the landforms in the setting with condition improvement.

Keywords: *Drainage pattern, Beas River Basin, Binwa, Environmental planning*

1. Introduction

The drainage analysis is the pivotal analysis in assessing the landforms. It has a precise relevance to geomorphology. The hydrological response of the basin is characterized by the runoff generation versus precipitation, which thusly is depicted by basin soil characteristics, morphometric properties, and land use network. As an inseparable piece of the topography, the drainage network is an essential portion of the Remote Sensing and Geographic Information System. In a drainage structure; streams constantly interface together to shape frameworks. As of now, much exploration is concerning hydrology and geography. In GIS; such gathering can be important for territory examination or theory (Dash et al, 2019). The GIS application in the Morphometric analysis is a very much time-saving, effective, and accurate technique to plan and manage the watershed basin. The site-specific suitability measures and watershed development and management can be planned accordingly. This has been a proven technique for analyzing morphometric parameters (Saha and Singh 2017). The morphometric components such as land use maps and topographical maps of the basin are mapped and evaluated concerning basin management. The basin possesses the 5th-order of stream of dendritic drainage pattern, which is a sign of the lack of structural control and homogeneity in texture. If the drainage density is very low then the basin possesses very good permeable subsurface formation which in turn prospects for water management (Prakasam, and Saravanan 2020). The detailed analysis of the watershed drainage and morphometric pattern watershed is pivotal in understanding the landforms and land usage using the drainage pattern (Prakasam et al., 2021) studied the hydropower project impact on the downstream side through the GIS application. The drainage analysis highlighted the changes in the basin.

1.1 Types of Drainage

Drainage designs are arranged based on their structure and surface according to incline and structure. Their shape or example creates in response to the neighborhood topography and subsurface geography. There are five kinds of drainage design Dendritic, Parallel, Trellis, Rectangular, and Reticulate. Because of the portrayal of various drainage designs, each example has its attributes, which can be reflected in some quantifiable variables identified with some topological and geometrical viewpoints. In Dendritic, the joining tributaries structure an intense point. The parallel is additionally in parallel structure with stretched watershed with long intense calculated straight tributaries. Trellis shapes the right edge and short straight tributaries. Rectangular curves and structures right point tributary and finally reticulate is in a cross like forming a circle tributary. Therefore, each example can be portrayed by a combination of various variables. In this area, the method for drainage design acknowledgment is introduced. In the first place, terms describing river systems are defined then characterization criteria are introduced and the distinctive strides of the procedure are point by point. Identifying the drainage pattern and its properties helps in characterizing sustainable planning of the watershed for the management of the resources. This paper attempts to understand the drainage pattern of the Binwa watershed for better watershed planning using GIS techniques.

* Corresponding author e-mail: cprakasam@gmail.com

2. Study Area

Binwa watershed is 340.1 sq, km located in Kangra district, Himachal Pradesh., between Shivalik undulated slopes and Lesser Himalayas (Figure 1). It is located in the Agricultural Economic Region, a warm sub sticky to damp Eco-district with dim-hued woodlands and podzolic soils (Sehgal et al., 1990)].The elevation ranges from 600 to 4286 m above MSL. Binwa watershed is tended to by a wet mild atmosphere with a yearly rainfall ranging from 1757 to 2798 mm. The mean most noteworthy and minimum temperature ranges were from 24.2˚C to 27.7˚C and 13.7˚C to 14.6˚C, independently. The measure of precipitation is gotten during the rainstorm timeframe. The rainfall period is from March to June and October to December. The watershed is portrayed by the closeness of Udic soil dampness administration and thermic temperature administration (Sidhu and Mahapatra 1997).

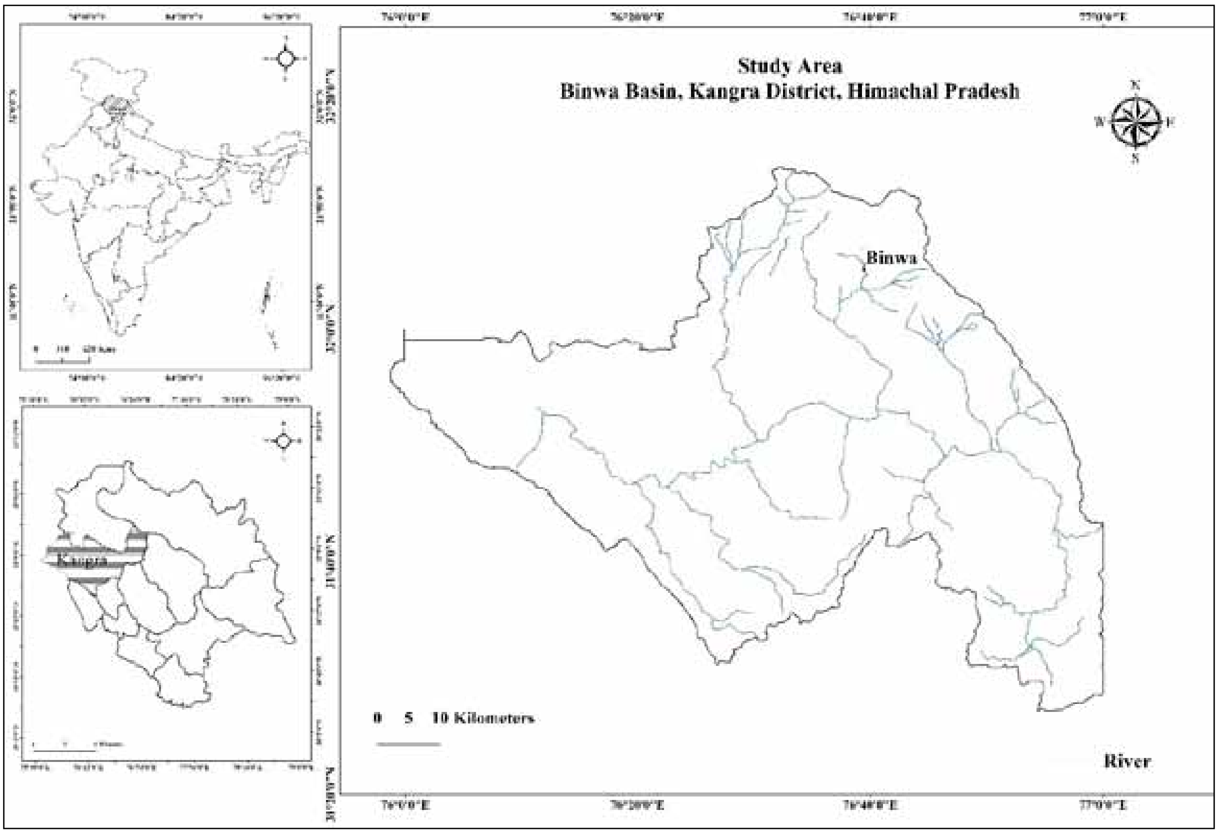

Figure 1. Index map of the Study Area.

From the grained rocks of Shivaliks and lower Himalayas such as phyllite, quartzite, granite, shale, sandstone, gneiss, etc., the Binwa watershed soils are formed along with fluvial deposits. Fluvial patios are created because of the water developments at the edge of the streams in the low slope zone.

3. Materials and Methods

The drainage pattern of the Suketi river basin has been studied for planning environmental aspects properly (Verma et al., 2012). 1:50000 scale SOI Topo sheets were used to set up the base guide to dissecting Stahler's stream and different layers were ready to outline the Suketi waterway bowl feeders (Momoh and Rilwani 2014). Displayed geo informatics-based for Muya watershed for its drainage characteristics in the Upper Niger bowl, Nigeria. Stream design was made utilizing the Landsat and geographical data, while at first DEM was made utilizing the geography map. The interaction evaluated the Fundamental drainage boundaries, for example, accumulation, direction, length, density, bifurcation ratio, and so forth, which were assessed to give a concise thought regarding the seepage model in the review region (Zhang and Guilbert 2012). Presented a procedure reliant upon mathematical quantitative markers to see the seepage plans in a waterway regularly. The creator gave an outline of various kinds of waste examples and their attributes. The linear aspects consist of stream number, stream order, bifurcation ratio, stream length, and stream length ratio (Rathore et al. 2022). Javarayigowda (2018) an attempt has been made utilizing GIS to look at the morphometric boundaries of the Karadya limited scope watershed. The examination uncovers that the landscape shows a dendritic sort seepage plan with the most critical stream demand being the third order. The Aster DEM has been downloaded from the open-source network known as the earth explorer site and imported into the GIS environment. The process starts with filling up the voids and is followed by the flow direction. The next step is flow accumulation. Using the calculator, the accumulation value greater than 1000 is delineated using GIS and finally, the drainage has arrived. The basin is then clipped for the study area purpose (Prakasam et al, 2021).

3.1 Stream order

It is the proportion of the overall size of streams and the littlest tributaries, generally enduring are alluded to as first-request (first) streams, trailed by a second request beginning where two 1st orders meet to shape the second request, in that movement until the water exhausts into another significant river (Figure 2) (Oyedotun 2020). The stream order is directly proportional to the size of the drainage, sub-basins, and river discharge. The study area comprises stream order up to 6th order. The first-order stream is 48 % followed by 25% of the second-order stream, third order stream is 13% and the fourth, fifth, and sixth-order streams are 7%, 3%, and 5% respectively. Here the lower-order stream is high in number and hence the yielding capacity of the water basin is high during the rain and also contributes to the groundwater.

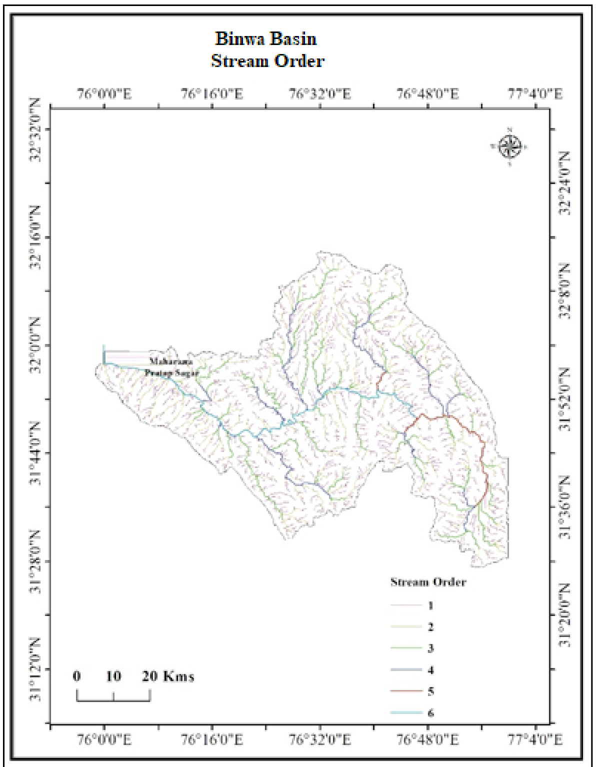

Figure 2. Map showing the Stream order in the Study area (source: ASTERDEM).

3.2 Stream Number (Nu)

The total number of stream fragments based on the stream order is the stream number (Bharath et al. 2021). It refers to the cumulative amount of stream/drainage segments of each order. It prompts the inference that a few streams generally upsurge in geometric movement as the order of the stream increases. A higher stream number indicates lesser porousness and infiltration (Figures 3and 4). The plot between the stream order and number gives the idea of the total number of streams present in the drainage pattern. Here a total of 5079 of the stream is present, out of which first-order contributes much to the overall rate with 2440 streams in total. It indirectly indicates that the infiltration capacity of the study area is also high. The plot between the order and number shows that the drainage pattern is healthy, as good drainage conditions contribute to better water-holding capacity and flowing properties present (Table 1).

Table 1. Stream order, counts and percentage

Stream order	Stream counts	Percentage of stream%
1	2440	48
2	1249	24
3	655	13
4	350	7
5	145	3
6	240	5
	5079	100

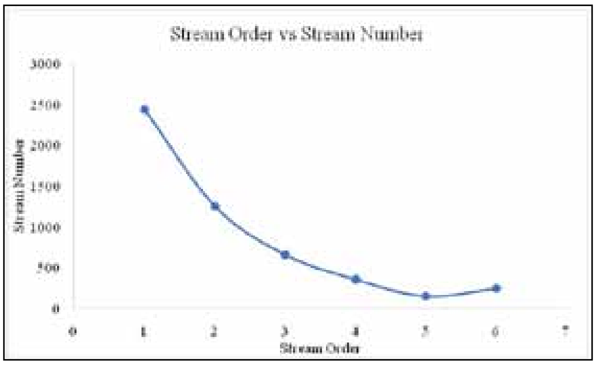

Figure 3. Plot between Stream order vs Stream number

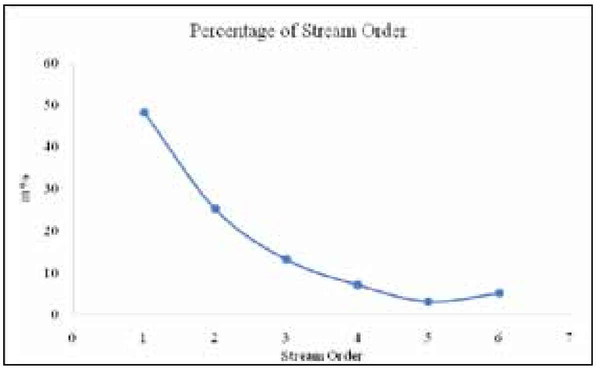

Figure 4. Stream order vs Stream number

3.3 Drainage pattern

Based on the physical characteristics of the drainage such as joint angle, length of the stream, and shortness, the pattern has been characterized (Qadir et al., 2021). The drainage pattern has been derived from the hydrological analysis of the DEM. The western side (downstream) end has a reservoir namely Maharana Pratap Sagar. Hence the drainage lines show straight in that region. The influence of the geological structures won't affect much on the drainage pattern if the bifurcation ratio is between 3.84 and 5.30. The bifurcation ration and flooding are inversely proportional. Studying the pattern helps in determining the plan of the study area, as each pattern has different properties for conducting the drainage. Based on the angle, length of the stream, etc., it is identified that the dendritic pattern of drainage is found in the study area. It is tree-like patterns are found in places where there is no robust geological control and homogenous texture (Figure 5).

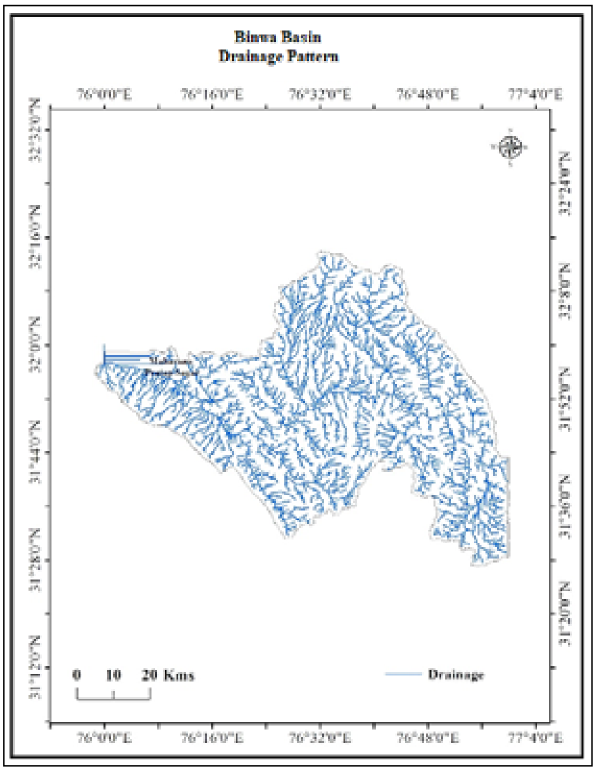

Figure 5. Map showing the Drainage pattern in the Study area.

3.4 Drainage density

The ratio between the total lengths of the stream in the numerator to the area of the basin in the denominator is the drainage density (Figure 6) Melese and Belay (2021). Drainage density is inversely proportional to the groundwater probability. Since runoff and permeability are related to the drainage density, it indirectly indicates the groundwater potential in the proposed area:

Drainage density =

(Total length of the drainage / Area of the basin) ………… (1)

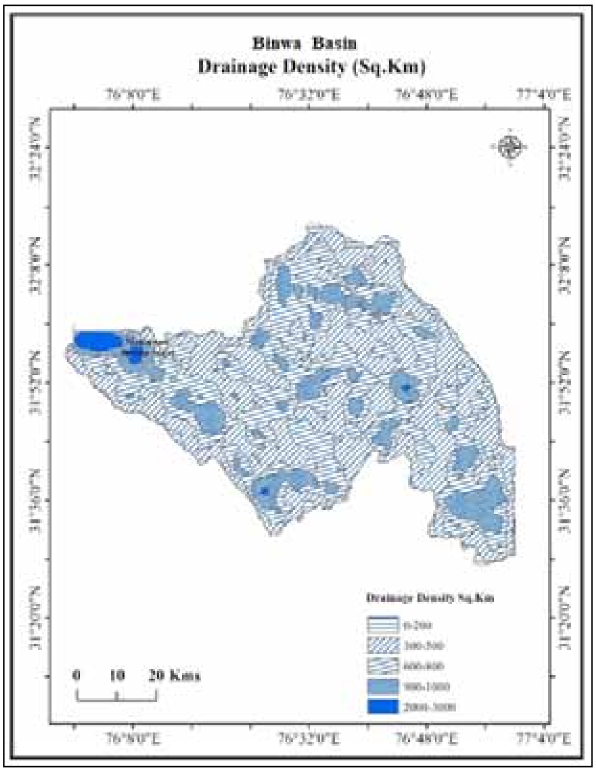

Figure 6. Map showing the Drainage density in the study area.

The drainage density analysis shows that it ranges up to 3000 Sq.Km of the total area. The basin comprises a maximum low-density ratio indicating that the free flow of water in the topology occurs and gets drained soon with less soil moisture and poor vegetation. The high density indicates high vegetation content in the region in which high soil moisture content can be identified in the region. The western portion has a reservoir downstream hence the drainage density is high.

3.5 Texture ratio

The ratio between the numbers of streams/drainage to the perimeter of the study basin. It is indirectly related to the drainage density, as it increases the texture also increases. The basin area is of a homogeneous texture of moderate. The classification of the texture ratio ranges between very coarse to very fine texture.

3.6 Stream Length

The stream length is defined as the stream order's length. The total stream length is 388.99 km. Stream length indicates the contributing area of the basin of each stream order. The length of the first to sixth-order stream is as follows 186.88 km, 95.65 km, 50.16 km, 26.81 km, 11.15 km, and 18.34 km. The plot between the stream order and stream length shows that the first-order stream has a higher length and it gradually decreases. The lithological inconsistency could be the reason why higher stream length in 1st order and gradually decreases with low order streams. The control over the morphological and geological characteristics of the basin could also be a reason (Mallick, et al., 2022).

Table 2. Stream length for each Stream order.

Stream order	Stream length (Km)
1	186.88
2	95.65
3	50.16
4	26.81
5	11.15
6	18.34
	388.99

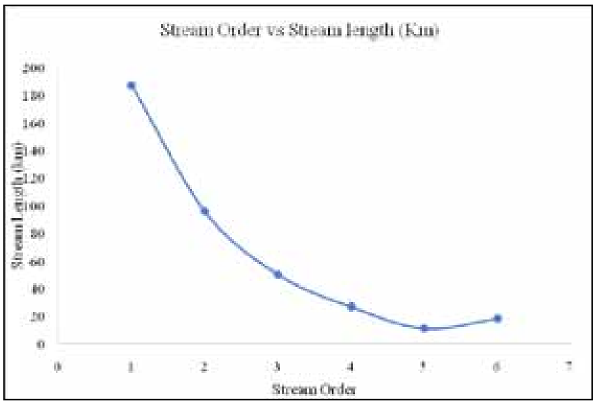

Figure 7. Stream order vs Stream number

3.6 Bifurcation ratio (Rb)

The Bifurcation ratio is termed as the proportion between the quantities of streams in progressive stream order. Here 'Nu' is the stream quantity and (Nu+1) is the number of drainages in the following higher order (Schumm, 1956):

Rb=Nu/Nu+1 ……...… (2)

It is a ratio whose values lie between 3 to 5. The bifurcation ratio is 4.21, indicating a lower permeability region in the study area.

4. Conclusion

The drainage analysis has been carried out for the Binwa basin for preparation and planning of the basin for hydropower project studies. Stream order is a significant boundary in the drainage network framework which upholds a wide scope of utilizations, for example, flood risk appraisal, water asset the board, flood immersion planning, watershed the executives, and some more. The drainage pattern of the considered area is described by a dendritic sort drainage basin. The first-order stream is found to be high in number than the others. The total number of streams is also large for the first-order stream and reduces gradually for the sixth-order stream. During heavy precipitation, the surface drainage system varies from the stream framework essentially. These distinctions are reflected in the thickness and the interior design of the frameworks. The drainage density analysis shows that the study area is of poor soil moisture content and constitutes a maximum of less drainage density in the region. The homogenous texture of moderate range is identified in the study region and the bifurcation ratio is 4.21 indicating lower permeability in the region. Stream length analysis shows that the first-order stream is higher. For better and sustainable watershed management practices in this study area, this research will be helpful. The location of dams, wells, or any water structures can be determined through this study. In this way, Drainage design study proposals will support the decision makers and chiefs to find a genuine answer for the issue picked.

References

Bharath, A., Kumar, K. K., Maddamsetty, R., Manjunatha, M., Tangadagi, R. B., & Preethi, S. (2021). Drainage morphometry based sub-watershed prioritization of Kalinadi basin using geospatial technology. Environmental Challenges, 5, 100277.

Dash, B., Nagaraju, M. S. S., Sahu, N., Nasre, R. A., Mohekar, D. S., Srivastava, R., & Singh, S. K. (2019). Morphometric analysis for planning soil and water conservation measures using geospatial technique. Int. J. Curr. Microbiol. App. Sci, 8(1), 2719-2728.

Javarayigowda, N. H., Basavaraju, G. K. S., & Jayaram, S. H. (2018). Morphometric analysis of Karadya micro watershed: A case study of Mandya district. American Journal of Remote Sensing, 6(1), 15.

Mallick, J., Shivhare, V., Singh, C. K., & Al Subih, M. (2022). Prioritizing Watershed Restoration, Management, and Development Based on Geo-Morphometric Analysis in Asir Region of Saudi Arabia Using Geospatial Technology. Polish Journal of Environmental Studies, 31(2).

Melese, T., & Belay, T. (2021). Groundwater Potential Zone Mapping Using Analytical Hierarchy Process and GIS in Muga Watershed, Abay Basin, Ethiopia. Global Challenges, 2100068.

Momoh, I. E. B. A. A., & Rilwani, L. (2014). Geoinformatics Characterization of drainage systems within Muya Watershed in the upper Niger drainage basin, Nigeria. International Journal of Research, 2(3), 2311-2484.

Oyedotun, T. D. T. (2020). Quantitative assessment of the drainage morphometric characteristics of Chaohu Lake Basin from SRTM DEM Data: a GIS-based approach. Geology, Ecology, and Landscapes, 1-14.

Prakasam, C., & Saravanan, R. (2020). Assessment of Environmental Changes using GIS Applications. International Journal of Innovative Technology and Exploring Engineering, 16.

Prakasam, C., Saravanan, R., & Sharma, M. K. (2021). Assessment of Environmental Flow Requirements through Rainfall-Runoff Modelling for Hydropower Project. In F-EIR Conference on Environment Concerns and its Remediation (pp. 231-249). Springer, Cham.

Prakasam, C., Aravinth, R., Kanwar, V. S., & Nagarajan, B. (2021). Sustainable Water Resource Management Using Watershed Morphometry–A Case Study of Giri River Catchment, Himachal Pradesh, India. Geographic Information Science for Land Resource Management, 229-250.

Qadir, A., Yasir, M., Abir, I. A., Akhtar, N., & San, L. H. (2020). Quantitative Morphometric Analysis Using Remote Sensing and GIS Techniques for Mandakini River Basin. In IOP Conference Series: Earth and Environmental Science (Vol. 540, No. 1, p. 012021). IOP Publishing.

Rathore, C. S., Singh, M., Kothari, M., & Yadav, K. K. (2022). Morphometric Analysis of Bhesra Kalan Micro-watershed using Remote Sensing and GIS Technique. Indian Journal of Ecology, 49(1), 155-160.

Saha, A., & Singh, P. (2017). Drainage morphometric analysis and water resource management of Hindon river basin, using earth observation data sets. International Journal of Interdisciplinary Research (IJIR), 3(4), 2051-2057.

Sehgal, J. L., Mandal, D. K., Mandal, C., &Vadivelu, S. (1990). Agro-ecological regions of India. NBSS Publication, (24).

Schumm, S. A. (1956). Evolution of drainage systems and slopes in badlands at Perth Amboy, New Jersey. Geological Society of America Bulletin, 67(5), 597-646.

Sidhu, G. S., & Mahapatra, S. K. (1997). Soils of Himachal Pradesh: their kinds, distribution, characterization, and interpretations for optimising land use. National Bureau of Soil Survey & Land Use Planning, Indian Council of Agricultural Research.

Verma, N., Khanduri, K., & Singh, P. (2012). The study of drainage patterns of Suketi River Basin for the proper environmental planning, Mandi District, Himachal Pradesh, India. International Journal of Environmental Sciences, 2(3), 1575-1584.

Zhang, L., & Guilbert, E. (2012). A study of variables characterizing drainage patterns in river networks.

JJEES

JJEES (2022) 13 (4): 247-262
ISSN 1995-6681

Jordan Journal of Earth and Environmental Sciences

Landsat / MODIS Fusion for Soil Moisture Estimation Over a Heterogeneous Area in Northern Jordan

Ali Almagbile[1,2*], Khaled Hazeymeh[1,2], Mostafa Mosleh[3], Abdulla Al-Rawabdeh[4,2], Omar Aldayafleh[1], Mohammad Zeitoun[1], Amer Maslamani[1]

[1]*Department of Geography, Yarmouk University, 21163 Irbid, Jordan*
[2]*Applied Geoinformatics Laboratory, Yarmouk University, 21163 Irbid, Jordan*
[3]*Department of Geography, Faculty of Arts, South Valley University, Qena 83523, Egypt*
[4]*Department of Earth and Environmental Sciences, Yarmouk University, 21163 Irbid, Jordan*

Received 17th October 2021; Accepted 9th April 2022

Abstract

Fusion models have been developed to improve the spatial and temporal resolution simultaneously because remote sensing data cannot guarantee the high resolution of vegetation and temperature products. In this study, Moderate Resolution Imaging Spectroradiometer (MODIS) and Land Remote Sensing Satellite (Landsat) data were fused using the STI-FM fusion model for retrieving soil moisture index (SMI) based on the NDVI-LST triangulation/trapezoidal shape. The study was conducted from November 2019 to May 2020 and covered a heterogeneous area in Northern Jordan. For validation, the soil moisture index results were then compared with the observed in-situ soil moisture measurements at 16 sites distributed throughout the study area. To determine the spatial and temporal variability/stability of SMI and observed soil moisture, statistical and geostatistical approaches were employed. The results revealed that the relationship between SMI and in-situ measurements was high in the wet winter months and low during the warm summer months. The determination coefficient r^2 of 0.66 and RMSE of 0.10 were found in January while in May, the r^2 and RMSE were 0.35 and 0.32, respectively. The results of the semi-variogram analysis showed that the observed soil moisture was more varied during the wet periods when compared with the drier period, whereas the SMI was not influenced by seasonal variations. The results indicated that high values of SMI can be obtained with low temperature and rich vegetation, while the higher temperature and water-stressed vegetation revealed low SMI values.

Keywords: *Soil moisture index, Data fusion, NDVI-LST space, Land surface temperature, NDVI, In-situ measurements*

1. Introduction

One of the key components for understanding soil moisture variability in spatial and temporal scales involves analyzing the inter-relationship between vegetation and temperature indices. The variation of soil properties, such as texture, porosity, permeability, and organic matter, could affect the distribution of soil moisture at local scales (Mohanty and Skaggs 2001). Topography in terms of slope, aspects, and curvature could also have a significant contribution to soil moisture variations even over a small area as they could determine the runoff and evapotranspiration rates. The Topographic Wetness Index (TWI) (Beven and Kirkby 1979) is common and widely used in determining the spatial variation of soil moisture and runoff generation (Grabs et al. 2009). Vegetation type and density might influence the spatiotemporal distribution of soil moisture as they control the infiltration, runoff generation, evapotranspiration rates, and the dynamic of soil water-retention capacity (Mohanty and Skaggs 2001, Jin et al. 2011). Since vegetation responds to precipitation, its influence on soil moisture variation is more dynamic in comparison with the topography factor.

Generally, soil moisture estimates can be extracted by either direct or indirect techniques (Dorigo et al. 2011, Almagbile et al. 2019). The direct technique involves a gravimetric method that calculates soil moisture as a percentage by weighting the moist soil, then oven drying it at 105 Celsius, and reweighting the dried soil. Whereas indirect methods measure soil moisture through electromagnetic instruments such as neutron probes, capacitance sensors, time-domain reflectometry (TDR), Tensiometers, electrical resistance blocks, and Psychrometers. The trade-off between these sensors varies in terms of sensor costs, the size of soil moisture data, and the wetness status of the soil (Bogena et al. 2007, Robinson et al. 2008, Seneviratne et al. 2010, Dorigo et al. 2011).

Although in-situ-based measuring of soil moisture could provide more reliable and accurate measurements of the actual amount of water in the soil at various depths, these measurements are limited in their spatial and temporal scales. To overcome this, remote sensing methods have been extensively used in mapping soil moisture variability at larger spatial extents (Xu et al. 2018). In this context, Soil Moisture Index (SMI) is widely applied. SMI is normally calculated by employing the universal triangular/trapezoidal eigenspace theories of the relationship between land surface temperature (LST) and normalized vegetation index (NDVI) (Carlson 2007, Choi and Hur 2012) using the optical and thermal spectral bands of different satellite systems such as

* Corresponding author e-mail: a.magbile@yu.edu.jo

Moderate Resolution Imaging Spectroradiometer (MODIS) and Landsat (Sandholt et al. 2002, Sun et al. 2012, Xu et al. 2018, Fan et al. 2019).

Since remote sensing observations have either a high spatial resolution or high temporal resolution, MODIS/Landsat fusion models have been developed to produce high-resolution data in both temporal and spatial scales. Such models include the Spatial and Temporal Adaptive Reflectance Fusion Model (STARFM) (Gao 2006), the Spatial-temporal Adaptive Data Fusion Algorithm for Temperature mapping (SADFAT) (Weng et al., 2014), and the Spatial-temporal Image Fusion Model (STI-FM) (Hazaymeh and Hassan 2015a).

The relationship between soil moisture and Normalized Difference Vegetation Index (NDVI) has been investigated intensively (e.g., Farrar et al. 1994, Liu and Kogan 1996, Adegoke and Carleton 2002, Wang et al. 2007, Schnur et al. 2010). These studies found that NDVI and soil moisture are significantly correlated. In recent years, fusion models have emerged for computing soil moisture index by analyzing the NDVI-LST relationship. The scope of these investigations was to emphasize the importance of improving the spatial and temporal resolution of soil moisture products for accurately enhancing many agricultural and agroclimatic applications such as agriculture monitoring, drought and flood analysis, and natural resource reservations. Zhong et al. (2018) adopted downscaling technique for soil moisture retrieving using microwave soil moisture products whereas Xu et al. (2018) employed a downscaling method based on MODIS/Landsat fusion algorithm for retrieving surface soil moisture. These studies used in-situ soil moisture measurements for validating remote sensing data.

Apart from estimating soil moisture from NDVI-LST relationship space, several previous studies (e.g., Hills and Reynolds 1969, Hawely et al. 1983, Westren et al. 1999, Mohanty et al. 2000, Mohanty and Skaggs 2001) have been conducted for analyzing soil moisture in heterogeneous environments. The relationship between soil moisture patterns and other environmental factors such as topography and vegetation has been intensively studied on different spatial and temporal scales. Early attempts were conducted by Hills and Reynolds (1969) to find a relationship between soil moisture and slope and found that no significant relationship existed. In a small agricultural watershed, however, Hawely et al. (1983) found that the variation of soil moisture was greatly affected by the topography factor. This result was also found by Mohanty et al (2000). Grabs et al. (2009) developed a new wetness index to show its capacity to truly predict the spatial distribution of soil moisture. Soil moisture dynamic concerning the land cover was also investigated. In complex terrain with mixed vegetation, Hawely et al. (1983) found that temporal soil moisture tends to be more stable in comparison with sparse vegetation.

To determine the relationship between moisture and environmental factors (temperature, topography, and vegetation), various statistical approaches were used. These approaches can be categorized into descriptive and analytical statistics such as mean, variation coefficient, standard deviation, correlation and regression, and geostatistical analysis (e.g., Qiu et al. 2001, Brocca et al. 2010). The influence of the environmental variables on soil moisture can be determined using intrinsic methods such as principal component analysis (Zhang and Oxley 1994). The extrinsic methods, on the other hand, are divided into linear (e.g., canonical correlation analysis) and nonlinear such as canonical correspondence analysis (Qiu et al. 2001). Although both linear and nonlinear methods are powerful in relating the soil moisture pattern to environmental factors, the nonlinear methods have been proven to be more robust than the linear methods (Zhang and Oxley 1994, Qiu et al. 2001). In a similar environment, Ibrahim et al (2021) evaluated the influences of LST on NDVI, SMI, normalized difference water index (NDWI), and dry bare soil index (DBSI) using a series of Landsat and MODIS images. The results showed that the SMI decreased by around 44 % in 2019 compared with those 1990. Using correlation analysis techniques, Jaber (2018) investigated the relationships between vegetation abundance and LST in different seasons in the years 1987 and 2016 in urban areas in Greater Amman Municipality. The results showed a negative relationship between vegetation abundance and LST in summer, while a positive relationship was found in winter. Jaber (2021) also demonstrated the relationship between NDVI and daytime and nighttime LST in Jordan based on MODIS data in different seasons in 2017. The results showed that the variability in NDVI can be explained by land cover. However, the variation in the daytime and nighttime LST can slightly be correlated to the variation in land cover.

The main objective of this study is to infer the spatial variation of soil moisture over a heterogeneous environment in northern Jordan based on integrated ground soil data and remote sensing data. To improve the spatial and temporal resolution of soil moisture products, remote sensing data including MODIS and Landsat-8 data are fused using the STI-FM technique (Hazaymeh and Hassan, 2015a, b). More specifically, this study aims to (i) investigate the relationship between the normalized difference vegetation index (NDVI) and land surface temperature (LST) using high spatiotemporal fused data (ii) estimate soil moisture at high spatial and temporal scales, (iii) validate the estimated remote sensed-based soil moisture with ground-based soil moisture, and (iii) demonstrate the variation of the observed and estimated soil moisture in both spatial and temporal dimensions.

2. Material and methods

2.1 Study area

The study area is in the northern part of Jordan (32° 23′ to 32° 28′ N and 35° 49′ and 36° 2′ E) with an approximate area of 50 km^2 (Figure 1). This study area was chosen because it has heterogeneous characteristics in terms of topography, climate, vegetation, and soil. Thus, soil moisture is subject to wide variations within a short distance and time. The characteristics of vegetation and soil type provided below were observed during our soil sampling campaigns which were conducted between November 2019 and May 2020.

Geographically, the study can be divided into three parts:

(1) The hillslope area is in the western part of the study area and has a topography that varies from complex to moderate relief with elevation ranges between 600m and 1150 m above mean sea level. The climate is characterized by hot-dry summer and modest wet winter. The annual averages of rainfall and temperature are 580 mm and 14.4 °C, respectively. These vegetation types are natural vegetation such as wild pistachios (Pistacia Atlantica), evergreen oak (Quercus ilex), pine (Pinus), Carbo tree (Ceratonia siliqua), and wild strawberry (Fragaria vesca) common, as well as cereal crops (e.g., Wheat (Triticum), barley (Hordeum vulgare), and lentil (Lens culinaris)) and orchards (Olives (Olea europaea), apple (Malus Domestica), nectarine (Prunus persica var. nucipersica), peach (Prunus persica), and vine (Vitis)), particularly in the moderately sloped areas. Soil types consist of fine and coarse textures with predominantly clay, silt, and loam.

(2) The gentle-sloped area is in the eastern part of the study area and has moderate relief with elevation ranges between 500 to 800 meters above mean sea level. The climate is a transition from sub-humid to semi-arid with annual averages of rainfall and temperature of 140 mm and 16.9 °C, respectively. In almost all months, the precipitation in this area is less than the evaporation. The vegetation and land cover include grass and pasture; thus, a huge part of this area is allocated for grazing. In the areas located close to the sub-humid climate, Wheat (Triticum), barley (Hordeum vulgare), and lentil (Lens culinaris) crops are cultivated. The soil type is a coarse and fine texture with sand and loam.

(3) The plain area is located between the abovementioned areas. It has moderate climate conditions with annual average precipitation and temperature of 460mm and 17.8 °C, respectively. It is characterized by simple topography with elevation ranges between 450 to 650 meters above sea mean level. Clay soil is predominant with small patches of silt and loam. Agricultural lands include orchards which consist mainly of Olives (Olea europaea), apples (Malus Domestica), nectarine (Prunus persica var. nucipersica), peach (Prunus persica), and vine (Vitis)), and the dominant crops including Wheat (Triticum), barley (Hordeum vulgare), and lentil (Lens culinaris) which occur in most parts of this part of the study area.

Figure 2 which shows the elevation and slope (degrees) in the study area, was derived from Aster Global Digital Elevation Model (DEM) with a 30-meter resolution (https://search.earthdata.nasa.gov/search). The percentage of variations of sand, clay, and silt was interpolated using ordinary kriging based on the observed soil data during our sampling campaign (Figure 3). As can be seen, the heterogeneity of the landscape features in the study area would in turn have a significant effect on the spatiotemporal variation of soil moisture.

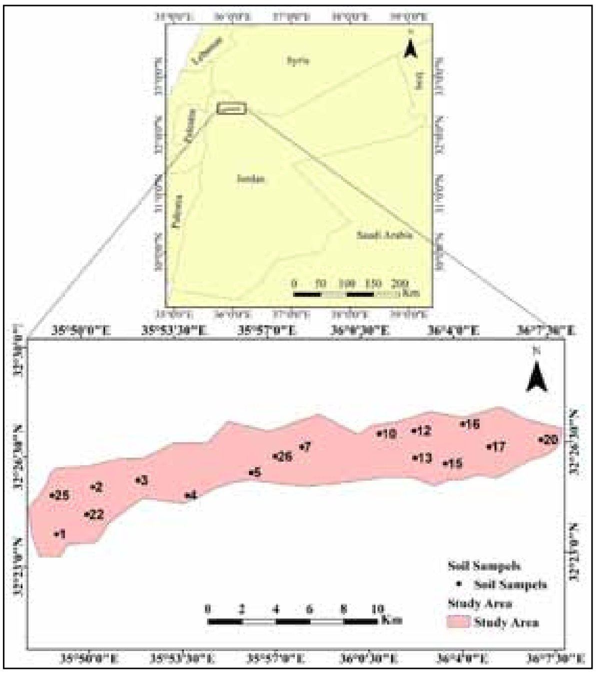

Figure 1. The geographic extent of Jordan (up) and the geographic extent of the study area with soil sample locations (bottom).

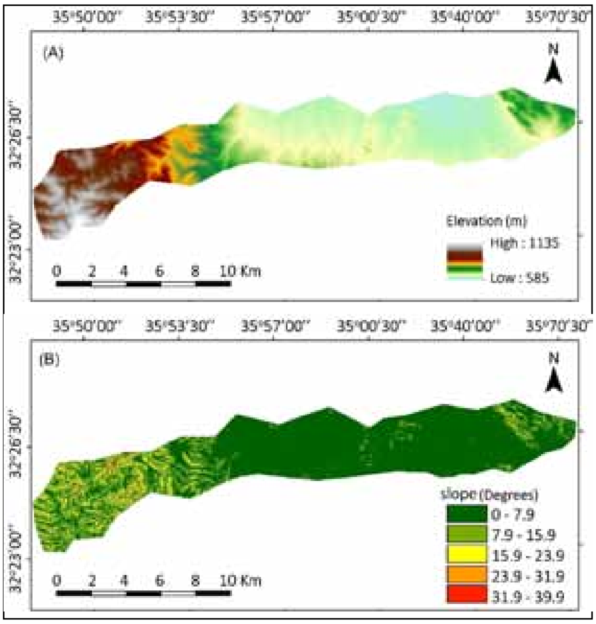

Figure 2. SRTM-30m digital elevation model (A), and the generated slope (B) of the study area

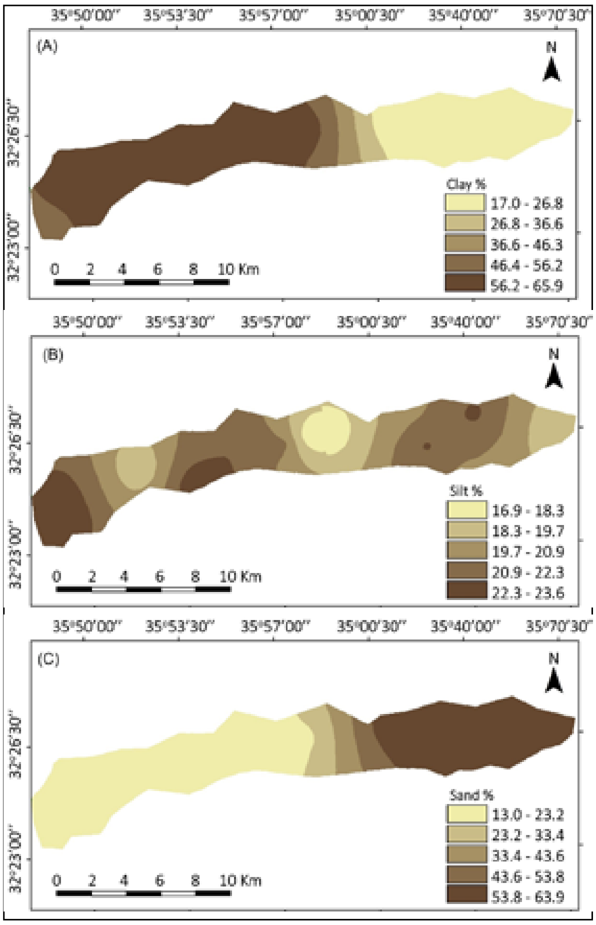

Figure 3. Soil texture characteristics based on soil textural triangle, percentage of clay (A), silt (B), and sand (C) in the study area

***In Situ* measurements**

Soil data were collected from 16 sample locations spread over the study area (Figure 1) at depth of 10 cm. Table 1 shows the description of soil samples, soil moisture %, and the soil type for each sample location. Field visits were conducted once a month from November 2019 to May 2020. The position of each soil sample was determined using a real-time kinematic (RTK) receiver with approximately 3cm level accuracy. It is worth mentioning that the following restrictions have been considered during soil samples collection:

- In the case of the hilly area, the samples were taken on a gentle slope and the steep slope was avoided because the soil depth is very shallow.
- during rainfall events, sampling was suspended.
- All soil samples were taken in rainfed areas, thus irrigated areas were avoided.
- The minimum distance between sample locations was at least 2 km to avoid homogeneity of topography, vegetation, and soil.
- To avoid human activities such as industrial, trading, and irrigated agriculture which may influence the soil, built-up areas (urban areas), road networks, and dense tree canopy were avoided.

After soil samples were collected, soil moisture was computed in the laboratory using the volumetric soil moisture method. In this method, each soil sample was weighed before and after oven drying. Then the water content in each sample was converted to a percentage value. The volumetric method was selected due to its simplicity, robustness, and low technical work required to derive the soil water content (Robock et al. 2000, Seneviratne et al. 2010). Therefore, it is widely used for calibrating indirect methods such as neutron probes (Almagbile et al. 2019).

Table 1. Description of the sixteen soil samples used to calculate the reference soil moisture measurements in this study

Sample	Location ID	X	Y	SM %	soil type	LULC
1	7	32.40123	35.81503	18.4	clay	Grass
2	26	32.42580	35.83848	16.6	clay	bare soil
3	16	32.42877	35.86696	19.3	clay	bare soil
4	10	32.42002	35.89748	16.5	clay	bare soil
5	12	32.43119	35.93785	17.7	clay	wheat crop
6	20	32.44408	35.97006	13.5	clay	bare soil
7	17	32.44988	36.01881	12.8	sand-loam	grass
8	13	32.45095	36.04061	12.2	sand-loam-clay	grass
9	15	32.43652	36.04082	13.9	sand-loam	grass
10	5	32.43306	36.05966	9.8	sand-loam-clay	grass
11	2	32.45389	36.07126	10.9	sand-loam	grass
12	3	32.44138	36.08727	9.5	sand-loam	grass
13	25	32.44432	36.11991	9.3	sand-loam	grass
14	4	32.41133	35.83432	19.1	clay	orchard
15	22	32.42196	35.81295	18.0	clay	orchard
16	1	32.43943	35.95331	15.2	clay	orchard

Remote Sensing Datasets

NDVI and LST

Table 2 illustrates the characteristics of the remote sensing dataset that has been used in this study. Two types of datasets were used (i) MODIS collections (i.e., MOD13Q1 and MOD11A2). The MOD13Q1 collection provides the composite NDVI values over 16 days at 250m spatial resolution where cloud-free global coverage is achieved by replacing clouds with the historical MODIS time series climatology record. The MOD11A2 provides composite 8-day LST data at 1km spatial resolution. The MOD11A2 collection comprised daytime and night-time LSTs, quality assurance assessment, observation times, view angles, bits of clear sky days and nights, and emissivity estimated using the spectral bands 31 and 32 concerning land cover types. (ii) The Landsat 8 Operation Land Imager (OLI) and Thermal Infrared Sensor (TIRS) at 30m spatial resolution. Here, the red (0.64-0.67 μm), near-infrared (0.85-0.88 μm), and thermal (10.6-11.19 μm) spectral bands were used to calculate the NDVI and LST maps.

Table 2. Characteristics of remote sensing dataset used in this study

Satellite	MODIS 8day composite		Landsat-8 (L8)	
Product	NDVI	LST	NDVI	LST
Collection	MOD13Q1	MOD11A2	Level 2	Level 2
Type	16-day composite	8-day composite	individual day	individual day
Spatial Resolution	250m	1000m	30m	30m
Spectral bands	Red and NIR	TIR 31 and 32	Red and NIR	TIR 10
MODIS Day of the Year, L8 Acquisition date	**2019**: 329, 337, 345, 353, 361 **2020**: 001, 009, 025, 033, 041, 0.49, 057, 065, 072, 081, 089, 097, 105, 129		2019/11/26, 2020/02/14, 2020/04/02, 2020/04/18, 2020/05/04, 2020/05/20	
Path/Raw	v05/h21		174/037	
Sources	Google Earth Engine			

Data processing

In this study, original NDVI and LST images were used to generate synthetic Landsat-like NDVI and LST by fusing the original MODIS and Landsat 8 using the STI-FM model. The fusion of MODIS and Landsat 8 allows the generation of synthetic images at the spatial resolution of Landsat 8 (i.e., 30m) and the temporal resolution of the MODIS product. From the relationship between the LST and NDVI, the soil moisture index is retrieved.

Calculating NDVI and LST using a data fusion model

STI-FM is a recently developed model that used two MODIS images taken at time one and time two, and one Landsat image taken at the time one [$L_{(t1)}$] to generate a synthetic Landsat surface reflectance and land surface temperature image at time two. The STI-FM model begins with determining the rate of the temporal change in spectral signatures between the two MODIS images at times one and two. Based on this relationship, the temporal changes might be either positive or negative change. In some cases, however, no change could be identified. In the second step, a linear relationship between the MODIS images for each case of change is developed (Hazaymeh and Almagbile 2018). Finally, a synthetic Landsat surface reflectance or surface temperature image at time two $synth\_L(t_2)$ is generated using the regression coefficients computed in the second step as follows:

$$synth_{L(t_2)} = a * L_{(t1)} + c \quad \text{(1)}$$

where a and c are the slope and intercept, respectively. Note that STI-FM has been validated in previous work and used in developing a remote sensing-based agricultural drought indicator and successfully implemented over a semi-arid region in Jordan.

Soil Moisture Index

Early studies (Carlson 1986, Gillies, and Carlson 1995) used the vegetation index/temperature (VIT) trapezoidal shape for determining soil moisture index (Figure 4).

The trapezoidal shape in the Ts-VIs scatters plots emerge due to the negative relationship between these two variables. For instance, Ts have low sensitivity to the variation of water content over vegetated areas, while it has high sensitivity over bare soils. For example, a non-water stress condition can be identified when the VIs values increase along the x-axis while the Ts values decrease along the y-axis. This is due to the cooling effects of evapotranspiration, and vice versa. In the Ts-VIs scatter plot, the VIs and Ts are represented on the x-axis and the y-axis, respectively. Referring to Figure 4, the theoretical dry edge that represents the water stress condition is defined along the edge that connects the *no evaporation* and the *no transpiration* points. While the theoretical wet edge, which represents the well-watered condition, is defined by the horizontal line that connects the *maximum evaporation* and the *maximum transpiration* points. In Figure 4, values along the Ts axis reflect the effects of water content and topography over the bare lands, while values along the VIs axis show the effects of the water content and vegetation density over the vegetative land. The values inside the trapezoidal shape represent varying vegetation cover between the bare lands and dense vegetation. Note that the trapezoidal shape might be affected by many factors including, (i) evaporation levels; (ii) vegetation density and moisture status; (iii) local climate; (iv) the number of pixels in the scene; and (v) other specific study area characteristics such as topography, soil type, spatial heterogeneity, and latitude. In Figure 4, the dry condition appears in the upper envelope of the trapezoid, A–C, a.k.a "warm edge" whereas the "cold edge" occurs in the lower limit of the trapezoid, B–D. Soil moisture index can be retrieved from the relationship between the LST and NDVI based on the location of a pixel in the LST-NDVI space defined in a scatter plot. Therefore, the soil moisture index ranges between 0 at the "warm edge" and 1 at the "cold edge" (Zhan et al. 2004, Parida et al. 2008). The SMI for a given pixel (LST, NDVI) in the LST-NDVI space can be retrieved as (Sandholt et al. 2002):

$$SMI = \frac{T - T_{min}}{T_{max} - T_{min}} \quad (2)$$

Where T_{max} and T_{min} represents the maximum and minimum slopes of the trapezoid and can be respectively calculated as:

$$T_{max} = a_1 * NDVI + b_1 \quad (3)$$

$$T_{min} = a_2 * NDVI + b_2 \quad (4)$$

where a_1, a_2, and b_1, b_2 are the regression coefficients.

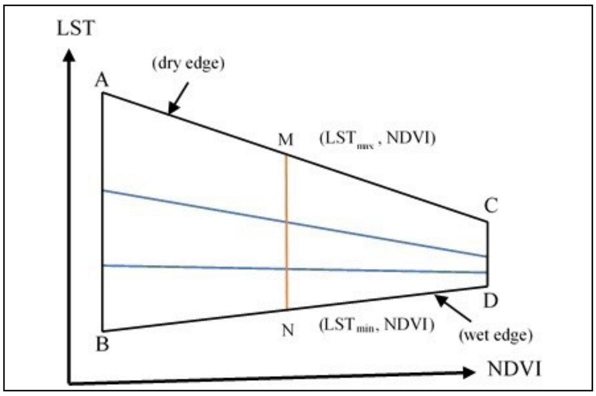

Figure 4. The trapezoidal shape illustrates the relationship between NDVI and LST for estimating soil moisture (after, Zhan et al. 2004)

Data processing

In this study, original NDVI and LST images were used to generate synthetic Landsat-like NDVI and LST by fusing the original MODIS and Landsat 8 using the STI-FM model. The fusion of MODIS and Landsat 8 allows the generation of synthetic images at the spatial resolution of Landsat 8 (i.e., 30m) and the temporal resolution of the MODIS product. From the relationship between the LST and NDVI, the soil moisture index is retrieved.

Statistical analysis

The variation of soil water content in both spatial and temporal scales was determined using statistical analysis such as the spatial and temporal mean, standard deviation, and variation coefficient. The spatial and temporal mean of soil moisture can be respectively calculated as follows (Brocca et al. 2010):

$$\bar{\theta}_j = \frac{1}{N}\sum_{i=1}^{N}\theta_{ij} \quad (5)$$

$$\bar{\theta}_i = \frac{1}{M}\sum_{j=1}^{M}\theta_{ij} \quad (6)$$

Where θ_{ij} is the soil moisture in location (point) i and sampling day j, N, and M are the number of measured points and sampling days, respectively? The coefficient of variation $C.V$ for both spatial ($C.V_i$) and temporal ($C.V_j$) can be calculated respectively as (Brocca et al. 2010):

$$C.V_i = \frac{\sigma_i}{\bar{\theta}_i} = \frac{\sqrt{\frac{1}{N-1}\sum_{i=1}^{M}(\theta_{ij} - \bar{\theta}_i)^2}}{\bar{\theta}_i} \quad (7)$$

Where σ_i and σ_j are the standard deviation of the spatial and temporal soil moisture?

$$C.V_j = \frac{\sigma_j}{\bar{\theta}_j} = \frac{\sqrt{\frac{1}{N-1}\sum_{j=1}^{N}(\theta_{ij} - \bar{\theta}_j)^2}}{\bar{\theta}_j} \quad (8)$$

The temporal persistence of soil moisture, relative to point i and time j, is given by (Brocca et al. 2010)

The mean relative difference (MRD) and its standard deviation (SDRD) over the sampling time can be computed as:

$$\delta_{ij} = \frac{\theta_{ij} - \bar{\theta}_j}{\bar{\theta}_j} \quad (9)$$

$$\bar{\delta}_i = \frac{1}{M}\sum_{i=1}^{M}\delta_{ij} \quad (10)$$

$$\sigma_i(\delta_i) = \sqrt{\frac{1}{M-1}\sum_{i=1}^{M}(\delta_{ij} - \bar{\delta}_i)^2} \quad (11)$$

The relationship between the SMI and observed soil moisture from *in-situ* measurements was computed using simple regression analysis. Then, the coefficient of determination (R^2) and the root of mean squared error (RMSE) were used as evaluation metrics of the results using the following equation:

$$r^2 = \left[\frac{\sum(A_{(t)} - \overline{A_{(t)}})(S_{(t)} - \overline{S_{(t)}})}{\sqrt{\sum(A_{(t)} - \overline{A_{(t)}})^2}\sqrt{\sum(S_{(t)} - \overline{S_{(t)}})^2}}\right]^2 \quad (12)$$

$$RMSE = \frac{\sqrt{\sum S_{(t)} - A_{(t)})^2}}{N} \quad (13)$$

Where $A_{(t)}$ and $S_{(t)}$ are the actual and the synthetic Landsat-8 surface reflectance images $A_{(t)}$ and $S_{(t)}$ are the mean values of the actual and the synthetic Landsat-8 images, and N is the number of observations.

Geostatistical analysis

To demonstrate the Spatiotemporal pattern of the observed and estimated soil moisture, a geostatistical interpolation technique based on the Ordinary Kriging- semi-variogram function is used. The semi-variogram provides a basic tool for examining spatial autocorrelation as a function of the distance between observations (Romshoo 2004). Generally, the theoretical semi-variogram consists of different models namely linear, spherical, circular, exponential, and Gaussian. The mathematical expression to estimate the semi-variance is defined as (Olea 1999; Webster 2001):

$$y(x) = \frac{1}{2n_h}\sum_{i=1}^{n_h}[z(x_i + h) - z(x_i)h]^2 \quad (14)$$

where $y(x)$ is the empirical semi-variogram; $z(x_i + h)$, $z(x_i)$ is the soil moisture values at sample points x_i *and* $x_i + h$, spaced apart at distance h; n_h is the number of pairs (x_i, $x_i + h$)

of soil moisture values at points spaced at distance, used for calculating the semi-variogram function.

Normally, the experimental semi-variogram consists of a nugget, sill, and range. The nugget values do not approach zero at the origin y-axis due to the spatially uncorrelated noise or error in observations, (Kitanidis 1997). The range is a distance where the semi-variogram model first flattens out whereas the sill is a value that the semi-variogram model attains at the range.

The most suitable semi-variogram model is the one that achieves the smallest RMS error between the semi-variance values obtained from the observed soil data and the theoretical model that predicts the semi-variance values. Following published research (e.g., Romshoo 2004; Kumar et al. 2014), the spherical model has been found the best model that achieves the smallest RMSE between the actual and theoretical model computed semi-variance values. Thus, this study employed the spherical semi-variogram model for determining the spatiotemporal pattern of soil moisture. The spherical semi-variance models can be given as (Kumar *et al.* 2016, Romshoo 2004)

$$\gamma(x) = \begin{cases} 0, & h = 0 \\ C_0 + C\left(\frac{3}{2}\frac{h}{a} - \frac{1}{2}\frac{h^3}{a^3}\right) & 0 < h \le a \\ C_0 + c & h > a \end{cases} \quad (15)$$

The parameters, C_0 and a denote nugget and effective range respectively, $C_0 + C$ is the sill, and C is the partial sill.

3. Results and discussion

NDVI-LST space for retrieving SMI

The NDVI-LST space using synthetic images derived from the STI-FM data fusion algorithm was used for retrieving monthly surface soil moisture for the growing season from November 2019 to May 2020 in the study area. The computed SMI reflects the vegetation and temperature conditions in the study area. From Figure 5, the NDVI-LST space showed trapezoidal shapes. As such increase in NDVI values reflects a decrease in the LST values and vice versa. As shown in Figure 5, the relationship between the NDVI-LST is clear in wet and cold months (November to March). On the contrary, the situation is different in the warm months (April and May) as an increase in LST joined with an increase in NDVI in the study area. This situation can be seen when comparing the trapezoidal shapes in these months. This can be related to the increase in LST which in turn causes an increase in evapotranspiration and hence a reduction of soil water content and vegetation cover. As a result, the retrieved SMI based on the relationship between the NDVI and LST reflects a realistic soil water content during the wet and cold months compared with those of the warm and dry months.

Figure 6 shows the spatial distribution of SMI in the study area during the study period. It showed the regions which exhibit a high level of soil moisture in five categories with equal interval breaks to emphasize the amount of soil moisture values relative to other values. Generally, the eastern part of the study area showed the lowest values of soil moisture while the central and western areas exhibit the highest. This might be due to (i) the variation in climate conditions as the eastern part observes higher temperatures and lower precipitation values than those for the western parts, (ii) soil properties which consisted of a higher percentage of sand in the eastern part compared to clay, silt, and loam in the central and western parts (see Figure 3). As a result, the SMI in the eastern part does not exceed 0.4 while it reaches more than 0.6 in the central and western parts in almost all the months of the study period. It can also be seen that the topography condition plays another crucial role in determining the SMI values in the study area. This predominantly occurs when comparing the SMI in the central part with those in the western part. Since the central part is almost a plain area that includes a clay texture and deep soil layer, the SMI was always larger than 0.4. On the other hand, the complex relief, mixed soil texture, mixed natural vegetation (e.g., evergreen oak and pine), and shallow soil layer controlled the SMI values in the western part.

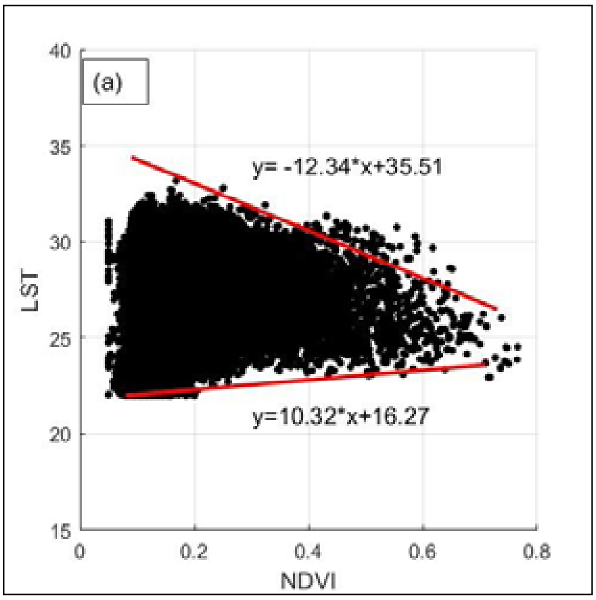

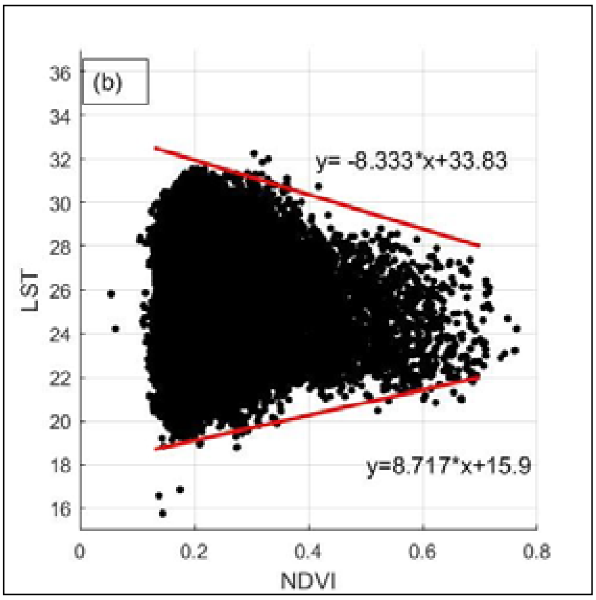

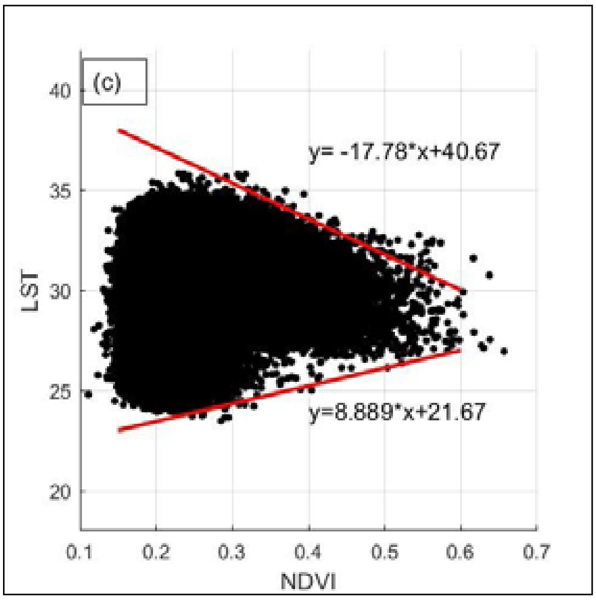

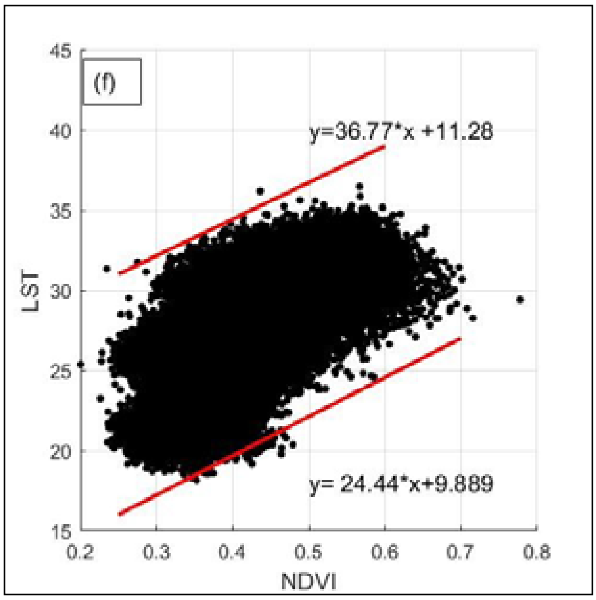

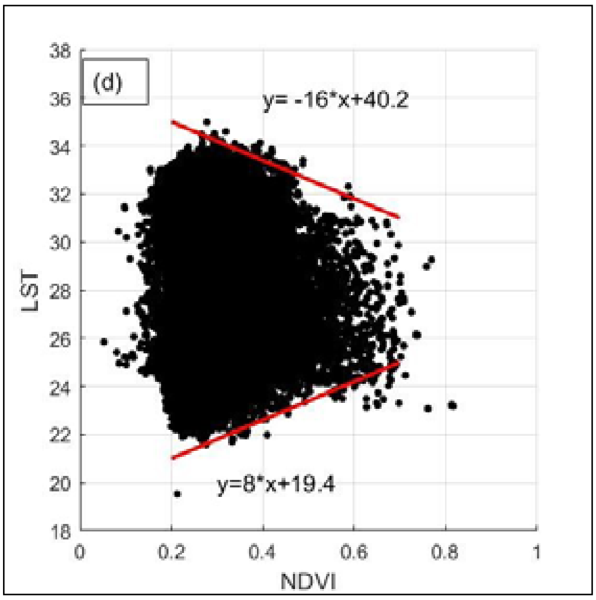

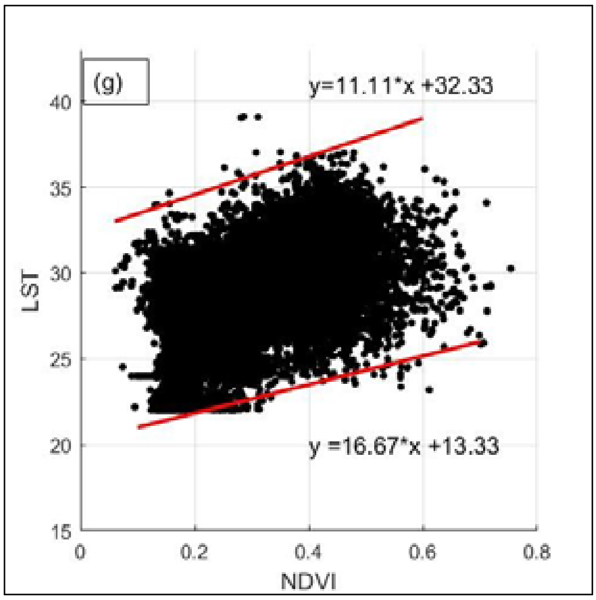

Figure 5. NDVI-LST space for (a) November, (b) December, (c) January, (d) February (e) March (f) April, and (g) May with maximum and minimum slope lines and regression coefficients

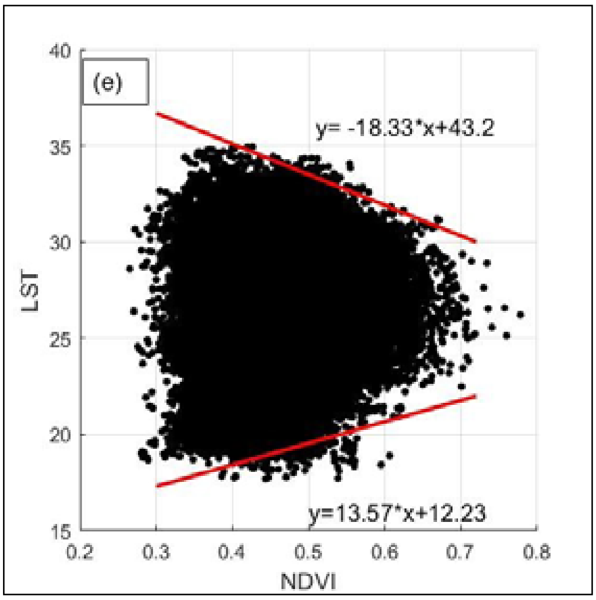

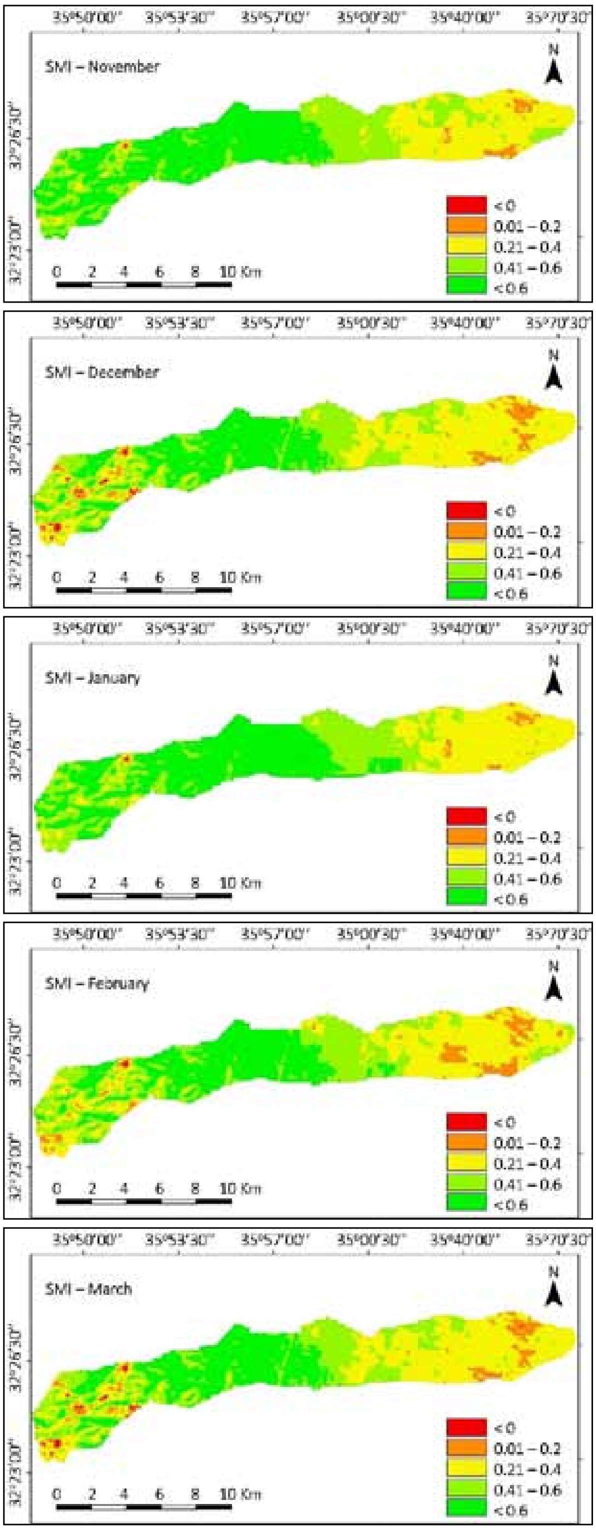

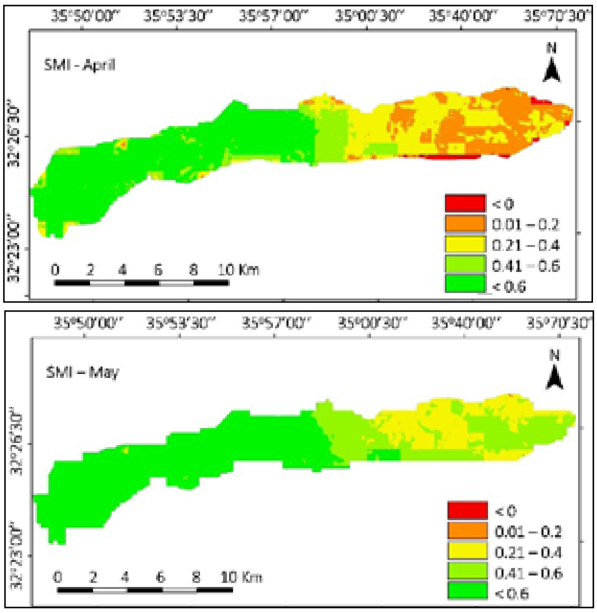

Figure 6. The spatial distribution of soil moisture index (SMI) during the study period from November 2019 to May 2020 in the study area

Soil moisture index and its validation

In this study, 16 *in-situ* measurements were used to validate the estimated SMI from synthetic Landsat 8 images. Figure 7 illustrates the relationship between the measured and estimated SMI along with the quantitative results of the determination coefficient (R^2) and root mean square error (*RMSE*). In general, the trend of the distribution of points was closely distributed to the regression line, this means that the estimated SMI results were close to the soil moisture *in-situ* measurements. Moreover, a moderate correlation between the estimated SMI and the *in-situ* measurements is obvious in the study area during the wet months such as 0.66, 0.62, and 0.49 in January, February, and April. Whereas weak correlation values were observed during November (0.38), December (0.38), and May (0.35). These results indicated that the value of SMI increases in wetter months (i.e., January and February) and decreases in lower precipitation (i.e., November and December) and warmer months (i.e., May). This means that a high amount of rainfall leads to an increase in the soil water content and hence enriches the vegetation cover. The RMSE values, on the other hand, ranged between 0.10 in January to 0.32 in May and thus it behaves oppositely with r^2 and confirmed its results.

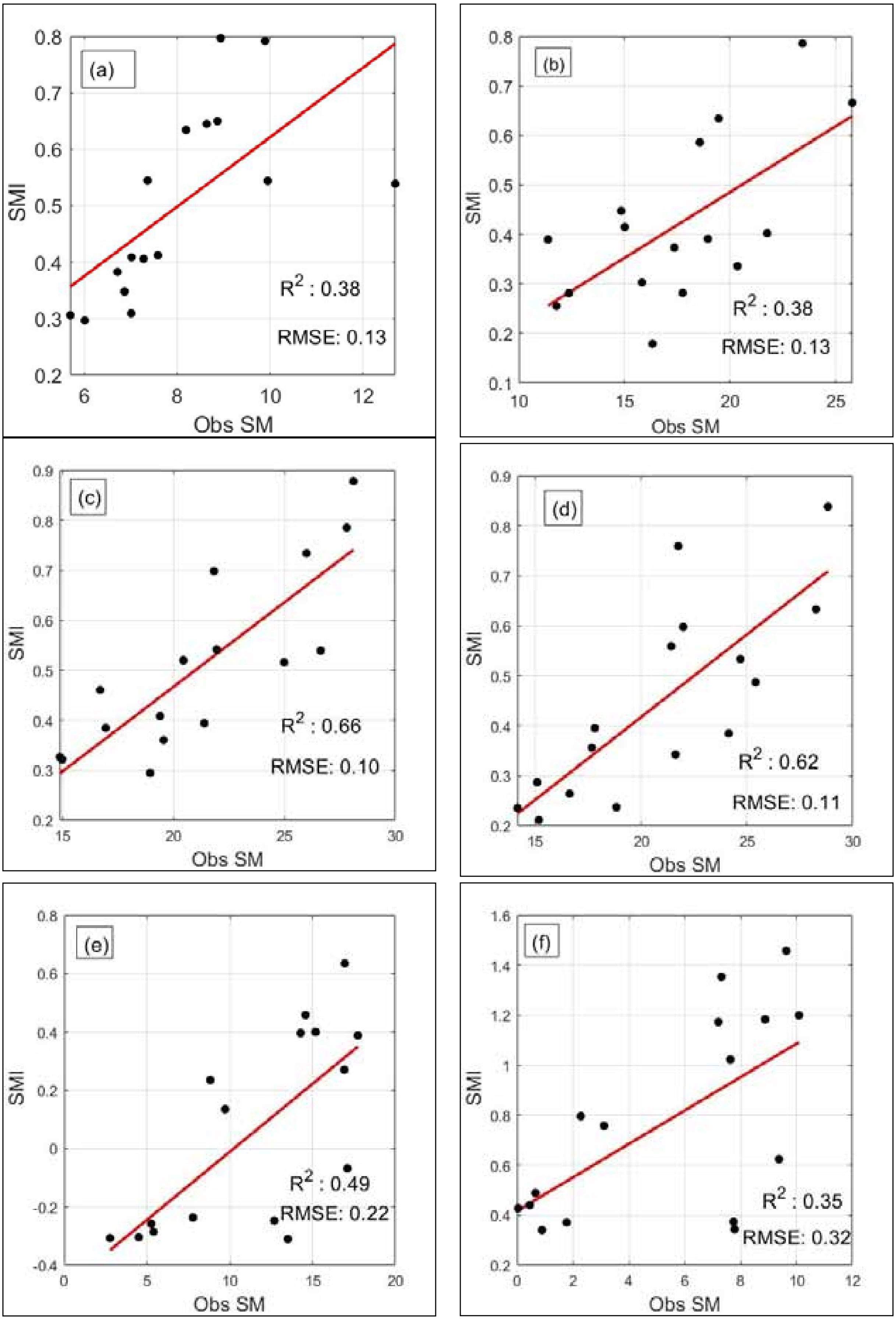

Figure 7. Relationship between observed soil moisture and estimated soil moisture index (SMI) in (a) November, (b) December, (c) January, (d) February, (e) April, and (f) May. Note that the in-situ measurements of soil moisture for March were not performed due to the Covid-19 lockdown restrictions in the study area.

Statistical analysis of the observed soil moisture and SMI

The variation of the soil moisture index, as well as observed soil moisture in both spatial and temporal dimensions, is statistically presented to illustrate whether both the SMI and observed soil moisture vary in a similar pattern. This includes spatial and temporal averages, standard deviation, variation coefficient, mean relative difference and root mean square error (RMSE). Figure 8 shows the temporal averages, the standard deviation, and the variation coefficient of the observed soil moisture and SMI of the 16 *in-situ* measurements. The temporal average in both the observed soil moisture and SMI was similar. This means that when the temporal average of observed soil moisture for a measurement point is high, it is also high for that point in the case of SMI and vice versa. For instance, the average in sample points 3-9 fluctuates between 9– 12% and 0.2-0.3 in the observed soil moisture and SMI, respectively. In both observed soil moisture and SMI, the average in these points was relatively less than the other data sample points. For the other sample points (10-16) the average ranges between 15 -20% in the case of the observed soil moisture, and thus it coincides with those in the SMI. The fluctuations of the temporal averages are attributed to the different climate conditions, topography, soil texture, and vegetation cover in the study area. The standard deviation reflects the temporal variations of soil moisture in the study area as such a huge change in soil water content of a point reflects a large standard deviation and vice versa. Overall, the standard deviation was relatively low in both observed soil moisture and SMI. In the case of the observed soil moisture, the variation coefficient showed that sample points 1-9 have high variations because their values range between 75-38% whereas the rest sample points have a steady stable variation with values ranging between 40-45%. For the SMI variation coefficient, the values were relatively high (around 100%) for sample points 3-9 while it was between 40-60% for the other sample points.

For the spatial analysis, the average, standard deviation, and variation coefficient for the observed soil moisture and the SMI are presented in Figure 9. The spatial average increases with the increase in rainfall and vice versa. Thus, for the observed soil moisture case, the highest spatial averages occurred in January and February during the study period. In these months, the spatial averages were 20% whereas the averages in November, December, April, and May were approximately 9, 17, 11, and 5%, respectively. For the SMI case, the averages ranged between 0.4 and 0.5 from November to the end of February, then it rapidly fell to approximately 0.1 in April and ended up at 0.7 in May. Since the relationship between the NDVI and LST controls the SMI, the growing season, which starts in November and extends until May, reflects an increase in SMI. In April, the evapotranspiration exceeds the precipitation, and therefore, the decay of vegetation causes a reduction of SMI. Notably, the high values of SMI in May are attributed to the vegetative propagation of the natural vegetation (e.g., pine, oak, and wild pistachios) and orchards (e.g., apricot, nectarine, and nuts). Since the variation of the spatial average in the observed soil moisture and SMI is relatively small, the standard deviation and variation coefficient values were steadily stable throughout the whole study period.

The results of temporal stability analysis including the mean relative difference (MRD), the RMSE, and standard deviation for the observed soil moisture and the SMI are depicted in Figure 10. The purpose of MRD is to compare the soil moisture value at a particular data point to the average over the study area. Thus, a point is deemed to be dry or moist if it is less or greater than zero, respectively. To determine whether the soil moisture in a point is in stable status or not, the standard deviation of mean relative difference (SDRD) is normally used. As such low SDRD represents temporal stability whereas a large SDRD indicates that the soil moisture in a point is not linearly related to the study area.

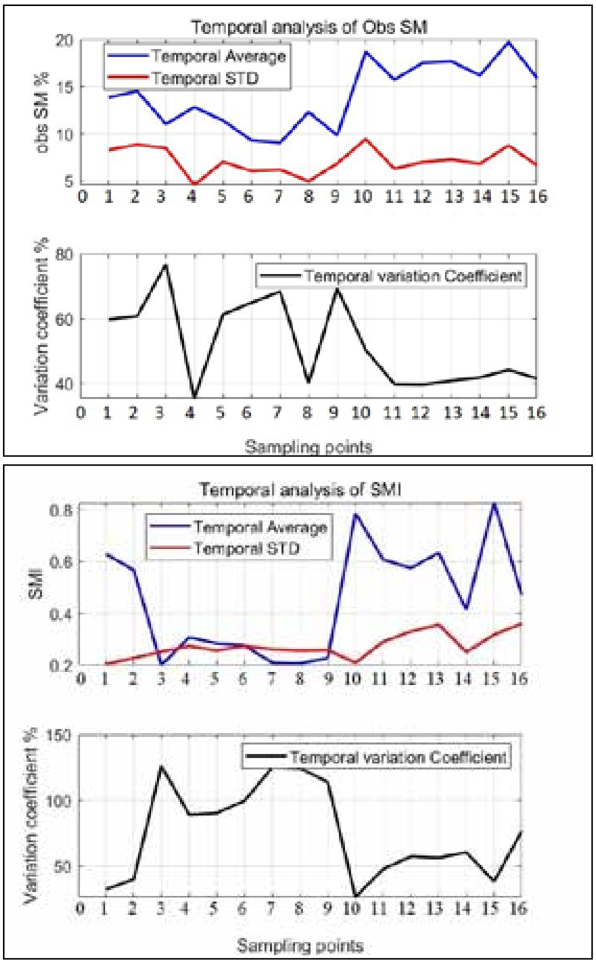

Figure 8. Temporal average, standard deviation, and variation coefficient for the observed soil moisture (up) and SMI (bottom)

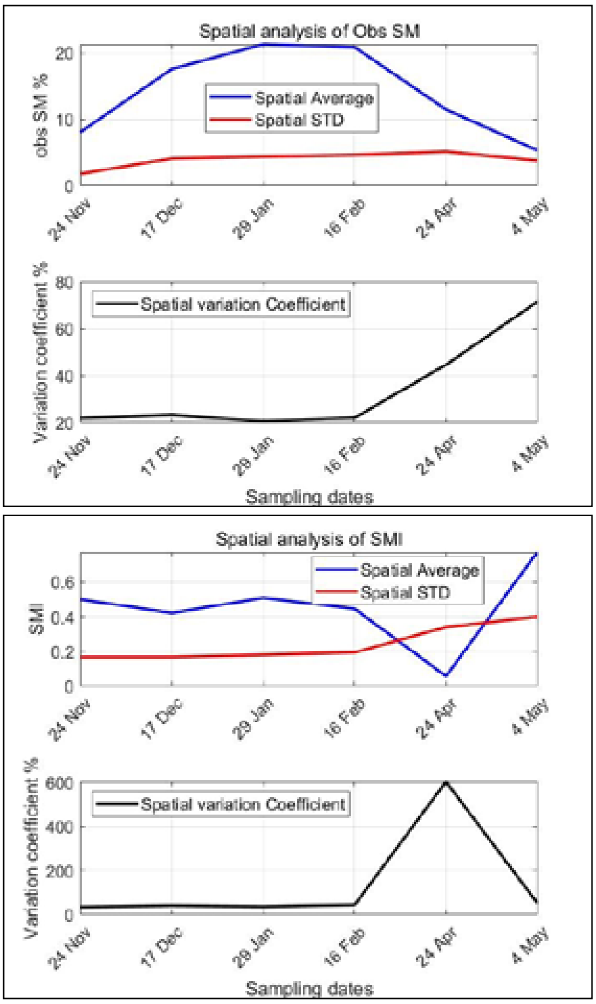

Figure 9. Spatial average, standard deviation, and variation coefficient for the observed soil moisture (up) and SMI (bottom)

In the case of the observed soil moisture, two groups can be found in terms of dry and moist status. The first group is dry and includes sample points 1-9 as their MRD values were below the mean (zero). The second group, on the other hand, consisted of sample points 10-16 which were found as moist samples as their MRD values were above the mean. This might be related to the location of the first group which represents a semi-arid area whereas the second group belongs to a sub-humid area. For the SMI, the situation was slightly different because sample points 3-9 and sample point number 14 had MRD values below the mean, while the rest of the data points had MRD values greater than the mean.

A clear image can be observed when comparing the values of SDRD and RMSE for each data point for both observed and SMI. For the observed soil moisture, the highest SDRD values (above 0.3%) were found for sample points 3, 7, 8, 12, 14, and 15, whereas the lowest SDRD values (0.15%) were noticed in points 10, 11, and 13. This means that the points which have low SDRD values were temporarily stable while the other data points exhibited large variations within a short time. In the case of the SMI, the opposite situation can be noticed for points 14 and 15 because their SDRD and RMSE values were different from those obtained by the observed soil moisture. Therefore, these data points were not linearly linked to the observed soil moisture.

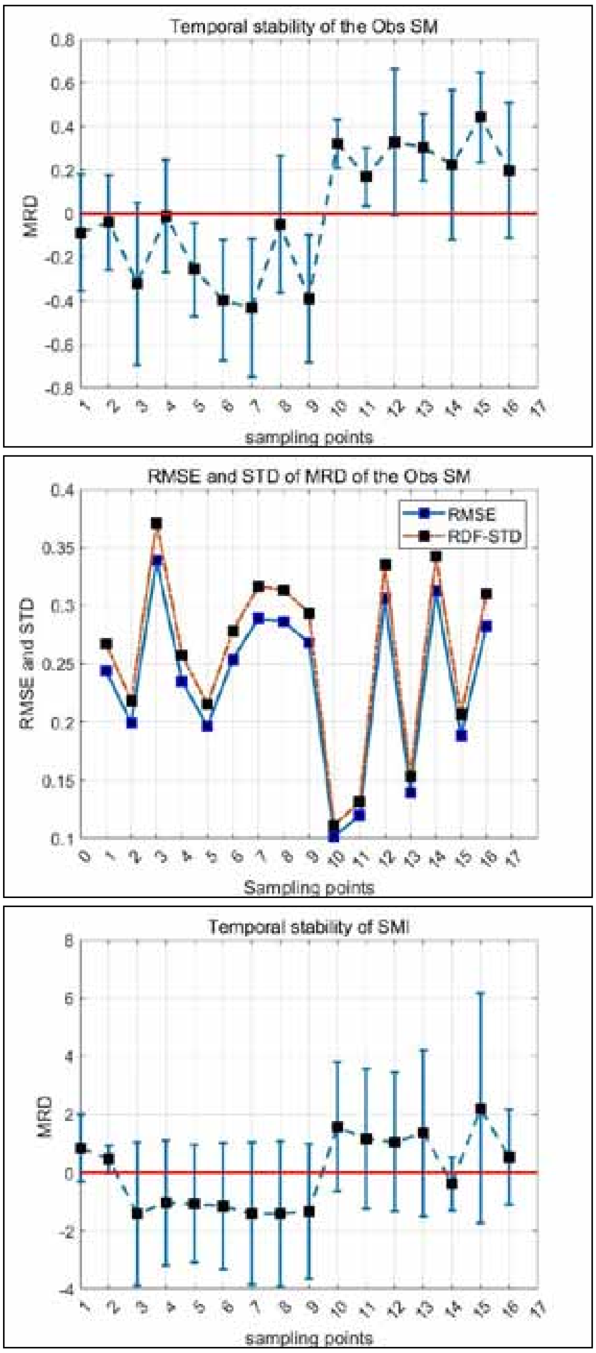

Spatiotemporal variability of soil moisture

Figure 11 shows the semi-variogram analysis of the 16 soil moisture locations over the whole study period. This is to clarify the spatial autocorrelation among soil moisture observations as a function of distance. As can be seen in Table 3, the minimum and maximum nugget values of 1.11 and 6.42 occur in November and April respectively. Since the nugget values were relatively high in some months, some factors other than the distance between observations influence soil moisture variability. The lowest sill values occur in the driest periods (November, April, and May) with values varying from 0.61 to 7.59. On the other hand, the sill values in December, January, and February (wet periods) are 18.30, 28.54, and 32.7 respectively. The range of correlation length varies from 10545 m in April to approximately 29428 m from November to February.

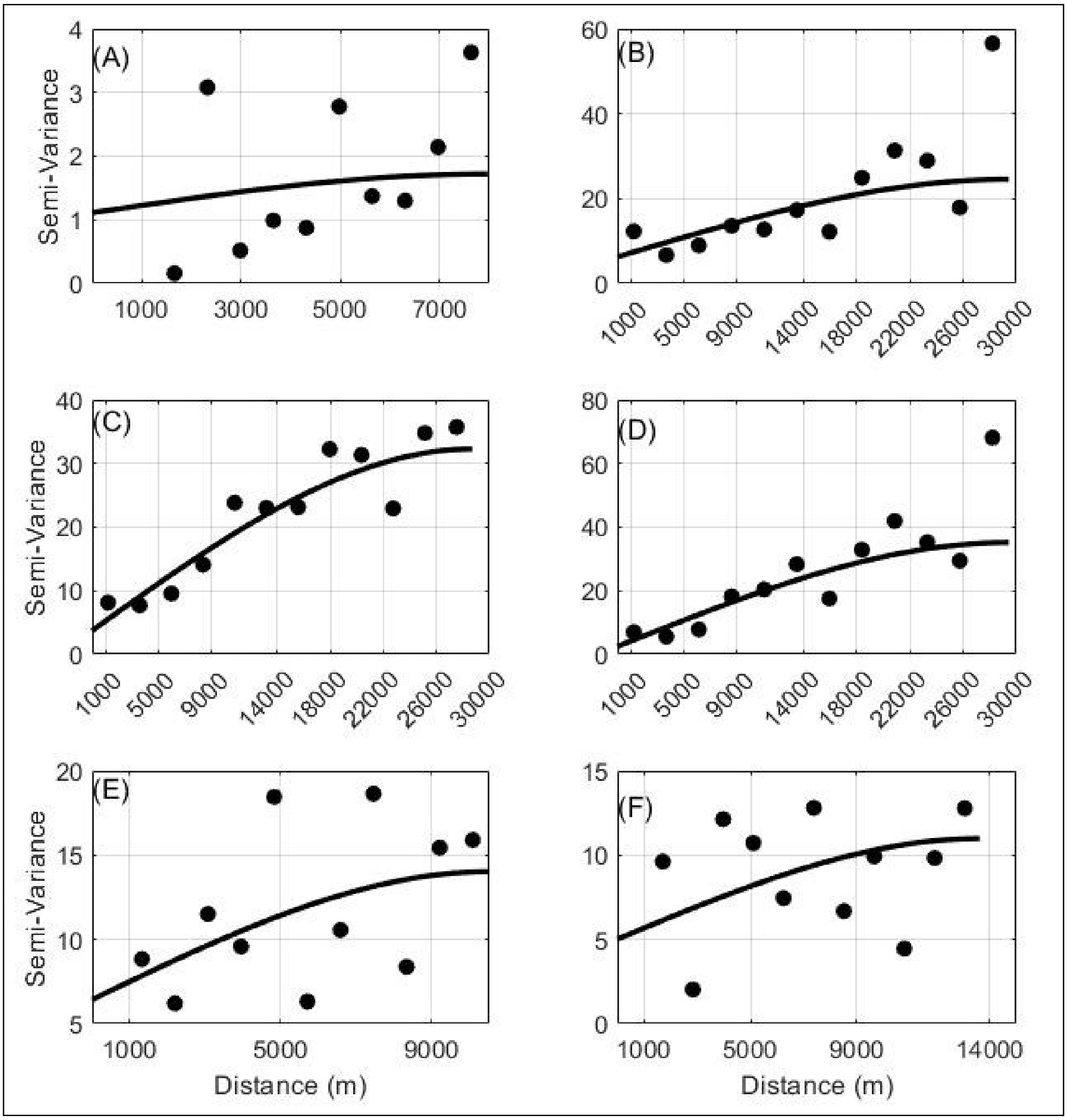

Figure 11. Semi-variogram analysis of the observed soil moisture in (A) November, (B) December, (C) January, (D) February, (E) April, and (F) May. The black dots represent the soil observations.

Table 3. Semi-variogram model elements (range, sill, and nugget) of the observed soil moisture samples over the study period (24th November 2020 to 15th May 2021)

date of sample observation	Nugget	Sill	Range (m)
24-Nov 2020	1.11	0.610	29428
17-Dec 2020	6.26	18.30	29428
29-Jan 2021	3.74	28.54	28718
18-Feb 2021	2.47	32.70	29428
24-Apr 2021	6.42	7.59	10545
15-May 2021	5.02	5.96	13630

For the case of SMI, the Analysis of the Spherical semi-variogram model is depicted in Figure 12 and Table 4. Throughout the study period, the nugget values varied from 0.001 to 0.009 and this reflects a tiny error in soil moisture observations. The sill values are opposite to those found in the case of observed soil moisture because the lowest values were observed during the wet period (December, January, and February) whereas the drier period, such as April and May, in particular, exhibit higher values. This reflects a larger correlation length (range) in the drier period and a shorter range during the wet period.

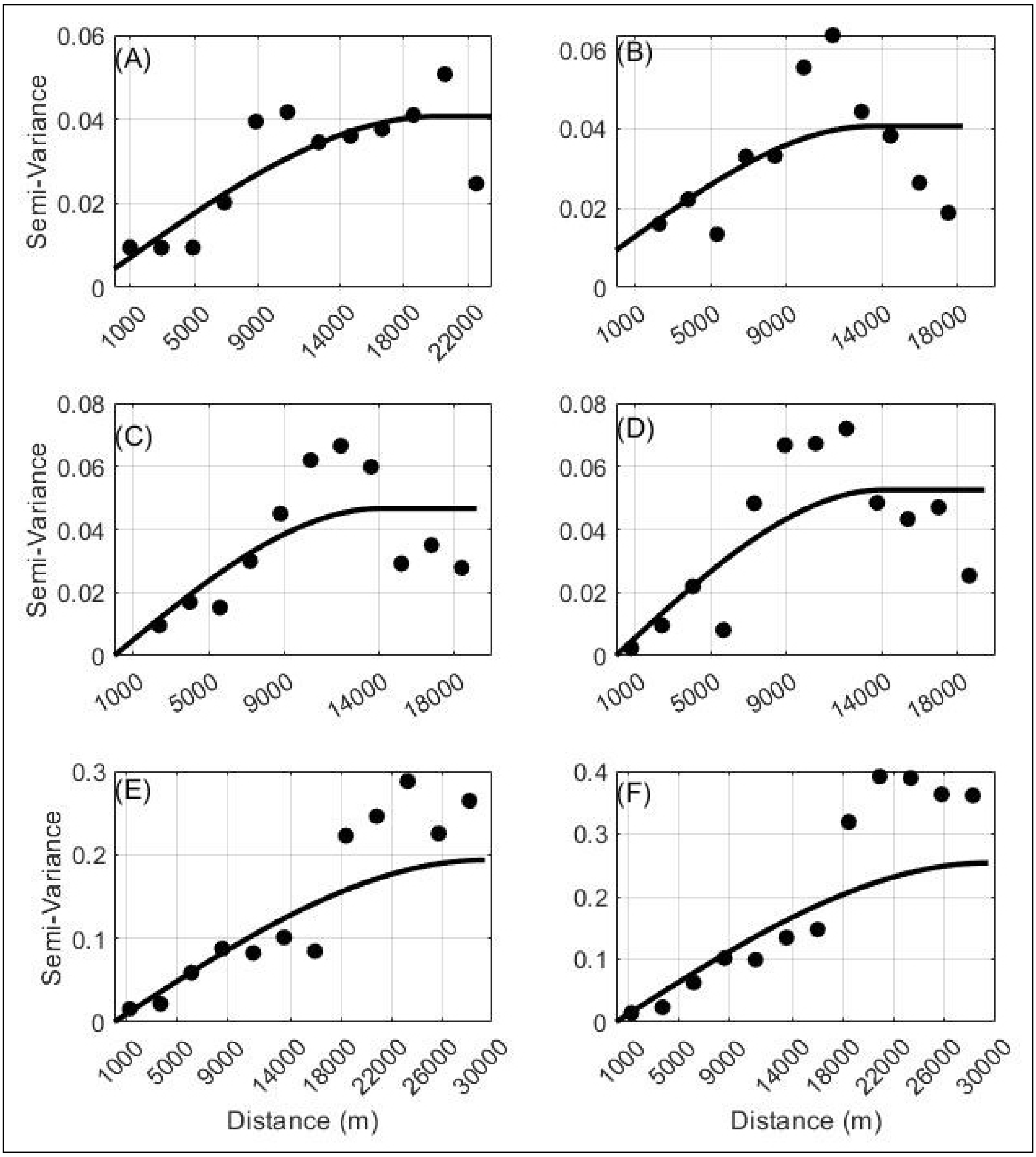

Figure 12. Semi-variogram analysis of SMI in (A) November, (B) December, (C) January, (D) February, (E) April, and (F) May. The black dots represent the soil observations.

Table 4. Semi-variogram model elements (range, sill, and nugget) of SMI over the study period (24th November 2020 to 15th May 2021)

date of images	nugget	sill	range
24-Nov	0.004	0.036268	20125
17-Dec	0.009	0.031228	13544
29-Jan	0.001	0.046645	14149
18-Feb	0.001	0.052551	14139
24-Apr	0.001	0.19372	29428
15-May	0.001	0.25382	29428

4. Conclusions

High spatial and temporal resolutions make satellite images valuable resources for soil moisture monitoring when the ground-based measurements are absent or not evenly distributed. However, due to the trade-off between spatial and temporal resolution of satellite data and the possibility of cloud contamination, new spatiotemporal data fusion techniques were developed and used to generate synthetic satellite-like images. In this context, STI-FM was used to generate synthetic NDVI and LST by fusing MODIS and Landsat 8 products. The correlation between the NDVI and LST images was tested and used to calculate the SMI over a heterogenous study area in northern Jordan during the growing season from November 2019 to May 2020. Results showed that the NDVI-LST relationship is an objective and robust metric for estimating and identifying the spatial distribution of soil moisture in the study area. The results also show a moderate correlation between the measured and SMI for the wetter months and a low correlation in the drier months. The high correspondence between SMI calculated based on the NDVI-LST relationship and independent in-situ metrics demonstrates the high potential of satellite images in monitoring and identifying the spatial distribution of soil moisture in the study area. Furthermore, the results of the semi-variogram analysis for the observed soil moisture show that the drier months have higher soil moisture variability than the wet months. For the case of SMI, the semi-variogram analysis showed no seasonal pattern of soil moisture variability. It was demonstrated that the NDVI-LST relationship and SMI are likely linked to a different climate, soil, and terrain properties in the study area which has a strong impact on spatiotemporal variability/stability of soil moisture.

References

Adegoke, J. O., and Carleton A. M. 2002. Relations between soil moisture and satellite vegetation indices in the US corn belt, J. Hydrometeorol., 3(4), 395– 405. doi:10.1175/1525-7541(2002)003<0395: RBSMAS>2.0.CO;2.

Almagbile, A., Zeitoun, M., Hazaymeh, K., Sammour, H., and Sababha, N. 2019. "Statistical analysis of estimated and observed soil moisture in sub-humid climate in north-western Jordan." Environ Monit Assess 191, 96. doi:10.1007/s10661-019-7230-9.

Beven, K., and Kirkby, M. 1979. "A physically based, variable contributing area model of basin hydrology." Hydrological Sciences Bulletin 24(1), 43-69. DOI: 10.1080/02626667909491834.

Bogena, H. R., Huisman, J. A., Oberdörster, C., and Vereecken, H. 2007. "Evaluation of a low-cost soil water content sensor for wireless network applications." Journal of Hydrology 344, 32–42. DOI: 10.1016/j.jhydrol.2007.06.032.

Brocca, L., Melone, F., Moramarco, T., and Morbidelli, R. 2010. "Spatial-temporal variability of soil moisture and its estimation across scales." Water Resources Research 46, 1-14. DOI: 10.1029/2009WR008016.

Carlson, T.N. 1986. "Regional-scale estimates of surface moisture availability and thermal inertia using remote thermal measurements." Remote Sens. Rev 1 (2), 197–247. DOI: 10.1080/02757258609532069.

Carlson, T. 2007. "An Overview of the "Triangle Method" for Estimating Surface Evapotranspiration and Soil Moisture from Satellite Imagery." Sensors 7: 1612–1629. doi:10.3390/s7081612.

Choi, M., and Y. Hur. 2012. "A Microwave-Optical/Infrared Disaggregation for Improving Spatial Representation of Soil Moisture Using AMSR-E and MODIS Products." Remote Sensing of Environment 124: 259–269. doi:10.1016/j.rse.2012.05.009.

Dorigo, W. A., Wagner, W., Hohensinn, R., Hahn, S., Paulik, C., Drusch, M., Mecklenburg, S., van Oevelen, P., Robock, A., and Jackson, T. 2011. "The International Soil Moisture Network: a data hosting facility for global in situ soil moisture measurements." Hydrology and Earth System Sciences 15, 1675–1698. doi.org/10.5194/hess-15-1675-2011.

Fan, L., Al-Yaari, A., Frappart, F., Swenson, J.J., Xiao, Q., Wen, J., Jin, R., Kang, J., Li, X., and Fernandez-Moran, R. 2019. "Mapping Soil Moisture at a High Resolution over Mountainous Regions by Integrating with Situ Measurements, Topography Data, and Modis Land Surface Temperatures." Remote Sens 11(6), 656. DOI: doi.org/10.3390/rs11060656.

Farrar, T. J., Nicholson, S. E., and Lare, A. R. 1994. "The influences of soil type on the relationships between NDVI, rainfall, and soil moisture in semiarid Botswana. II. NDVI response to soil moisture." Remote Sensing of Environment 50 (2), 121–133. DOI: 10.1016/0034-4257(94)90039-6.

Gao, F., Masek, J., Schwaller, M., and Hall, F. 2006. "On the blending of the Landsat and MODIS surface reflectance: predicting daily Landsat surface reflectance." IEEE Trans. Geosci. Remote Sens 44, 2207–2218. DOI: 10.1109/TGRS.2006.872081.

Gillies, R.R., and Carlson, T.N. 1995. "Thermal remote sensing of surface soil water content with partial vegetation cover for incorporation into climate models." J. Appl. Meteorol 34 (4), 745–756. doi: 10.1175/1520-0450(1995)034<0745:TRSOSS>2.0.CO;2.

Grabs, T., Seibert, J., Bishop, K., Laudon, H. 2009. "Modeling spatial patterns of saturated areas: a comparison of the topographic wetness index and a dynamic distributed model." J. Hydrol 373, 15–23. DOI: 10.1016/j.jhydrol.2009.03.031.

Hazaymeh K., and Almagbile A. 2018. "A comparative analysis of spatiotemporal data fusion models for Landsat and modis data." Int. Arch. Photogramm. Remote Sens. Spatial Inf. Sci., XLII-3,", 7–10 May, Beijing, China. 491–495, doi:10.5194/isprs-archives-XLII-3-491-2018.

Hawley, M.E., Jackson, T.J. & McCuen, R.H. 1983. "Surface soil moisture on small agricultural watersheds". Journal of Hydrology, 62: 179–200.

Hazaymeh, K., and Hassan, Q.K. 2015a. "Spatiotemporal image-fusion model for enhancing the temporal resolution of Landsat-8 surface reflectance images using MODIS images." J. Appl. Remote Sens 9, 96095. DOI: 10.1117/1.JRS.9.096095.

Hazaymeh, K., and Hassan, Q.K. 2015b. "Fusion of MODIS and Landsat-8 Surface Temperature Images: A New Approach." PLoS One 10, 117755. DOI: 10.1371/journal.pone.011775.

Hills, T.C., and Reynolds, S.G. 1969. "Illustrations of soil moisture variability in selected areas and plots of different sizes." Journal of hydrology 8 (1), 27-47. DOI: 10.1016/0022-1694(69)90029-8.

Ibrahim M., Koch B., and Datta P. 2021. Evaluate the effect of land surface temperature in arid and semi-arid lands using potential remote sensing data and GIS techniques. International Journal of Global Warming. 24: 342-355.

Jaber S.M. 2021. "On the relationship between normalized difference vegetation index and land surface temperature: MODIS-based analysis in a semi-arid to the arid environment." Geocarto International. 36: 1117-1135.

Jaber S.M. 2018. "Landsat-based vegetation abundance and surface temperature for surface urban heat island studies: the tale of Greater Amman Municipality." Annals of GIS. 24: 195-208.

Kitanidis, P.K. 1997. "Introduction to Geostatistics: Application to Hydrogeology." University Press, Cambridge.

Kumar, K.; Arora, M.K.; Hariprasad, K.S. 2016. Geostatistical analysis of soil moisture distribution in a part of Solani river catchment. Appl. Water Sci., 6, 25–34.

Jin, T. T., Fu, B. J., Liu, G. H., and Wang, Z. 2011. "Hydrologic feasibility of artificial forestation in the semi-arid Loess Plateau of China." Hydrol. Earth Syst. Sci. 15(8), 2519–2530. DOI: 10.5194/hess-15-2519-2011.

Liu W. T., and Kogan, F. N. 1996. "Monitoring regional drought using the Vegetation Condition Index." International Journal of Remote Sensing 17 (14), 2761-2782, DOI: 10.1080/01431169608949106.

Mohanty, B. P., Skaggs, T. H., and Famiglietti J. S. 2000. "Analysis and mapping of field-scale soil moisture variability using high-resolution, ground-based data during the Southern Great Plains 1997 (SGP97) Hydrology Experiment." Water Resour. Res 36, 1023– 1031, doi:10.1029/1999WR900360.

Mohanty, B. P., Skaggs, T. H. 2001. "Spatial-temporal evolution and time stable characteristics of soil moisture within remote sensing footprints with varying soil, slope and vegetation. Advances in Water Resources, 24, 1051-1067.

Olea R.A. 1999. "Geostatistics for engineers and earth scientists." Boston. Springer. ISBN 978-0-7923-8523-3 pp. 303.

Parida, B. R., Collado, W. B., Borah, R., Hazarika, M. K., and Samarakoon, L. 2008. "Detecting Drought-Prone Areas of Rice Agriculture Using a MODIS-Derived Soil Moisture Index." GIScience & Remote Sensing 45(1), 109-129, DOI: 10.2747/1548-1603.45.1.109.

Qiu Y., Fu B, Wang J, and Chen L. 2001. "Soil moisture variation in relation to topography and land use in a hillslope catchment of the Loess Plateau, China." Journal of Hydrology 240, 243–263. doi:10.1016/S0022-1694(00)00362-0.

Robinson, D. A., Campbell, C. S., Hopmans, J. W., Hornbuckle, B. K., Jones, S. B., Knight, R., Ogden, F., Selker, J., and Wendroth, O. 2008. "Soil moisture measurements for ecological and hydrological watershed scale observatories: a .org/10.2136/vzj2007.0143.

Robock, A., Vinnikov, K.Y., Srinivasan, G., Entin, J.K., Hollinger, S.E., Speranskaya, N.A., Liu, S., and Namkhai, A. 2000. "The global soil moisture data bank." Bulletin of the American Meteorological Society 81, 1281–1299. DOI: 10.1175/1520-0477(2000)081<1281:TGSMDB>2.3.CO;2.

Romshoo, S. A. 2004. "Geostatistical analysis of soil moisture measurements and remotely sensed data at different spatial scales." Environmental Geology, volume 45, pages339–349.

Sandholt, I., Rasmussen, K., and Anderson, J. 2002. "A simple interpretation of the surface temperature/vegetation index space for assessment of the surface moisture status." Remote Sensing of Environment 79: 213–224. doi:10.1016/S0034-4257(01)00274-7.

Schnur, M.T., Xie, H., and Wang, X. 2010. "Estimating root zone soil moisture at distant sites using MODIS NDVI and EVI in a semi-arid region of southwestern USA".

Sun, L., and Sun, R. 2012. "Monitoring surface soil moisture status based on remotely sensed surface temperature and vegetation index information." Agric. For. Meteor 166–167, 175–187. doi: 10.1016/j.agrformet.2012.07.015.

Seneviratne, S. I., Corti, T., Davin, E. L., Hirschi, M., Jaeger, E. B., Lehner, I., Orlowsky, B., and Teuling, A. J. 2010. "Investigating soil moisture-climate interactions in a changing climate: a review." Earth-Science Reviews 99(3–4), 125–161. doi.org/10.1016/j.earscirev.2010.02.004.

Wang, X., Xie, H., Guan, H., and Zhou, X. 2007. "Different responses of MODIS-derived NDVI to root-zone soil moisture in semi-arid and humid regions." J. Hydrol. 340 (1–2), 12–24. doi.org/10.1016/j.jhydrol.2007.03.022.

Webster, R. M. 2001. "Geostatistics for environmental scientists." Chichester. John Wiley and Sons. ISBN 0471965537 pp. 271.

Weng, Q., Fu, P., and Gao, F. 2014. "Generating daily land surface temperature at Landsat resolution by fusing Landsat and MODIS data." Remote Sens. Environ 145, 55–67. doi.org/10.1016/j.rse.2014.02.003.

Western, A. W., and Blöschl, G. 1999. "On the spatial scaling of soil moisture." J. Hydrol. 217. 203– 224, doi:10.1016/S0022-1694(98)00232-7.

Xu, C, Qu, J., Hao, X., Cosh, M., Prueger, J., Zhu, Z., and Gutenberg, L. 2018. "Downscaling of Surface Soil Moisture Retrieval by Combining MODIS/Landsat and In Situ Measurements. Remote Sens 10, 210. doi.org/10.3390/rs10020210.

Zhan, Z, Qin, Q, and X. Wang, 2004. The Application of LST/NDVI Index for Monitoring Land Surface Moisture in Semiarid Area, Geoscience and Remote Sensing, 2004, IGARSS '04. Proceedings 2004 IEEE International, 3:1551–1555.

Zhang, J., and Oxley, R.R.B. 1994. "A comparison of three methods of multivariate analysis of upland grasslands in North Wales." Journal of Vegetation Science 5(1), 71–76. DOI: 10.2307/3235640.

Zhong, A., Wang, A., Li, J., Xu, T., Meng, D., Ke, Y., Li, X., and Chen, Y. 2018. "Downscaling of passive microwave soil moisture retrievals based on spectral analysis." International Journal of Remote Sensing 39(1), 50-67, DOI: 10.1080/01431161.2017.1378456.

JJEES

JJEES (2022) 13 (4): 263-270
ISSN 1995-6681

Jordan Journal of Earth and Environmental Sciences

Plastic Waste for the Enhancement of Concrete Properties - A review

Salim Kennouche*[1], Hami Brahim[1],
Houssam Eddine Abdelli[2], J.L.Barroso de Aguiar[4], Carlos Jesus[5]

[1] Department of Civil Engineering, University of Bouira, Algeria
[2] Research Unit of Emergent Materials, University Ferhat Abbas Setif 1, Algeria
[4, 5] University of Minho, C-TAC Research Centre, Guimarães, Portugal

Received 18th October 2021; Accepted 22nd April 2022

Abstract

Abstract. The consumption of different forms of plastics is interesting to the environmental protection subject. The increasing use of plastics in many areas of human daily life results in the accumulation of plastic waste in the environment. The introduction of plastic waste in concrete is a solution to preserve the environment and reduce the cost of concrete.

This paper presents an overview of some published research regarding the use of waste plastic in concrete. we present the work of many researchers on the valorization of plastic waste in concrete in different forms as a partial replacement of fine and coarse aggregate as well as fibers and their effects of waste plastic addition on the fresh, mechanical, and durability of concrete. The research work seems interesting, which shows the possibility of recycling plastic waste in concrete. However, it will be interesting to explore the combined uses of plastic as aggregate and fiber in concrete, which allows a possible recovery of additional quantities of plastic waste in concrete.

Keywords: *fiber in concrete, plastic waste, recycling, concrete properties, waste management.*

1. Introduction

Plastics have become an inseparable and integral part of our lives. The quantity of this material consumed annually has increased steadily. Its less density, user-friendly designs, manufacturing capabilities, long life, lightweight, and low costs are the factors that explain this phenomenal growth. Siddique et al (2008) have described that plastics have been used in packaging, automotive and industrial applications, medical distribution systems, other health applications, water desalination, soil conservation, flood prevention, food transport, and other uses. A large amount of plastic waste is produced each year.

We estimate that 8300 million metric tons (Mt) of virgin plastics have been produced to date. As of 2015, approximately 6300 Mt of plastic waste had been generated, around 9% of which had been recycled, 12% was incinerated, and 79% was accumulated in landfills or the natural environment. If current production and waste management trends continue, roughly 12,000 Mt of plastic waste will be in landfills or the natural environment by 2050 (Geyer et al., 2017).

Diverse usage and manufacturing of plastics in large quantities are considered the source of the environmental waste plastic problem, which the man focalized to reduce the impact of waste plastic (Singh et al., 2017). Recycling by using plastic waste in concrete in different forms is one of the solutions adopted by many searchers. Ismail and AL-Hashmi, (2008) used a plastic waste composed of about 80 % polyethylene and 20 % polystyrene with a variable length of 0.15- 12 mm and a width of 0.15 to 14 mm for different colors as a partial replacement of sand in the concrete. Rahmani et al., (2013), studied the use of plastic waste (Polyethylene terephthalate PET) as a partial substitute for fine aggregate with a maximum size of 7 mm. Usman et al (2015), used polyethylene bags in concrete to replace coarse aggregates. The workability, density, compressive and flexural strength, water permeability, static and dynamic modulus of elasticity, and abrasion resistance properties of concrete were investigated in the study of (Jain et.al, 2019) by adding different percentages (0, 0.5, 1, 2, 3 and 5%) of waste plastic bags by weight of concrete. Abu-Saleem et al., (2021), concluded that using plastic waste as a partial replacement for natural coarse aggregate up to 20% satisfies the concrete bloc design requirement and the strength loss is not detrimental. Up to 20% replacement of PET and PP showed an improved abrasion resistance compared to the control mix. PET exhibited an acceptable drying shrinkage compared to the control mix.

Rahim et al., (2013), examined the use of high-density polyethylene (HDPE) plastic waste as coarse aggregate in concrete with a size between 4.75 mm and 20 mm. Bhogayata and Arora, (2017), examined the fresh and hardened properties of concrete reinforced with metalized plastic waste (MPW) fibers (used for wafer packaging) of 5 mm, 10 mm and 20 mm with percentages from 0 to 2 by volume of the mixture.

In this paper, we study the different forms of use of plastic waste in concrete by different researchers around the world and their effect on concrete performance. Its objective is to reduce plastic waste in the environment so can be an asset to participate in sustainable development in reducing this waste.

* Corresponding author e-mail: kennouchesalim@gmail.com

2. Valorization of plastic waste as aggregates

Due to the great problems of disposal of plastic waste, it has been used in concrete by many researchers as a partial replacement for fine or coarse aggregates.

Rai et al., (2012), studied the properties of concrete mixtures with plastic waste, which replaced fine aggregate with 5 %, 10 %, and 15 % by volume. They concluded that the compressive strength of concrete decreases as the rate of waste increases. This trend could be attributed to the reduction in adhesive strength between the plastic waste surface and cement paste, as well as the increased particle size of the plastic. Ramadevi and Manju, (2012), examined the possibility of using PET bottles as a partial replacement for fine aggregate in concrete. They found that the compressive strength increased up to 2 % of (PET) fibers and gradually decreased by 4 % and 6 % of substitutions as well as tensile strength.

Saikia and Brito, (2014), evaluated the effects of the sizes and shapes of PET aggregate on the fresh and hardened characteristics. Three types of plastic waste aggregates were used in this study. One in the form of (PA) pellets replacing the fine aggregate with 5 %, 10 %, and 15 %. The other two with shredded pieces, one replacing the fine aggregate PF with 5 %, 10 %, and 15 %, and the last substituting the coarse aggregate (PA) with the same percentages. They found that the differences in size and shape of (PET) aggregates affect the slump and the abrasion resistance of concrete mixes with PET types was better than that of reference concrete. Table 1 summarizes some recent work research, that waste plastic was used as aggregate in concrete.

Table 1. Summary of some research using plastic waste as aggregate in the concrete.

Type of plastic waste	Studied %	Size of particles Studied (mm)	Optimal %	The optimal size (mm)	Reference
80% polyethylene; 20% polystyrene	0-5-15- 20	Fine (0.15–12 length; 0.15-14 width)	10	Not indicated	(Ismail and AL-Hashmi, 2008)
Polyethylene Terephthalate PET	0-5-10-15	Fine (< 7)	10	< 7	(Rahmani et al. ,2013)
High-density Polyethylene HDPE	0-10-20-30	Coarse (4.75-20)	20	Not indicated	(Rahim et al., 2013)
Plastic pallet	0-5-10-15	Fine (NI)	5	Not indicated	(Rai et al., 2012)
PET bottle	0-5-10-15	Fine (< 4; < 2) Coarse (< 16)	10	Not indicated	(Saikia and Brito, 2014)
Recycled plastic Waste	0-7.5-15	Fine (1-4) Coarse (2-11.2)	7.5	Not indicated	(Silva et al., 2013)
PET bottle	0-5-10-15-20	Fine (< 4.75) Coarse (4.75-20)	5	Not indicated	(Saxena et al., 2018)

3. The effect of replacing aggregate with plastic waste on the mechanical properties of concrete.

3.1. Properties of fresh concrete

3.1.1. Workability

Ismail and AL-Hashmi, (2008), noticed that the slump values of concrete mixtures in plastic waste tended to decrease with the increase in the rate of these wastes. This reduction might be because some particles are angular and others have non-uniform shapes. The same result was found by Rai et al., (2012).

Rahmani et al., (2013), concluded that the slump value decreased with the percentage increase in the replacement of sand by PET in both water-cement ratios of 0.42 and 0.54.

The workability of the concrete decreased when the PET content was increased. This result could be related to PET particles being more specific surfaces compared to natural sand due to their mercenary form and there would be more friction between the particles. Unlike natural, plastic aggregates do not absorb water during mixing. Shubbar and Al-Shadeedi, (2017), examined the effect of the use of PET waste as a partial replacement of fine aggregate on the mechanical properties of concrete. The results indicated that as the waste content increases, the fluidity of the concrete improves, despite the decrease in the slump value. The spherical and smooth shape of the plastic aggregate is not only the reason for this behavior but it can also be related to water not absorbed by PET waste causing some abundant water in the mixture. Usman et al., (2015), found that the workability of the mixture decreased as the polyethylene waste rate increased. But the workability can be adjusted by varying the amount of water. Hama and Hilal, (2017), concluded that the slump flow diameters of mixtures produced with coarse plastic waste were less than that produced with fine plastic waste and mixed plastic waste. Figure. 1 illustrates the results of the effect of plastic waste on a concrete slump.

3.1.2. Density

Rai et al., (2012), found that the fresh density decreased by 5 %, 8.7 %, and 10.71 % for 5 %, 10 %, and 15 % of replacement respectively. This trend could be attributed to the density of plastic waste being less than that of sand by 70 %, resulting in a reduction in the fresh density. These results were consistent with those (Ismail and AL-Hashmi, 2008).

The substitution of fine aggregate with PET waste had a measurable effect on fresh density with a downward trend resulting from the addition of plastic waste to the mixture.

The results indicated that at a PET replacement level of 1 %, 2 %, 4 % and 8 %, there was a decrease of 0.5 %, 2,8 %, 7.3 % and 9 % in the fresh density. This was due to the lighter specific gravity of the plastic aggregate, which was 13.75 % lower than the fine aggregate used (Shubbar and Al-Shadeedi, 2017). Saikia and Brito, (2014), showed that there was a reduction in the density of fresh concrete when the plastic aggregate content increased because the density of plastic aggregate particles is very low compared to natural aggregate. Silva et al., (2013), found that the wet density of concrete with plastic aggregates was significantly lower than that of control concrete, due to the lower density of plastic aggregate (PA). The loss of density was greater when progressively bigger and flakier PA was incorporated. Figure. 1 summarizes the results of the effect of plastic waste on the fresh density of concrete.

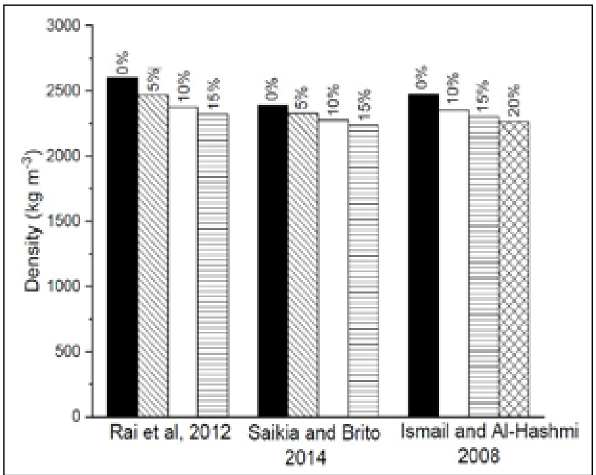

Figure 1. The effect of plastic waste on the fresh density of concrete.

3.2. Properties of hardened concrete

3.2.1. Compressive Strength

Ismail and AL-Hashmi, (2008), concluded that the compressive strength decreased with increasing plastic content for all plastic concrete mixtures at all curing ages. This could be attributed to the reduction in the adhesion strength between the plastic surface used and the cement paste. These results were consistent with those (Rai et al, 2012).

Rahmani et al., (2013), found that the replacement of 5 % of sand by PET gave the optimum strength for both mixtures and with an increase in the PET content, the resistance decreased. The results indicated that as sample sizes increase, the compressive strength decrease. Shubban and Al-Shadeedi, (2017), observed a slight increase in the compressive strength in the percentage of 1 % by 3.7 % and 1.6 % during the 7 and 28 days of hardening. But an obvious increase was observed by adding 2 % of PET waste approximated by 15 % and 13 %, respectively at 7 and 28 days. Followed by a drop to about 25 % for 8 % of replacement at both curing periods. The compressive strength of the cube increased with increasing PET waste et it gives a maximum value of 2 % PET.

Mustafa et al., (2019), found that the compressive strength of the plastic concrete decreased with the increase in plastic content. As the sand was replaced by plastic waste, the average compressive stress was reduced by 24 % with 20 % of volume replacement.

Rahim et al., (2013), concluded that the compressive strength of concrete containing aggregate (HDPE) is less retained compared to the control samples. However, the resistance decreased significantly when the proportion of HDPE was greater than 20 %. The decrease in strength might be attributed to the lower bond between the cement paste and PHD aggregate and the lower strength of the plastic.

The maximum strength obtained with 10 % replacement of bottle caps increased by 9.72 % and 5.97 % at 7 and 28 days compared to the reference concrete. (Saxena et al., (2018), concluded that the incorporation of PET plastic waste as coarse aggregate in concrete results in a decrease in compressive strength due to a poor bond between the plastic waste and the mortar paste. Figure. 2 shows the results of the compressive strength of concrete with the percentage of waste plastic replacement.

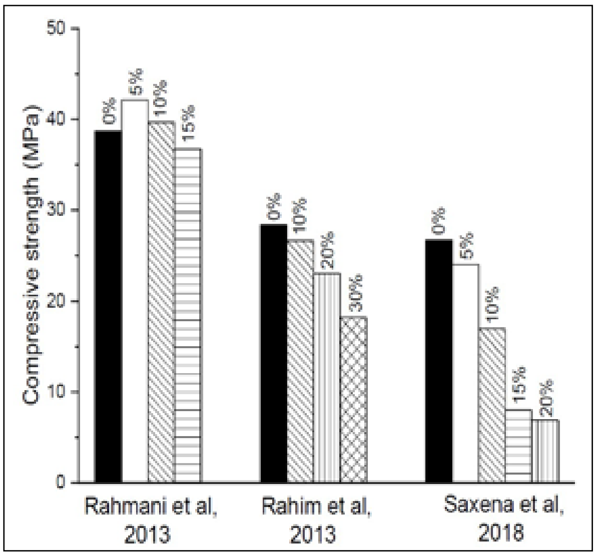

Figure 2. Compressive strength with % of waste plastic replacement at 28 days.

3.2.2. Tensile Strength

For the tensile strength, (Rahmani et al. 2013), showed a decrease in the tensile strength with increasing PET up to 15 % for the two water-cement ratios of 0.42 and 0.54. Shubbar and Al-Shadeedi, (2017), observed an increase in tensile strength by splitting with the increase in substitution of fine aggregate with PET bottles waste up to 2 % at 7 and 28 days of curing. After that, there was a decrease to obtain a minimum value of 8 % replacement. The decrease in strength could be due to the aggregate density and adhesive strength between the aggregate and the cement. Albano et al., (2009), studied the replacement of sand by PET with a grain size of 0.26 and 1.14 cm in concrete with the variation in the water-cement ratio (0.50 and 0.60).

They found that for a water-cement ratio of 0.50, there was a decrease in the tensile strength by splitting compared to the reference concrete regardless of the size of the PET added. However, when the amount of recycled PET was 20 %, the decrease was more significant because of the high porosity of the concrete may have with this amount of PET. When the water-cement ratio is equal to 0.60, the trends observed remain the same. Again, the tensile strength values decreased compared to the control mixture, but in higher amounts.

They showed that the tensile strength increased when the fine aggregate was partially replaced by 6 % of plastic. However, replacing more than 6 % decreased resistance.

3.2.3. Flexural strength

For flexural strength, (Ismail and AL-Hashmi, 2008), found that the flexural strength of plastic concrete mixes decreased with increasing plastic rates. These results were consistent with (Rai et al., 2012). Ramadevi and Manju, (2012), concluded that the flexural strength of the specimens with the replacement of the fine aggregate with PET bottle fibers gradually increased with the increase in the percentage substitution.

Shyam and Drishya, (2018), studied the replacement of fine aggregate by high-density polyethylene powder (HDPE) at percentages of 5 %, 10 %, 15 %, and 20 %. They concluded that the optimal value was obtained with a 5 % replacement of the fine aggregate by HDPE powder. The flexural strength increased to 46.34 % for 5 % of replacement and was significantly higher than that of the control samples and all other percentages of substitution. Rahmani et al, (2013), concluded that the maximum value of flexural strength is found at 10 % replacement of coarse aggregates by plastic waste.

3.2.4. Water absorption and durability

Albano et al., (2009) found that for a water-cement ratio of 0.50, the absorption percentage for mixtures with 10 % was lower than those with 20 % because to lower porosity. Also, the mixtures with PET of large particle size have higher values of water absorption. For a water-cement ratio of 0.60, trends in particle content and size were similar to those obtained for a water-cement ratio equal to 0.50. Moreover, it can be seen that for the higher water-cement ratio, the less the surface area covered by the aggregate was reduced, so reducing the amount of paste, voids, or pores in the concrete also increased the water absorption.

Saikia and Brito, (2014) concluded that the abrasion resistance of concrete mixes containing various types of PET aggregate was better than that of the control concrete. The abrasion resistance of concrete with the incorporation of various types and contents of PET-aggregates can be related to its compressive strength.

Nikbin et al., (2016) studied the feasibility of using waste polyethylene terephthalate (PET) particles to replace aggregates for acid erosion of normal and durable lightweight structural concrete. They concluded that the ultrasonic wave velocity decreased in the specimens containing more percentages of PET particles. It might be due to the higher capacity of concrete containing PET particles to resist the internal pressure caused by the expansion of cement paste and retain more integrity during the reaction to sulfuric acid, which could be related to its more porosity as accommodation for reaction products and the flexibility of PET particles.

Saxena et al., (2018) found that the addition of PET plastic waste improves the ductile behavior of the concrete and the energy absorption capacity of the plastic concrete increase with the waste plastic aggregate content in the concrete. Silva et al., (2013) concluded that the water absorption increased when replacing natural aggregates with plastic aggregates. Concrete with plastic aggregates showed higher carbonation depths and chloride migration coefficients than control concrete.

4. The effect of the use of plastic waste in the form of fibers on the concrete

4.1. Valorization of plastic waste as fiber in concrete

Concrete is characterized by several facts such as low tensile strength, low ductility, heavyweight, and low energy absorption. These disadvantages have led civil engineers to use conventional reinforcement to increase tensile strength and ductility. The notion of using fibers as reinforcement is not new.

Pesic et al., (2016) studied the mechanical properties of concrete reinforced with recycled high-density polyethylene extruded plastic fibers (PHDE). Two fiber diameters of 0.25 (AR = 92) mm and 0.40 mm (AR = 75) with three-volume fractions of 0.40 %, 0.75 % and 1.25 % were used in this study. They concluded that the introduction of PHDE fiber does not influence the modulus of elasticity and the compressive strength of concrete.

Marthong and Sarma, (2015) examined the influence of different PET fiber geometries on the physical and mechanical properties of concrete. The test results showed that the geometry of the fiber has a marginal effect on the workability of concrete. However, it plays an important role in achieving good compressive and tensile strength of concrete. Table 2 summarizes some recent work research, that waste plastic was used as fiber in concrete.

Table 2. Summary of some research on the use of plastic waste as a fiber in concrete.

Type of plastic fiber	Studied %	Size of fiber studied (mm)	Optimal %	The optimal size (mm)	Reference
PET bottle	0-0.6-0.8-1-1.2	AR= 30-50-70	1	50	(Singh et al., 2017)
Metalized plastic Waste	0-0.5-1-2	AR= 5-10-20	1	20	(Bhogoyata and Arora ., 2017)
High-density Polyethylene	0-0.4-0.75-1.25	Θ = 0.25;0.40 1.25	1.25	Not indicated	(Pesic et al., 2016)
PET bottle	0-0.5-1-1.5	AR= 1.33-1.67-2	0.5	1.33	(Shamskia et al., 2012)
PET water bottle	0-0.5-1	AR= 0.5-1-1.5	0.5	Not indicated	(Taherkhani et al., 2014)
Polyethylene LDPE	0-0.25-0.5-0.75-1-1.25	AR= 10	0.5	Not indicated	(Mohammad- hosseini et al., 2018)

4.2. Properties of fresh concrete

(Pelisser et al., (2012) showed that a greater loss of slump occurred as the fiber content increased. The concrete reinforced by PET fiber still has good workability and was easily compacted without excessive vibration. Bhogayata and Arora, (2017) found that the workability of the concrete was affected by the two test parameters, namely the fraction and type of MPW fibers. Concrete containing fibers of type A (5 mm) showed a reduction in the slump of 5 %, 8 %, 12 %, and 16 % to vary the fraction from 0.5 % to 2 %. Concrete with fibers of type B (10 mm) and type C (20 mm) reduced the slump relatively more than the first type. They concluded that a higher dosage of MPW fibers increases the viscosity of the matrix and decreases the consistency of the fresh mixture at a higher volume fraction. Marthong and Sarma, (2015) concluded that for the water-cement ratio of 0.50, the workability of concrete was slightly decreased with the inclusion of 0.5 % PET fibers. However, the geometry of the fiber had a small significant effect on the workability of the concrete. Shamskia, (2012) examined the influence of PET fiber on the fresh and hardened properties of the concrete. The results showed that by increasing the percentage of fibers, the workability decreased significantly. Thus, to produce a feasible mixture, a superplasticizer was used.

Singh et al., (2017) used various types of PET fiber in concrete to improve its performance at percentages of 0.8 %, 1 %, and 1.2 % by weight of cement. They concluded that the workability of the concrete mix decreases with the incorporation of PET fibers for all aspect ratios. Concretes containing straight PET fibers had higher workability than concretes containing folded PET fibers.

4.3. Properties of hardened concrete

Marthong and Sarma, (2015) found that the addition of 0.5 % PET fiber in the concrete improves the compressive strength of the samples and varied with the fiber geometry. On the other hand, many researchers found that the compressive strength was not affected by plastic fibers (Pesic et al., 2016; Bhogoyata and Arora, 2017).

Borg et al., (2016) studied the performance of concrete reinforced by fibers produced from plastic waste, and polyethylene terephthalate (PET). Different types of shredded, straight, and deformed recycled PET fibers, as well as different lengths of 30 mm and 50 mm, were evaluated for a percentage of addition ranging from 0.5 % to 1 % in the concrete. They concluded that the addition of recycled PET fibers leads to a reduction in compressive strength of 0.5 % to 8.5 % compared to the control mixture.

Taherkhani, (2014) studied the use of PET waste as fiber in concrete with different lengths of 1, 2, and 3 cm at percentages from 0.5 to 1 % by volume of the mixture. They concluded that the compressive strength at 7 and 28 days decreased with increasing length and fiber content, with the lowest resistance for the mixture containing 1 % PET of 3 cm. This reduction was attributed to a lack of adequate bonding between the fibers and the cement paste, and more potential for crack development.

Kumar and Daule, (2017) concluded that the compressive strength increases with the increase in fiber content and the maximum value at the percentage of 1.5 %. (Mohammad hosseini et al., 2018) concluded that the incorporation of metallized plastic waste (MPW) in percentages of 0.25 %, 0.5 %, 0.75 %, 1 % and 1.25 % decrease the strength by 6 %, 7 %, 11 %, 18 % and 21 %, respectively. This decrease could be attributed to the existence of air voids in the matrix that are increased by the addition of fibers in the concrete. Figure. 3 presents the results of compressive strength as a percentage of waste plastic fibers.

For the tensile strength, (Marthong and Sarma, 2015) demonstrated that the inclusion of 0.5 % PET fiber enhances the resistance. On the other hand, (Taherkhani, 2014) concluded that the tensile strength of the mixture reinforced by fibers was lower than that of the reference mixture. The resistance increased with increasing fiber length, while at higher levels it decreased with the increase of the fiber length. (Pelisser et al., 2012) found that the tensile strength increases with increasing fiber content, despite the effect diminished at 150 days. Singh et al., (2017), concluded that the resistance of mixtures with PET fibers increases up to 1 % for all aspect ratios and concrete with crimped fibers had a high value than concrete with straight fibers. Khalid et al., (2018) investigated the effect of incorporating waste PET bottles as fibers on the performance of concrete. They concluded that the tensile strength increased by 16.9 %, 26.3 % and 13.3 % at 0.5 %, 1 % and 1.5 % of fiber content respectively, in RPET-5 type (60 mm diameter and 5 mm thickness).

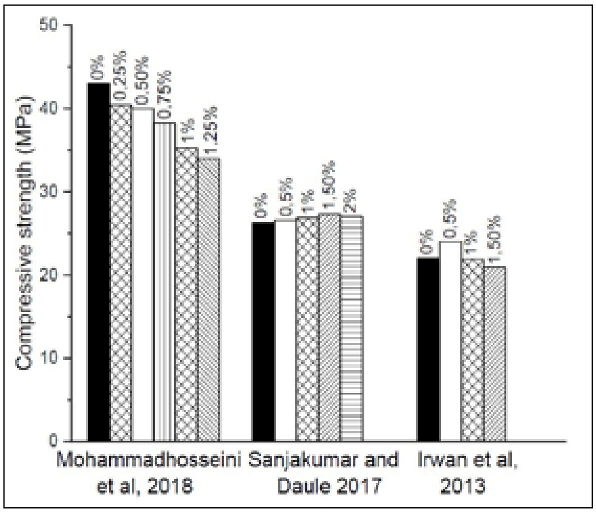

Figure 3. Compressive strength with different waste plastic fibers at 28 days.

Bui et al., (2018) concluded that recycled PET bottle waste (RPET) and recycled woven plastic sack waste (RWS) improve the tensile strength of recycled aggregate concrete (RAC). The tensile strength of RAC reinforced with RPET fibers increased from 11.8 to 20.3 %, while RWS fibers only improved strength by 9 to 16.6 %. Figure. 4 shows the results of the effect of plastic waste fibers on the tensile strength of concrete.

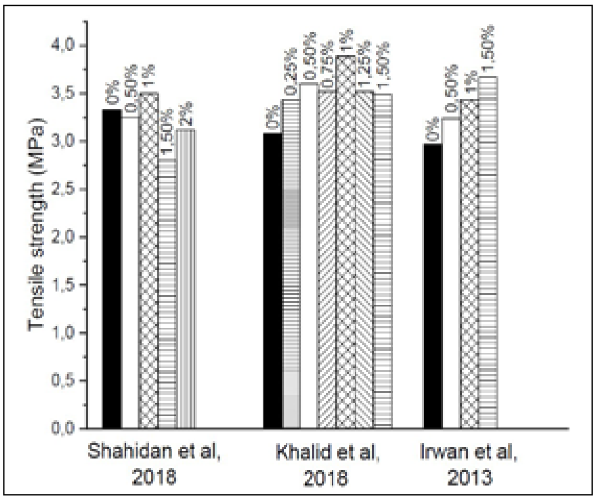

Figure 4. Effect of plastic waste fibers on the tensile strength of concrete.

For the flexural strength, (Taher Khani., 2014) concluded that the flexural strength of the mixtures increases with increasing fiber length. He also found that the strength of the blends decreases with the increase in fiber content. This was attributed to staying more water in the mix with a higher fiber rate, which leads to weak concrete. In addition, the smooth surface of the fibers causes a reduction in the bond between the fiber and the cement paste.

Mohammad hosseini et al., (2018) observed an increase in flexural strength in concrete mixes containing metalized plastic waste compared to control concrete at 7, 28, and 90 days of curing. In contrast, the researchers found that the flexural strength was not directly affected by the inclusion of PET fiber in concrete, (Bhogoyata and Arora, 2017).

4.4. Durability

Taherkhani, (2014) found that the mixture containing PET fiber was more abrasion resistant than the control mix. Abrasion resistance increased with increasing fiber lengths. On the other hand, mixtures containing short fiber had a lower modulus of elasticity than the control mixture. Marthong, (2015) found that the PET fibers increase both the ductility and energy absorption of axially compressed concrete samples. The results showed that the inclusion of PET fibers in concrete has improved the crack resistance of conventional concrete. The presence of MPW fibers has extended the ductility of the cement paste against brittle failure and reduced the spread of microcracks in the cured mass. Besides, MPW fiber improved the deformation capacity at higher loads subjected to axial compression, (Bhogoyata and Arora, 2017). Pesic et al., (2016) found that the HDPE fibers reduced the water permeability of concrete by a significant magnitude of 17- 42 % when the depth of water penetration was measured. This proved that HDPE will be more sustainable in the exploitation than ordinary concrete.

Even a small amount of added PHDE fibers showed a significant reduction in the cracking of concrete. The reduction of crack widths by more than 50 % was achieved with a volume of 0.40- 1.25 % of HDPE fibers. The mixture of 0.5 % PET fiber in the concrete showed no signs of a porous structure. Since a predicted range of UPV values (3.5 km/s to 4.5 km/s) has been obtained (Marthong and Sarma, 2015). Krishnammorthy et al., (2017) studied the durability of concrete with PET fibers. Three volume fraction 0.5 %, 1 % and 1.5 % used with three aspect ratios 0.15- 0.30 and 0.45. They concluded that the mixture with PET fiber with a volume fraction of 1 % and an aspect ratio of 0.45 gives better results in acid and chloride attacks. Kim et al., (2010) examined the properties of concrete with the incorporation of recycled PET fibers. They found that cracking due to drying shrinkage was delayed in samples of reinforced concrete with PET fibers compared to unreinforced samples.

After the concrete samples have been immersed in the magnesium chloride solution for 30, 60, and 90 days, (Vijaya et al., 2018) observed that the percentage reduction in weight loss decreased as the percentage of fiber content increased and the chloride penetration was reduced with an increasing percentage of fiber content.

Bui et al., (2018) found that the recycled woven plastic sack waste (RWS) and recycled PET bottles waste fiber (RPET) enhanced the shear strength of recycled aggregate concrete (RAC) by about 2–4 % and 7–15 %, respectively. Both RWS and RPET fibers improved the post-cracking behavior and ductility capacity of RAC. Kim et al., (2010) concluded that the concrete mixes with recycled PET fibers had relative ductility indices about 7 to 10 times higher than fiber-free mixes. Beyond a volume fraction of about 0.5 %, the ductility index and energy capacity decreased as the volume fraction of the fibers increased. Hosseini and Tahir, (2018) examined the durability performance of concrete containing metalized plastic fibers (MPW). They found that the penetration depth in the OPC mix with 0.5 % MPW fibers was 14.8 mm, 24 % less than the 19.5 mm obtained in the control mix.

Bhogayata and Arora, (2018) concluded that the acid and sulphate resistance, corrosion resistance, and resistance to oxygen permeability of conventional concrete were improved due to the presence of short MPW fibers. The type A fibers (5 mm long and 1 mm wide) filled the pore spaces around the aggregate-hydrated cement paste transition zone due to better adhesion of the constituents and helped to reduce voids within the hardened mass.

5. Conclusions

The results of the various researchers indicated:

- The addition of plastic as a substitute for aggregate increases tensile and flexural strengths compared to the reference concrete.
- Water absorption decreases in mixtures containing plastic as an aggregate because plastic waste has a lower water absorption capacity than the natural aggregate, an important positive parameter to produce durable concrete.
- The abrasion resistance of concrete mixes containing various types of PET aggregate is better than that of the control concrete due to the incorporation of fiber.

- The addition of PET plastic waste improves the ductile behavior of the concrete and the energy absorption capacity of the plastic concrete increase with the waste plastic aggregate content in the concrete.
- The incorporation of plastic aggregate in concrete show higher carbonation depths and chloride migration coefficients than control concrete, explained by the law of porosity of concrete.
- The chloride penetration was reduced with an increasing percentage of fiber content in the concrete, due to the impervious plastic particles which block the passage of the chloride ion.
- The plastic waste fiber enhanced the shear strength, post-cracking behavior, and ductility capacity of recycled aggregate concrete, due to the reinforcing role of fiber.

Abbreviations and definitions

LDPE : Low- Density Polyethylene
PS : Polystyrene
PET : Polyethylene Terephthalate
HDPE : High-density polyethylene
MPW : Metallized Plastic Waste
PET : Polyethylene Terephthalate
PC : Plastique aggregate
PHD : Polyethylene High-Density
UPV : Ultrasonic Pulse Velocity
RWS : plastic sack waste
RPET : Recycled Polyethylene Terephthalate
RAC : Recycled Aggregate Concrete
OPC : Ordinary Portland Cement
AR : Aspect Ratio

References

Abu-Saleem, M., Zhuge, Y., Hassanli, R., Ellis, M., Rahman, M., & Levett, P. (2021). Evaluation of concrete performance with different types of recycled plastic waste for kerb application. Construction and Building Materials, 293, 123477.

Albano, C., Camacho, N., Hernández, M., Matheus, A. and Gutiérrez, A. (2009) "Influence of content and particle size of waste pet bottles on concrete behavior at different w/c ratios", Waste Management 29(10), 2707–2716.

Bhogayata, A. C., & Arora, N. K (2017), "Fresh and strength properties of concrete reinforced with metalized plastic waste fibers", Construction and Building Materials, 146, 455-463.

Bhogayata, A.C. and Arora, N.K. (2018) "Impact strength, permeability and chemical resistance of concrete reinforced with metalized plastic waste fibers", Construction and Building Materials. 161, 254–266.

Borg, R.P., Baldacchino, O. and Ferrara, L. (2016) "Early age performance and mechanical characteristics of recycled PET fiber reinforced concrete", Construction and Building Materials. 108, 29–47.

Bui NK, Satomi T and Takahashi H (2018) "Recycling woven plastic sack waste and PET bottle waste as fiber in recycled aggregate concrete: An experimental study", Waste Management, 78, 79–93.

Geyer, R., Jambeck, J. R., & Law, K. L. (2017). "Production, use, and fate of all plastics ever made". Science advances, 3(7), e1700782.

Hama SM and Hilal NN (2017) "Fresh properties of self-compacting concrete with plastic waste as partial replacement of sand", International Journal of Sustainable Built and Environment, 6, 299–308.

Ismail, Z.Z., AL-Hashmi, E.A. (2008) "Use of waste plastic in concrete mixture as an aggregate replacement", Waste Management, 28, 2041–2047.

Jain, A., Siddique, S., Gupta, T., Jain, S., Sharma, R. K., & Chaudhary, S. (2019). "Fresh, strength, durability and microstructural properties of shredded waste plastic concrete". Iranian Journal of Science and Technology, Transactions of Civil Engineering, 43(1), 455-465.

Khalid, F.S., Irwan, J.M., Ibrahim, M.H.W., Othman, N. and Shahidan, S. (2018) "Performance of plastic wastes in fiber-reinforced concrete beams", Construction and Building Materials, 183, 451–64.

Kim, S.B., Yi, N.H., Kim, H.Y., Kim, J.H.J. and Song, Y.C. (2010) "Material and structural performance evaluation of recycled PET fiber reinforced concrete", Cement and Concrete Composite, 32(3), 232–240.

Krishnamoorthy, M., Tensing, D., Sivaraja, M., & Krishnaraja, A. R. (2017). "Durability studies on polyethylene terephthalate (PET) fiber reinforced concrete". International Journal of Civil Engineering and Technology, 8(10), 634-640.

Kumar, S., & Czekanski, A. (2017). "Development of filaments using selective laser sintering waste powder". Journal of Cleaner Production, 165, 1188-1196.

Marthong, C. (2015), "Effects of PET fiber arrangement and dimensions on mechanical properties of concrete", The IES Journal Part A: Civil & Structural Engineering, 8(2), 111-120,

Marthong, C. and Sarma, D.K. (2015) "Mechanical behavior of recycled PET fiber reinforced concrete matrix", International Scholarly and Scientific Research and Innovation 9(5), 879–883.

Mohammad Hosseini, H., Tahir, M.M. and Sam, A.R.M. (2018) "The feasibility of improving impact resistance and strength properties of sustainable concrete composites by adding waste metalized plastic fibers", Construction and Building Materials, 169: 223–236.

Mohammad Hosseini, H. and Tahir, M.M. (2018) "Durability performance of concrete incorporating waste metalized plastic fibers and palm oil fuel ash", Construction and Building Materials, 180, 92–102.

Mustafa, M.A.T., Hanafi, I., Mahmoud, R. and Tayeh, B.A. (2019) "Effect of partial replacement of sand by plastic waste on impact resistance of concrete: Experiment and simulation", Structures 20, 519–526.

Nikbin, I.M., Saman Rahimi R, Allahyari H and Fallah F (2016) "Feasibility study of waste Poly Ethylene Terephthalate (PET) particles as an aggregate replacement for acid erosion of sustainable structural normal and lightweight concrete", Journal of Cleaner Production 126, 108–117.

Pelisser, F., Montedo, O.R.K., Gleize, P.J.P. and Roman, H.R. (2012) "Mechanical properties of recycled PET fibers in concrete", Materials Research 15(4), 679–686.

Pesi,c N., Zivanovic, S., Garcia, R. and Papastergiou, P. (2016) "Mechanical properties of concrete reinforced with recycled HDPE plastic fibers", Construction and Building Materials, 115, 362–370.

Usman, M., Javaid, A. and Panchal, S. (2015) "Feasibility of waste polythene bags in concrete", International Journal of Engineering Trends and Technology, 23(6), 317–319.

Rahim, N.L., Salehuddin, S., Ibrahim, N. M., Amat, R.C. and Jalil, M.F. (2013) "Use of plastic waste (high-density polyethylene) in concrete mixture as an aggregate replacement", Advanced Materials Research, 701, 265–269.

Rahmani, E., Dehestani, M., Beygi, M.H.A., Allahyari, H. and Nikbin, I.M. (2013) “On the mechanical properties of concrete containing waste PET particles”, Construction and Building Materials, 47,1 302–1308.

Rai, B., Rushad, S.T., Kr, B., Duggal, S.K. (2012) “Study of waste plastic mix concrete with plasticizer”, International Scholarly Research Network Civil Engineering 2012:1–5.

Ramadevi, K., & Manju, R. (2012), “Experimental investigation on the properties of concrete with plastic PET (bottle) fibers as fine aggregates”, International journal of emerging technology and advanced engineering, 2(6), 42-46.

Saikia, N. and De Brito, J. (2014) “Mechanical properties and abrasion behavior of concrete containing shredded PET bottle waste as a partial substitution of natural aggregate”, Construction and Building Materials, 52, 236–244.

Shamskia, N. (2012) “The influence of pet fibers on the properties of fresh and hardened concret”, Journal of Structural Engineering and Geotechnics,2 (1), 13-17.

Saxena, R., Siddique, S., Gupta, T., Sharma, R.K. and Chaudhary, S. (2018) “Impact resistance and energy absorption capacity of concrete containing plastic waste”, Construction and Building Materials, 176, 415–421.

Shubbar, S. D., & Al-Shadeedi, A. S. (2017), “Utilization of waste plastic bottles as fine aggregate in concrete”, Kufa Journal of Engineering, 8(2).

Singh, N., Hui, D., Singh, R., Ahuja, I. P. S., Feo, L., & Fraternali, F (2017), “Recycling of plastic solid waste: A state of the art review and future applications”, Composites Part B: Engineering, 115, 409-422,

Siddique, R., Khatib, J., and Kaur, I, (2008) “Use of recycled plastic in concrete: A review”, Waste Management 28, 1835–1852.

Silva, R. V., De Brito, J. and Saikia, N. (2013) “Influence of curing conditions on the durability-related performance of concrete made with selected plastic waste aggregates”, Cement and Concrete Composites 35, 23–31.

Taherkhani, H. (2014). “An investigation on the properties of the concrete containing waste PET fibers”. International Journal of Science and Engineering Investigations, 3(27), 37-43.

Vijaya, G.S., Ghorpade, V.G., and Sudarsana, R.H. (2018) “The behavior of self-compacting concrete with waste plastic fibers when subjected to chloride attack”, Materials Today Proceedings, 5, 1501–1508.

JJEES

JJEES (2022) 13 (4): 271-277
ISSN 1995-6681

Jordan Journal of Earth and Environmental Sciences

Groundwater Quality Around Active and Non-Active Dumpsites in Benin City, Nigeria

Okwuchukwu Chiedozie[1] and Akiri-Obaroakpo Tosan[1]

1University of Benin, Benin City, Edo State, Nigeria

Received 20th August 2021; Accepted 23rd April 2022

Abstract

Groundwater is a source of water for different processes in the environment. The quality of groundwater is a factor that affects many aspects of the plant, animal, human and environmental health. This study is aimed at determining and comparing the quality of groundwater water collected from an active and a non-active dumpsite. Water samples were prepared and analyzed using standard methods. The physicochemical properties, microbiological composition, and heavy metal content of the samples were determined. Results obtained were subjected to statistical analyses using Microsoft Excel 2017 and SPSS Version 21. The results showed that the pH values of samples which ranged from 4.1 - 6.6 do not fall within WHO permissible limits for human consumption. The values of other parameters had ranges as follows: electrical conductivity (10 - 370µS/cm), chloride (7.1 - 56.90mg/L), dissolved oxygen (2.2 - 5.0mg/L), biochemical oxygen demand (0.9 - 2.30mg/L), turbidity (0 - 15.0mg/L), total hardness (8 - 75.0mg/L), total dissolved solids (5.3 - 197.0mg/L) and nitrate (0.31 - 3.12mg/L) all fall within WHO limits. The results of the heavy metal analysis showed that Pb concentration from LC (after 2mins) is above the EPA limits. The highest values for heterotrophic plate count was observed for LB (44cfu/ml) (after 2mins) and LB (3.50cfu/ml) for coliform bacteria. These results also are within the WHO permissible limits for safe drinking water. It can be concluded that the quality of the groundwater in the areas of interest is within safe limits for human consumption although it can be improved through the treatment of water.

Keywords: *Groundwater pollution, water quality, dumping, Benin city.*

1. Introduction

The World Health Organization (WHO) recommends a minimum daily per capita water consumption of 27 liters/person/day. However, a large percentage of the world's population especially in developing countries manages far less than 27 liters as approximately 70% of the renewable water resources are unavailable for human use or are under-developed or unevenly distributed (Minh *et al*., 2011). Drought, desertification, and other phenomena that contribute to water scarcity are estimated to affect as many as one-third of the world's population (Talafre and Knabe, 2009). The increasing human population and rising demand for food and other services have increased the demand for water (Rodak *et al*, 2011). As a result, reliance on groundwater resources has increased, creating challenges, among which is the provision of adequate quantities of good-quality water (WWDR, 2011). It is not clear how much water is available per capita in Benin City; however, many residents manage far less than 27 liters a day. Benin City had a population of 49,143 in 1950 and it has grown to an estimated 1,781,999 in 2021 with a 3.17% annual change (Akpoveta *et al.,* 2011).

Groundwater is easily the most important component of the hydrological cycle and constitutes about two-thirds of the freshwater resources of the world including Nigeria. Groundwater provides a reasonably constant supply for domestic use, livestock, and irrigation, which is not likely to dry up under natural conditions (Calow *et al*., 2011). In arid and semi-arid areas where rainfall is scarce or highly seasonal and surface water is extremely limited, groundwater is a means of coping with water deficiencies (David, 2011). Due to the financial benefits arising from borehole development projects, numerous non-environmental and non-hydrogeological experts are into borehole and hand-dug well development. Some of these projects are sited close to waste dump sites, pit toilets, soak-away pits, and septic tanks.

Contamination of groundwater is an issue of serious environmental concern (Silderberge, 2003; Akpoveta *et al*., 2011) because groundwater is vulnerable to pollution due to the water table being near the soil surface, the permeability of overlying layers and sources of pollution being numerous (Singh *et al.,* 2012). Contamination of groundwater may be due to the leaching of pollutants (Bekhit *et al.,* 2009), contaminant transport in the soil (Andricevic *et al.,* 2011) and human activities such as indiscriminate waste disposal, poor agricultural practices and construction of septic tanks, pit latrines and graves near boreholes, contribute to borehole water contamination (Lu, 2004; Kelly *et al*., 2011). Some of these activities account for the presence of coliform bacteria in groundwater which makes it unsuitable for domestic use as a resource due to contamination (Holmes, 2007). Contamination of groundwater water by microorganisms occurs because of their ability to survive in the short travel time from the pollution site to the groundwater source (Enyinna and Nkemdirim, 2018). Other contaminants of groundwater include heavy metals, agrochemicals, nutrients, colloids, organic matter, etc. (Hillel and Rabideau, 2000;

* Corresponding author e-mail: mercy.akiri-obaroakpo@uniben.edu

Adekunle *et al.,* 2007)

The consumption of contaminated water poses the risk of water-borne diseases as evidenced by rampant water-borne diseases such as typhoid and diarrhea. These diseases are further worsened by the lack of access to basic water treatment methods and the ignorance of users to hazards associated with the consumption of these waters. For these reasons, the provision of good quality L4.2 is a necessity.

This study aimed to comparatively assess the quality of groundwater around active and non-active dumpsites around Benin City.

2. Materials and Methods

2.1 Study Area

The study was carried out in Benin City, the capital of Edo state in the humid tropical rainforest belt of southern Nigeria. Benin City is underlain by the Benin Formation which is of the Oligocene-Pleistocene type, characterized by a reddish top layer composed of ferruginized or literalized clay sand and subsequent layers made of sands, sandy clays, and ferriginized sandstone (Ikhile, 2016).

Figure 1. A map of the study area showing the sampling locations.

2.2 Sample Collection

Three (3) samples of groundwater were collected from boreholes of three residences in two major locations; one each around an active (Iguasa) and a non-active dumpsite (Ikpoba). The samples collected from Iguasa were designated LA, LB, and LC, while those from Ikpoba were designated LD, LE, and LF. Locations LA and LB, and LD and LE were 10 meters away from their respective dumpsites; however, LC and LF were 40 meters away from the respective dumpsites and serve as control samples. The boreholes were of the shallow well type and their depths ranged between 140 and 180 feet. The samples were an initial sample, then another taken after two minutes to know if there would be a change in concentration of contaminants during the analysis, and a control sample. The samples were collected using water sampling bottles after which they were kept at 4°C and taken to the laboratory for analysis.

2.3 Physicochemical Analyses

The physicochemical parameters of the groundwater samples were determined as described. The pH was determined using a pH meter. Conductivity was determined using a conductivity meter. Turbidity was determined using a nephelometer. Total total dissolved solids (TDS) were determined using the weight difference method. Alkalinity was determined by acid-base titration with H_2SO_4 using phenolphthalein as an indicator. The concentrations of nitrate and ammonia in the samples were determined by analysis using ultraviolet-visible spectrometry. Total hardness was determined by titration with EDTA using Eriochrome Black-T as an indicator. The concentration of chlorides was determined using a spectrofluorometer. The dissolved oxygen levels of the samples were determined using BOD bottles and titration with sodium thiosulphate. Biochemical oxygen demand was determined by the 5-day BOD test using Winkler A and B solutions. All physicochemical analyses were done in triplicates and the mean results were recorded.

2.4 Heavy Metal Analyses

Heavy metal analysis was carried out after the method used by Oko *et al.* (2017). Three (3) liters of each water sample were first concentrated in a sandy oven at 80°C until the volume reached 50ml. 4ml of concentrated sulfuric acid (Merck, 98%) was added to each sample which was then digested using the digesdahl apparatus for 3 minutes. After that, 10ml of hydrogen peroxide (Merck, 30%) was added and the mixture was heated until oxidation was completed. After cooling, each sample was filtered using Whatman No. 44 filter paper. The filtrate was diluted to a final volume of 50ml using deionized water. The prepared samples were analyzed using a flame atomic absorption spectrophotometer (FAAS) to determine the concentrations of heavy metals. The detection limit of the FAAS instrument was 0.01mg/L. The heavy metal analyses were all carried out in triplicates to ensure the quality of the results. The means of values obtained were recorded in mg/L.

2.5 Microbiological Analysis

Microbiological analysis of water samples was carried out to determine the heterotrophic plate count and the coliform counts for all samples. The heterotrophic plate count was done using the spread plate method and the coliform count was done using the membrane filter count method. All results were expressed as colony-forming units per milliliter of water (cfu/ml). All isolated microorganisms were subcultured onto nutrient agar made for purification. They were then transferred onto nutrient agar slants for storage and further analysis, after which they were identified using Bergey's Manual of Systematic Determinative Bacteriology (Buchanan and Gibbons, 1974).

2.6 Statistical Analysis

The mean and standard deviations of all values were calculated using Microsoft Excel 2017. Analysis of variance (ANOVA), correlation analysis, and t-tests waswere carried out using the Statistical Package for the Social Sciences (SPSS) Version 21.

3. Results and Discussion

3.1 Physicochemical analysis of water

The results of the physicochemical analysis of the water samples are were displayed in figures 2 to 12. The pH values of the samples ranged from 4.1 (LE) to 6.6 (LA). Electrical conductivity values ranged from 10µS/cm (LB) to 370µS/cm (LE). The turbidity values ranged from 0mg/L (LB, LC and LD) to 15mg/L (LA). The TDS values ranged from 5.3mg/L (LB) to 196.13mg/L (LE). Values for alkalinity ranged from 0mg/L (LD, LE, and LF) to 126mg/L (LA). The range for nitrate concentrations was 0.31mg/L (LA) to 3.10mg/L (LD). The concentrations of ammonia ranged from 0.09mg/L () to 0.85mg/L (LD and LF). Total hardness ranged from 8mg/L (LB) to 72mg/L (LE). Concentrations of chlorides ranged from 7.1mg/L (LC) to 56.5mg/L (LD and LE). The concentration of dissolved oxygen was highest in LB at 5.0mg/L and lowest in LA at 2.2mg/L. The biochemical oxygen demand was highest in LE at 2.3mg/L and lowest in LA at 0.9mg/L.

The pH values from the active dumpsite range from 5.3 - 6.6 and those from the non-active dumpsite range from 4.1 - 4.4. From these results, the values are not within the World Health Organization's acceptable pH range (6.5 - 8.5) for water quality (WHO, 2006). Organic waste such as food waste, green waste, and pruning waste was found in the assessed dumpsites. The low pH values recorded from the water samples are attributed to the early acidogenic phase of organic waste decomposition as described by Wdowczyk and Szymanska-Pulikowska (2020). The electrical conductivity of all collected water samples falls within the limits (1300mS/cm) set by the World Health Organization (WHO, 2006). The total dissolved solids values of all groundwater samples fall within the limits (500mg/L) set by the World Health Organization (WHO, 2006). The turbidity of groundwater samples collected from LA is above WHO standards (WHO, 2006). The presence of high concentrations of dissolved solids is responsible for this phenomenon. Nitrate concentrations for all the samples are within the WHO standard limits for nitrate in groundwater (10mg/L) (WHO, 2006). Groundwater nitrate contamination may be due to wastewater discharge, effluent from on-site sanitation, and leachate from solid waste dump sites (Kuppusamy *et al.,* 2015). The values of total hardness for all the samples fall within the WHO standards (500mg/L) (WHO, 2006). The chloride concentrations in the groundwater samples all fall within the limits set by the World Health Organization standards for chloride (250mg/L) (WHO, 2006). The WHO (2006) set no standards for alkalinity and ammonia in groundwater. The dissolved oxygen (DO) and biochemical oxygen demand (BOD) levels of the samples are all within the WHO limits of each parameter (WHO, 2006). The low DO and BOD levels of the groundwater samples indicate the near absence of organic matter in the samples. This agrees with the results of a study by Kuppusamy *et al.* (2015).

The analysis of the correlation between the physicochemical parameters showed the following significant ($p > 0.05$) correlations: pH had strong positive correlations with turbidity and alkalinity, and negative correlations with nitrate and ammonia; electrical conductivity was strongly positively correlated with total dissolved solids, nitrate, ammonia, hardness and chloride, and a negative correlation with dissolved oxygen; turbidity had a positive correlation with alkalinity, however, it was negatively correlated with nitrate, ammonia, and biochemical oxygen demand; total dissolved solids showed a strong positive correlation with nitrate, ammonia, hardness, chloride and dissolved oxygen. Other significant correlations were alkalinity negatively correlated with nitrate and ammonia, nitrate positively correlated with ammonia and chloride, hardness positively correlated with chloride and negatively with dissolved oxygen, and dissolved oxygen positively correlated with biochemical oxygen demand.

Positive correlations indicate that as the concentration of one parameter increased, so did the other. However, the negative correlations indicate that as the concentration of one parameter increased, the other decreased.

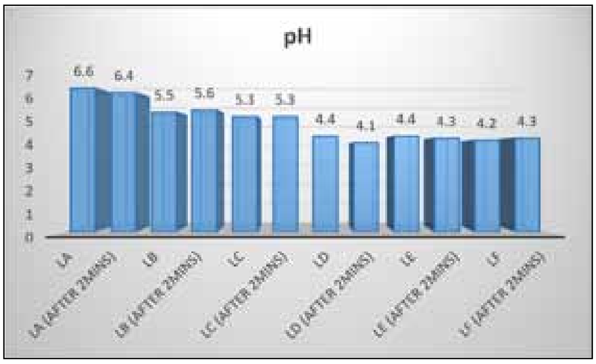

Figure 2. Concentrations of pH in all samples.

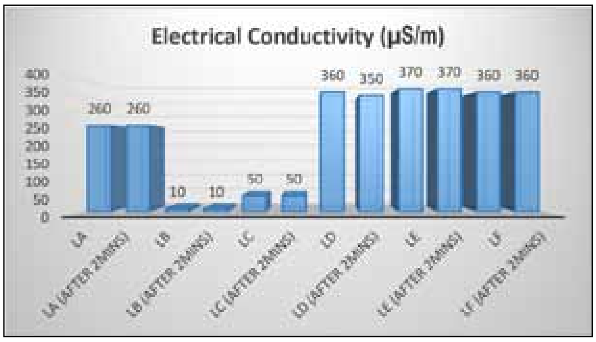

Figure 3. Concentrations of electrical conductivity in all samples.

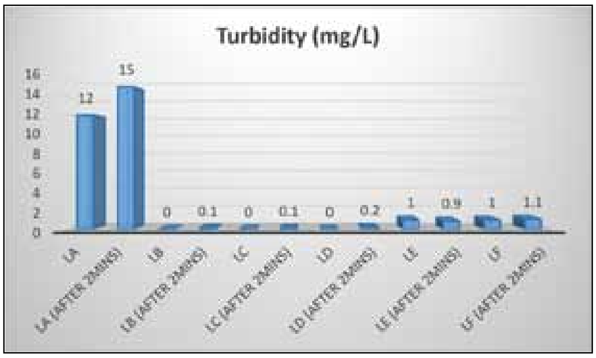

Figure 4. Concentrations of turbidity in all samples.

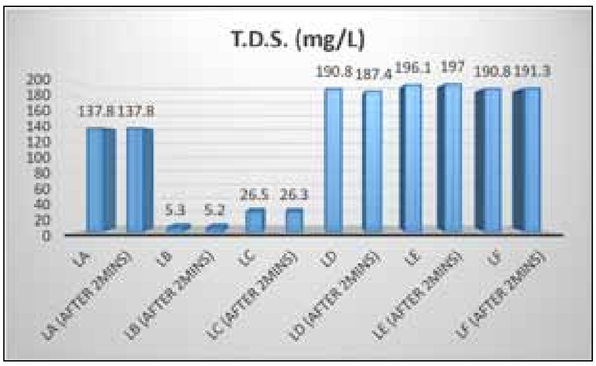

Figure 5. Concentrations of total dissolved solids in all samples.

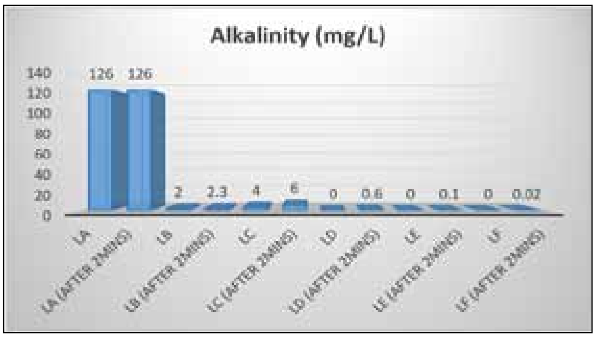

Figure 6. Concentrations of alkalinity in all samples.

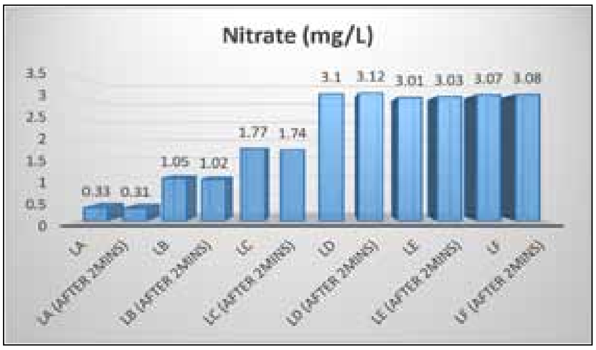

Figure 7. Concentrations of nitrate in all samples.

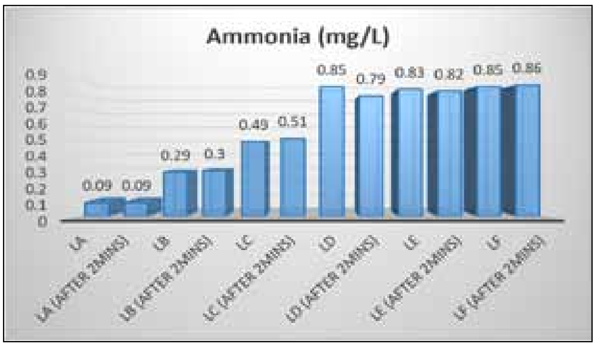

Figure 8. Concentrations of ammonia in all samples.

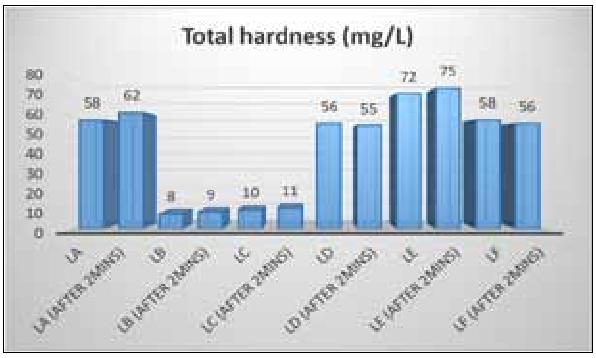

Figure 9. Concentrations of total hardness in all samples.

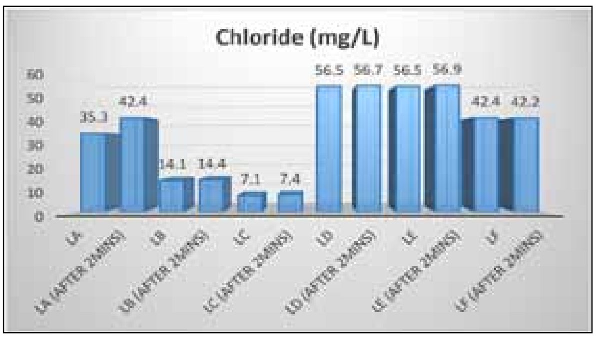

Figure 10. Concentrations of turbidity in all samples.

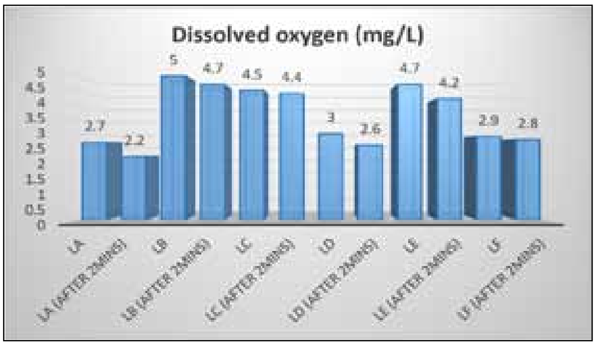

Figure 11. Concentrations of dissolved oxygen in all samples.

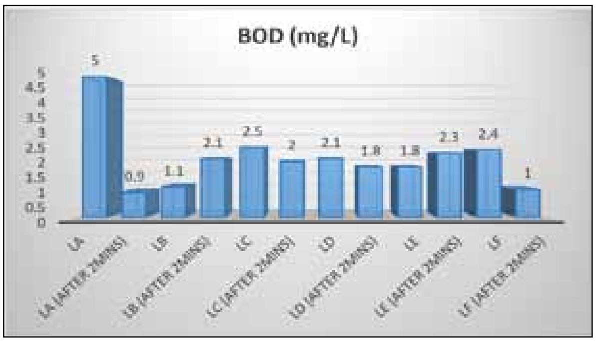

Figure 12. Concentrations of BOD in all samples.

Heavy metal analysis of water

The results of the heavy metal analysis for the water samples are shown in figures 13 and 14. LE had the highest concentration of iron (Fe) at 2.877 mg/L, while the lowest recorded concentration for Fe was 0.411 mg/L in the sample LB. The concentration of lead (Pb) was highest at LC and was 0.508 mg/L and the concentration of Pb at LB was below the detectable level. All concentrations of cadmium (Cd) from all locations were below detectable levels.

The heavy metal analysis of lead (Pb), cadmium (Cd), and iron (Fe) were carried out in all the water samples. The result, however, shows that Cd was not present in any of the samples. The concentration of lead in the samples ranged from below detectable levels (BDL) to 0.508mg/L. The highest concentration of Pb is above the standards set by the EPA (1986). The spike in lead concentrations in LC after 2 minutes is attributed to the entry of lead ions into the water due to the corrosion of plumbing materials that conduct water from the ground to the surface (USEPA, 2022). The low concentration of heavy metals in the groundwater samples is an indication that the waste in the dumpsite is mainly composed of municipal solid and household wastes. This agrees with a study carried out by Wdowczyk and Szymanska-Pulikowska (2020). The statistical analysis shows no significant difference between the mean values of the Pb concentrations in the samples from the active and non-active dumpsite. The concentrations of Fe in the groundwater samples ranged from 0.41 to 2.862mg/L. The high iron content in the water samples is attributed to the presence of ferruginized materials at various depths within the soil profile as described by Ikhile (2016) in combination with metallic ions from sedimentary rocks dissolving in groundwater (Omalu *et al.,* 2012). There is a significant difference between the mean values of Fe concentrations in the groundwater samples collected from the active and non-active dumpsite at p<0.05. The higher concentration of Fe in the groundwater samples from the non-active dumpsites may be due to the low pH of the water as low pH i.e. high acidity increases the solubility of metals (Wuana and Okieimen, 2011).

Correlation analysis for heavy metals and other parameters showed that at $p > 0.05$, iron was positively correlated with electrical conductivity, total dissolved solids, nitrate, hardness, and chloride. This showed that with an increase in the concentrations of these parameters in water, the concentration of iron increased.

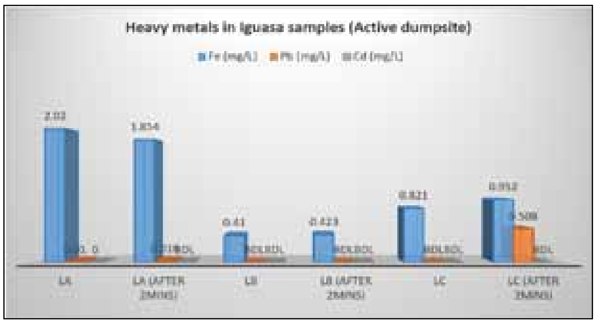

Figure 13. Heavy metal concentrations in samples from the active dumpsite.

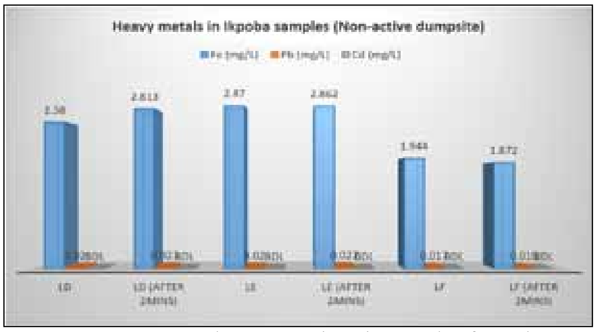

Figure 14. Heavy metal concentrations in samples from the non-active dumpsite.

Microbiological analysis of water samples

For the heterotrophic plate count (Table 1), the highest mean heterotrophic plate count was 27.5cfu/ml from LB, which increased to 44cfu/ml (the highest) after two (2) minutes. The lowest mean heterotrophic plate count was 4cfu/ml from LE and it increased to 4.5cfu/ml after two (2) minutes. The lowest mean count after two minutes was 3cfu/ml from LD. The repeat coliform count (Table 2) showed that the highest mean coliform count was 3.5cfu/ml for LB, which decreased to 3cfu/ml (highest) after two (2) minutes. The lowest mean coliform count was 1.5cfu/ml for LD, LE, and LF, while the lowest mean coliform count was 1cfu/ml for LE after two (2) minutes.

The highest heterotrophic plate count value among all the samples was 44cfu/ml, obtained from LB after 2 minutes. This high count is attributed to the presence of microbial biofilms within the water-conducting systems at the sampling location. This is as described by Gavriel *et al.* (1998). There was no significant difference between the heterotrophic plate count values initially and after 2 minutes for all groundwater samples except LB, at p<0.05. The coliform count reveals a maximum count of 3.5cfu/ml. According to studies by Sebiawu *et al.* (2014) and Mishra *et al.* (2016), coliform count values below 16cfu/ml are not threatening to human health. This means that the samples used in the study are within safe limits for human consumption. The statistical analysis revealed that there was no significant difference between the coliform counts for all samples initially and after 2 minutes, at p<0.05.

Table 1. Heterotrophic plate count (HPC).

Sample location	HPC		HPC after 2 minutes		Log_{10} of HPC		Log_{10} of HPC after 2 minutes	
	Mean	SD	Mean	SD	Mean	SD	Mean	SD
LA	15.50	0.71	18.00	0.00	2.19	0.02	2.26	0.02
LB	27.50	0.71	44.00	1.41	2.44	0.01	2.64	0.01
LC	15.50	4.95	35.00	7.07	2.18	0.14	2.54	0.14
LD	6.00	1.41	3.00	1.41	1.77	0.10	1.45	0.10
LE	4.00	0.00	4.50	0.71	1.60	0.00	1.65	0.00
LF	5.50	0.71	6.50	0.71	1.73	0.06	1.81	0.06

Table 2. Tabular representation of the repeat coliform count.

Sample location	Coliform count (cfu/ml)		Coliform count after 2 minutes (cfu/ml)		Log_{10} of coliform count		Log_{10} of coliform after 2 minutes	
	Mean	SD	Mean	SD	Mean	SD	Mean	SD
LA	2.50	0.71	1.50	0.71	1.39	0.12	1.15	0.21
LB	3.50	0.71	3.00	1.41	1.54	0.09	1.45	0.21
LC	2.50	0.71	4.50	0.71	1.39	0.12	1.65	0.07
LD	1.50	0.71	1.50	0.71	1.15	0.21	1.15	0.21
LE	1.50	0.71	1.00	0.00	1.15	0.21	1.00	0.00
LF	1.50	0.71	1.50	0.71	1.15	0.21	1.15	0.21

The bacteria isolated and identified from the water samples are displayed in Table 3. A total of ten (10) species of microorganisms were identified. They are *Enterobacter aerogenes*, *Escherichia coli*, *Bacillus pumilus*, *Morganella morganii, Klebsiella oxytoca*, *Pseudomonas aeruginosa*, *Alcaligenes faecalis, Bacillus subtilis, Proteus vulgaris* and *Serratia marcescens.*

Table 3. Bacteria identity and distribution.

Sample location	Bacterial Identity and distribution
LA	*Enterobacter aerogenes*, *E. coli*, *Bacillus pumilus*, *Morganella morganii.*
LB	*Klebsiella oxytoca*, *E. coli*, *Pseudomonas aeruginosa*, *Alcaligenes faecalis*
LC	*E. coli, Enterobacter aerogenes, Bacillus subtilis, Proteus vulgaris.*
LD	*E. coli, Enterobacter aerogenes, Serratia marcescens, Bacillus pumilus.*
LE	*E. coli, Enterobacter aerogenes, Serratia marcescens, Bacillus pumilus.*
LF	*Enterobacter aerogenes, E. coli, Bacillus pumilus, Morganella morganii.*

Keys: Active dumpsite (LA, LB, LC); Non-active dumpsite (LD, LE, LF).

Table 4 shows the percentage occurrence of the bacteria species. *Escherichia coli* had the highest percentage occurrence (25%), while the least occurrence was seen with *Klebsiella oxytoca*, *Pseudomonas aeruginosa*, *Alcaligenes faecalis, Bacillus subtilis* and *Proteus vulgaris* which were 4.17%.

Table 4. Frequency of occurrence of bacteria in samples.

Microorganism	Frequency of occurrence (%)
Enterobacter aerogenes	20.83
Escherichia coli	25
Bacillus pumilus	16.67
Morganella morganii	8.33
Klebsiella oxytoca	4.17
Pseudomonas aeruginosa	4.17
Alcaligenes faecalis	4.17
Bacillus subtilis	4.17
Proteus vulgaris	4.17
Serratia marcescens	8.33

The values of pH, turbidity, alkalinity, and BOD were higher in the samples from the active dumpsite, while the values of electrical conductivity, total dissolved solids, nitrate, ammonia, total hardness, chloride, and dissolved oxygen were higher in the samples from the non-active dumpsite. This can be attributed to the range of different point sources of contaminants as discovered by other researchers (Oyelami *et al.,* 2013; Oko *et al.,* 2017). The concentrations of Fe in the non-active dumpsite samples were higher than those from the samples of the active dumpsite. This may be due to leaching from the dumpsite, reducing conditions in the groundwater aquifer, and rusty pipes and pumps in the borehole system as explained by Kuppusamy *et al.* (2015). Leaching occurs when moisture enters the refuse in a dumpsite. Pb was detected in all samples from the non-active dumpsite but was not found in three of the samples taken from the active dumpsite which may be due to the presence of Fe-oxidizing bacteria (Kuppusamy *et al.,* 2015). The heterotrophic plate count and coliform counts were higher in the samples from the active dumpsite than those from the non-active dumpsite. This agrees with the results of Asibor and Oborakpororo (2019) who stated that microbial diversity increases as more waste accumulates.

4. CONCLUSION

Groundwater contamination is a major issue that affects human and environmental health. Different contaminants from dumpsites can leach or infiltrate through the soil and into groundwater. This study attempted to evaluate the quality of groundwater from an active dumpsite and compare it with that from a non-active dumpsite. From the results of this study, it is concluded that the groundwater from the non-active dumpsite has more inorganic contaminants than the active dumpsite groundwater. It is seen also that the groundwater from the active dumpsite area has more microbial contamination than the non-active dumpsite. While the level of microbial contamination is not hazardous, it can be further reduced by treating the water with boiling or chlorination. Finally, when the physicochemical properties and heavy metal content of the samples are compared, the groundwater of the active dumpsite is less contaminated than that of the non-active dumpsite.

References

Adekunle, I. M., Adetunji, M. T., Gbadebo, A. M. and Banjoko, O. P. (2007). Assessment of groundwater quality in a typical rural settlement in southern Nigeria, *International Journal of Environmental Research and Public Health,* **4**(4): 307 - 318.

Akpoveta, V., Okoh, B. E. and Osakwe, S. A. (2011). Quality assessment of borehole water used in the vicinities of Benin, Edo State, and Agbor, Delta, State, *Current Research in Chemistry,* **3**(1): 62 - 69.

Andricevic, R., Di Dato, M., Galesic, M. and Simundic, P. (2011). A novel screening tool for health risk in recreational waters near estuary: the carrying capacity indicator, *Science of the Total Environment,* **694**: 133 - 158.

Asibor, G. and Oborakpororo, O. (2019). Well, water quality assessment using water quality index in Warri Metropolis, Delta State, Nigeria, *International Journal of Environment and Pollution Research,* **7**(3): 45 - 52.

Bekhit, H. M., El-Kordy, M. A. and Hassan, A. E. (2009). Contaminant transport in groundwater in the presence of colloids and bacteria: model development and verification, *Journal of Contamination in Hydrology,* **108**(3-4): 152 - 167.

Buchanan, R. E., and Gibbons, N. E. (1974). Bergey's Manual of Determinative Bacteriology, 8th Edition. Williams and Wilkins Co.: Maryland, USA. 1246p.

Calow, R. C., McDonald, A. M., Nicol, A. L. and Robins, N. S. (2011). *Groundwater Security and Drought in Africa: Linking Availability, Access, and Demand.* Volume 1. University Press:

Cambridge, UK. 65p.

David, S. G. T. (2011). *The Environmental Impact of Groundwater Exploitation on African Grasslands: Examples and a Case Study of the Kalahari Region*. Volume 1. University of Sheffield: Sheffield, UK. 102p.

Enyinna, G. C. and Nkemdirim, V. U. (2018). Impact of the proliferation of borehole development projects on groundwater quality in Abia State, Nigeria, *International Journal of BioSciences and Technology,* **11**: 20 - 29.

EPA (Environmental Protection Agency) (1986). *Ambient Water Quality Criteria for Bacteria.* EPA 440/5-84-002. US EPA: Washington DC, USA. 411p.

Gavriel, A. A., Landre, J. P. and Lamb, A. J. (1998). Incidence of mesophilic *Aeromonas* within a public drinking water supply in north-east Scotland, *Journal of Applied Microbiology,* **84**: 383 - 392.

Hillel, R. and Rabideau, A. J. (2000). Approximate analysis of the contaminant of contaminated sites prior to remediation, *Water Science and Technology,* **42**: 1 - 2.

Holmes, J. (2007). *Climate Change and Water Resources*. Water Aid Document Number 288701. IntechOpen: London, UK. 61p.

Ikhile, C. I. (2016). Geomorphology and hydrology of the Benin Region, Edo State, Nigeria, *International Journal of Geosciences,* **7**: 144 - 157.

Kelly, W. R., Panno, S. V. and Hackley, K. (2011). *Groundwater and Surface Water Studies and Websites.* Bulletin B-74. Prairie Research Institute: Illinois, USA. 18p.

Kuppusamy, S. S., Muthusamy, P., Murugesan, B. and Murugesan, A. (2015). Assessment of groundwater contamination in soil due to leachate migration from an open dumping site of Dharampuram Municipality, Tamilnadu, India, *Advances in Applied Science Research,* **6**(12): 53 - 58.

Lu, O. (2004). GAC verification procedures save time, water, and *Opflow,* **30**(1): 9 - 11.

Minh, P. T. P., Castle, J. W. and Rodgers, J. H. (2011). *Application of Water Quality Guidelines and Water Quantity Calculations to Decisions for Beneficial Use of Treated Water.* 1st Edition. McGraw Hill: New York, USA. 79p.

Mishra, M. K., Prasad, S. and Jha, A. M. (2017). Groundwater quality assessment near municipal waste dump site - a case study, *Journal of Chemical, Biological and Physical Sciences,* **7**(1): 14 - 18.

Oko, O, J., Aremu, M. O. and Andrew, C. (2017). Evaluation of the physicochemical and heavy metal content of groundwater sources in Bantaji and Rafin-Kada settlements of Wukari Local Government Area, Taraba State, Nigeria, *Journal of Environmental Chemistry and Ecotoxicology,* **9**(4): 43 - 53.

Omalu, C. J., Mohammed, A. Z., Olamide, P. I., Ayanwale, V. A., Adeniran, V. A. and Gbise, S. (2012). Bacteriological and physicochemical analysis of sachet water in North Central Nigeria, *Journal of Pharmaceutical and Biomedical Sciences,* **21**(8): 1 - 4.

Oyelami, A. C., Ojo, A. O., Aladejana, J. A. and Agbede, O. O. (2013). Assessing the effect of a dumpsite on groundwater quality: a case study of Aduramigba Estate within Osogbo Metropolis, *Journal of Environment and Earth Sciences,* **3**(1): 120 - 132.

Rodak, C. M., Silliman, S. E. and Bolster, D. (2011). Reliability, resilience and vulnerability criteria for the evaluation of human health risks, *Journal of the American Water Resources Association,* **50**(1): 14 - 28.

Sebiawu, G. E., Fosu, S. A. and Saana, S. B. (2014). Physicochemical and bacteriological analysis of borehole water samples from the Wa Municipality of the Upper West Region, Ghana, *International Journal of Engineering Research and Technology,* **3**(5): 1959 - 1967.

Silderberge, M. S. (2003). *Higher Education Chemistry: The Molecular Nature of Matter and Change,* 1st Edition. McGraw Hill: New York, USA. 281p.

Singh, C. M., Kumar, B., Mandi, S. and Chandra, K. (2012). Effect of drought stress on rice: a review on morphological and physiological characteristics, *Trends in Biosciences*, **5**(4): 261 - 265.

Talafre, J. and Knabe, F. (2009). Climate Change and Water: An Overview from the WWDR3. Available online at www.unesco.org/news/en/natural-sciences/environment/water/single-view-fresh-water/news/climate_change_and_water_an_overview_from_the_wwdr3. Accessed 11th January 2021.

USEPA (the United States Environmental Protection Agency) (2022). Groundwater and drinking water. Available online at www.epa.gov/ground-water-and-drinking-water/basic-information-about-lead-drinking-water/. Accessed February 27th, 2022.

Wdowczyk, A. and Szymanska-Pulikowska, A. (2020). Differences in the composition of leachate from active and non-operational municipal waste landfills in Poland, *Water,* **12**: 1 - 15.

WHO (World Health Organization) (2006). *Guidelines for Drinking Water Quality.* 3rd edition. WHO: Geneva, Switzerland. 668p.

Wuana, R. A. and Okieimen, F. E. (2011). Heavy metals in contaminated soils: A review of sources, chemistry, risks and best available strategies for remediation. Available online at https://doi.org/10.5402/2011/402647. Accessed May 15th, 2020.

WWDR (World Water Development Report) (2011). Water for a Sustainable World. Volume 3. United Nations: New York, USA. 391p.

JJEES

JJEES (2022) 13 (4): 278-285
ISSN 1995-6681

Jordan Journal of Earth and Environmental Sciences

The Reduced Paleostress Tensors Based on Fault-Slip Data of Dana Conglomerate Formation in Ed Dhira Area, Dead Sea-Jordan

Mohammad Al-Adamat* and Abdullah Diabat

Department of Applied Earth and Environmental Sciences, Faculty of Earth and Environmental Sciences, Al al-Bayt University. Al-Mafraq-Jordan

Received 15th February 2022; Accepted 29th April 2022

Abstract

This study presents paleo stress results based on fault-slip data measured in the Dana Conglomerate Formation (Neogene) in Ed Dhira area east of the Dead Sea basin. Stress inversion of fault-slip data was carried out utilizing an improved Right-Dihedral method, followed by rotational optimization. Results revealed the existence of a strike-slip regime in all stress tensors, in which σ1 (SHmax) and σ3 (Shmin) are usually sub-horizontal and σ2 is sub-vertical. The stress ratio (R) ranged between 0.25 - 0.67 and the stress index (R') ranged between 1.33- 1.75. The SHmax σ1 oriented ESE– WNW within a range of 15° (113- 128) of all stress tensors. The results revealed about 10°-20° anti-clockwise rotation compared with the main trend of the Dead Sea stress (NW-SE SHmax) to WNW-ESE trend in the study area. The stress variations are due to the block rotation along the main faults in the study area and/ or may be due to stress changes in time.

Keywords: *Paleostress, Dana Conglomerate, Neogene, Dead Sea Transform, Jordan.*

1. Introduction

Paleostress analysis aims to classify stress systems acting in the past from their record in deformation structures, singularly from fault-slip data (Simón, 2019). Determination of the paleo stress tensors is an essential tool to characterize successive tectonic episodes in deformed rock (Radaideh and Melichar, 2015). The direction of the paleo stress can be determined successfully depending on the analysis of different types of geological structures, such as faults, fold axes, joints, veins, stylolites, and dykes (Zoback, 1992). Collections of small faults from a restricted area like an outcrop or a quarry can be analyzed to reconstruct the local paleo stress field (Fossen, 2016). Meso-scale faults are common. Their data can be widely collected, and their mechanical analysis provides the reconstruction of the successive stress states (Hardy et al., 2010). They are more widely used than large-scale faults to determine the stress field with a greater spatial resolution (Yamaji, 2007). Determinations of reduced stress tensors using fault slip data yield the orientation of principal stress axes and the ratio Φ or R of the differences between principal stress magnitudes. The use of rupture and friction laws allows the determination of the two remaining unknowns, that is, the reconstruction of the complete stress tensor (Angelier, 1989).

The goal of paleo stress inversion is to characterize what is known as the reduced stress tensor (Igwe and Okonkwo, 2016).) The reduced stress tensor has four parameters to define the full stress tensor: the principal stress axes σ 1 (maximum compression), σ 2 (intermediate compression), and σ 3 (minimum compression), and the Stress Ratio R = (σ 2 - σ 3) / (σ 1 - σ 3) (Delvaux and Sperner, 2003). Moreover, multiple methods for paleo stress analysis have been developed from the concept of stress inversion (e.g., Žalohar and Verbac, 2007; Delvaux and Sperner, 2003; Yamaji, 2000; Sperner, et al.,1993; Angelier and Mechler, 1977). The application of these methods is based on Wallace and Bott hypothesis (Bott, 1959; Wallace, 1951), which describes that the direction of slip in planar structure is parallel to the maximum shear stress of the reduced stress tensor.

The area being studied is located within the Ed Dhira area, to the east of the Dead Sea Basin (DSB). The DSB is a part of the most magnificent structural element in the region, the Dead Sea Transform Fault (DSTF) (Figures 1a and b). Furthermore, the Dana Conglomerates Formation (DC) is a clastic deposit that was formed during a significant episode of uplift and erosion following the regression of the Tethys Ocean in the late Eocene (Khalil, 1992). It is deposited in tectonically unstable basins during an extensional tectonic stage related to an early rifting phase (Powell, 1988). This research aims to shed light on the paleostresses of the DC Formation in five established measurement stations based on fault-slip data, as no research has been conducted in the current study area.

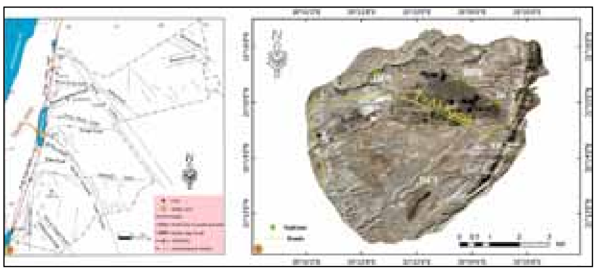

Figure 1. Structural setting of the study area. (a) The structural pattern of Jordan shows the location of the study area (modified from Diabat and Masri, 2005), and (b) a Satellite image of the study area with the established field measurement stations.

* Corresponding author e-mail: m.aladamat90@gmail.com

2. Geological setting

2.1. Stratigraphy

The outcropping rocks in the area under investigation range from the Upper Cretaceous to the Quaternary (Figure 2 a and b).

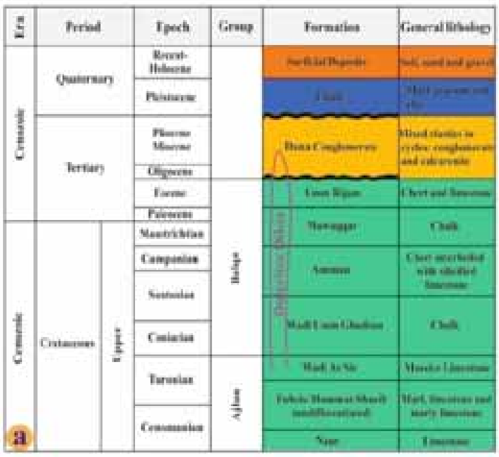

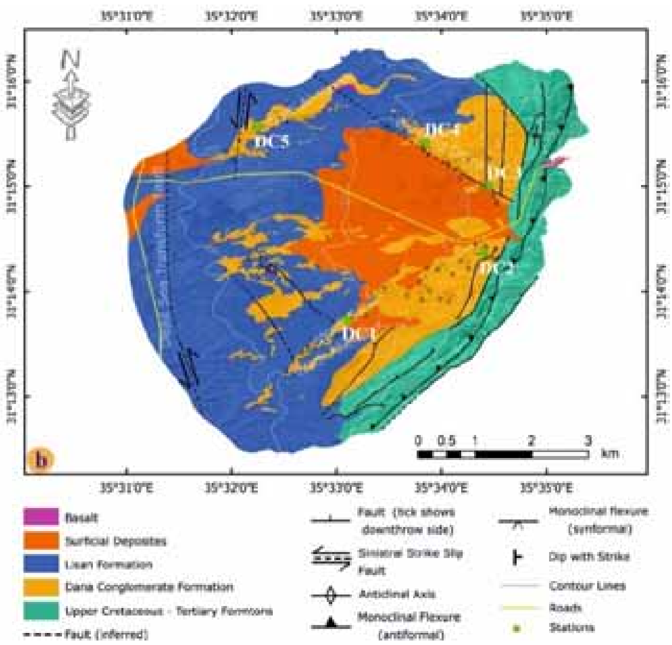

Figure 2. (a)The lithostratigraphic units exposed in the study area (modified from Powel 1988; Khalil 1992), and (b) the Geological map of the study area with the established field measurement stations.

2.1.1. Dana Conglomerate Formation (Oligo-Pliocene)

The formation is exposed in different locations within the study area (Figure 2b). According to Powell (1988), this formation can be divided into informal lower- and upper-members which are equivalent to the subdivision of Bender (1974), who also pointed to this unit as the Syn-tectonic Conglomerate. Moreover, the lower member is composed of thick beds of pebble-boulder conglomerate comprising poorly graded, well-rounded, clast of chert, chalk, and chalky limestone is which derived from the Eocene formations (Powell, 1988 and Khalil, 1992). The formation's upper member is made up of thick beds of clast-supported, poorly sorted, a well-rounded pebble-to-boulder conglomerate with a calcarenite/siliciclastic matrix. The lower member has a distinctive pink-tan and white color in the field, while the top member weathers to a brown-yellow tone (Powell, 1988). As it was mentioned earlier the formation has deposited in tectonically unstable basins during an extensional tectonic phase related to an early rifting stage.

2.2. Tectonic Setting

The Dead Sea Transform Fault (DSTF) is a left-lateral strike-slip fault system, about 1100 km in length (Masson et al., 2015). It accommodates strike-slip motion between the Sinai sub-plate to the West and the Arabian plate to the East (Weinstein et al., 2020). It links the Red Sea spreading center in the south to the Bitlis-Zagros zone of plate convergence in southern Turkey to the north (Figure 3a) (Khon et al., 2019). The DSTF is composed of numerous fault segments and associated transtensional and transpressional features, such as pull-apart basins, fault escarpments, and pressure ridges (Atallah and Al–Taj 2004; Atallah 1992; Garfunkel 1981). In Jordan, the DSTF comprises two main segments, the Wadi Araba Fault (WAF) in the south and the Jordan Valley Fault (JVF) in the north, which bound the Dead Sea Basin (DSB) in the middle (Figure 3b) (Garfunkel 1981). The DSB is an elongated deep Pull-apart basin, whose overall length is about 150 km, and its width ranges between 15–20 km (Wetzler, et al., 2015). Nevertheless, in the study area, the main DSTF is not exposed at the surface, but its trace is inferred depending on the geomorphology and geophysical pieces of evidence (Powell, 1988 and Khalil, 1992)

Ed Dhira area lies on the eastern flank of the DSB. It is surrounded by the Ed Dhira Monocline and splay fault to the east, and the Siwaqa fault to the northeast (Figure 3c) (Masri, 1997). The majority of the folds formed in the area are related to flexural juxtaposes of the associated faults; these include the Ed Dhira fault-monocline which is the main flexure spanning from the Siwaqa fault in the north to Wadi Assal in the south. It forms an arc-like structure trending NNW in the north, N in the middle, and NE in the southern part (Powell, 1988) (Figure 3c). Ed Dhira fault is a significant NE-SW trending splay fault that branches off the main DSTF in the vicinity of Wadi Assal, about 3.5 kilometers south of the studied area. The beds along the fault trace are frequently crushed or shattered by small faults. This fault disappears and passes into a main monoclinal flexure with minor faults (Powell, 1988) (Figure 3c). Rhomb-shaped faulted blocks are bounded by N-S and NW-SE trending faults and are well preserved in strata of the DC Formation in the Ed Dhira area (Figure 2b) (Khalil, 1992). A study carried out by Al- Adamat and Diabat (2021) in Ed Dhira area, proved the occurrence of syn-depositional extensional structures as normal faults and associated systems like horsts and grabens, joints, plumose joints, tension gashes, and veins. Horst and graben structures with a displacement range from a few centimeters to more than 3 m were observed in three stations of the study area, indicating N–S, NE–SW, and E–W extensional directions, respectively. In addition to negative flowers, the structure was observed in two stations associated with N–S- and NW–SE-directed strike-slip faults. This is explained as transmission related to the Dead Sea stress field.

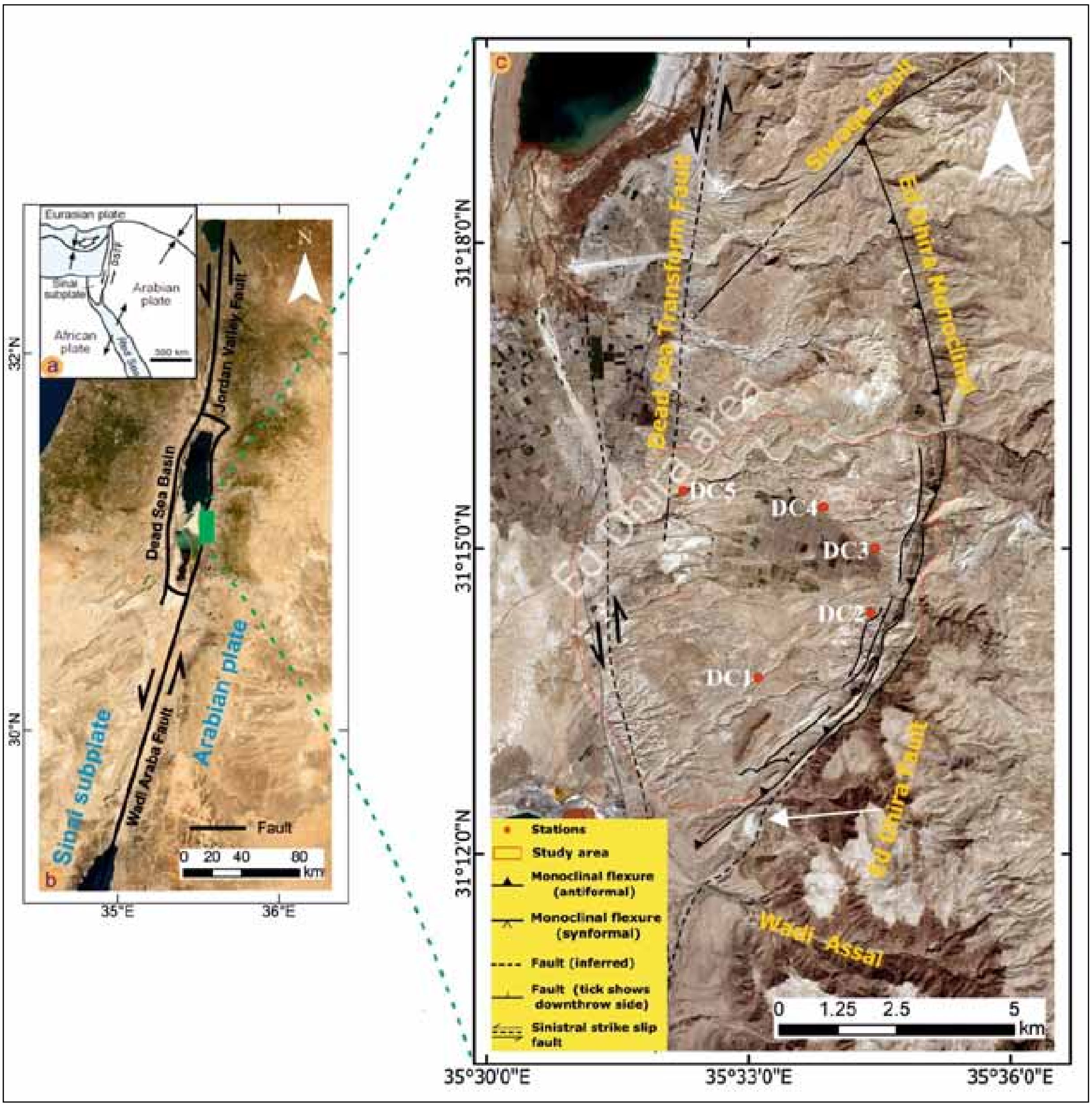

Figure 3. (a) Tectonic setting of the DSTF, (b) Satellite image of the DSTF segments in Jordan, and (c) Satellite image showing the tectonic setting of Ed Dhira area and the main geological structures of the study area.

3. Methodology

The study was dependent mainly on the fieldwork which has been included five investigated measurement stations. Collecting data have been performed by measuring the dip and strike of faults, and the trend and plunge of slickenlines on the fault planes within the Dana Conglomerate Formation. Field data including fault planes with slip lines and sense of movement have been used to calculate the orientation of the principal stresses ($\sigma1$, $\sigma2$, and $\sigma3$): the principal stress axis $\sigma1$ (maximum compression), $\sigma2$ (intermediate compression) and $\sigma3$ (minimum compression) and the ratio of principal stress difference $R = (\sigma2 - \sigma3)/(\sigma1 - \sigma3)$ which characterize the shape of the stress tensor, have been determined using successively the improved right dihedron method (Angelier and Mechler, 1977) and the rotational optimization method (Delvaux and Sperner, 2003). Both methods have been applied to utilize a free source computer software named Win Tensor (Delvaux, 2012). It is widely used by several geologists for reconstruction fractures analysis and crustal stresses. Moreover, the stress tensors are divided into the following: radial /pure/ strike-slip extensive, extensive / pure/ compressive strike-slip, or strike-slip, pure, radial compressive depending on the relative magnitude of the intermediate axis and given by stress ratio R (Delvaux et al.,1997) (Figure 4). On the geological map of the studied area, these tensors are exhibited with the orientation of both horizontal principal stress (SHmax) and horizontal minimum stress axes (Shmin).

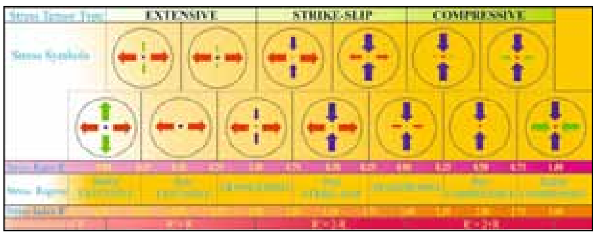

Figure 4. Stress tensor representation for different stress regimes (after Delvaux et al.,1997).

4. Results

Based on the availability and accessible data, the studied area has been divided into five stations (Figure 3c). The fault-slip data measurements have been performed by measuring slickenside lineations on the fault planes (Figure 5).

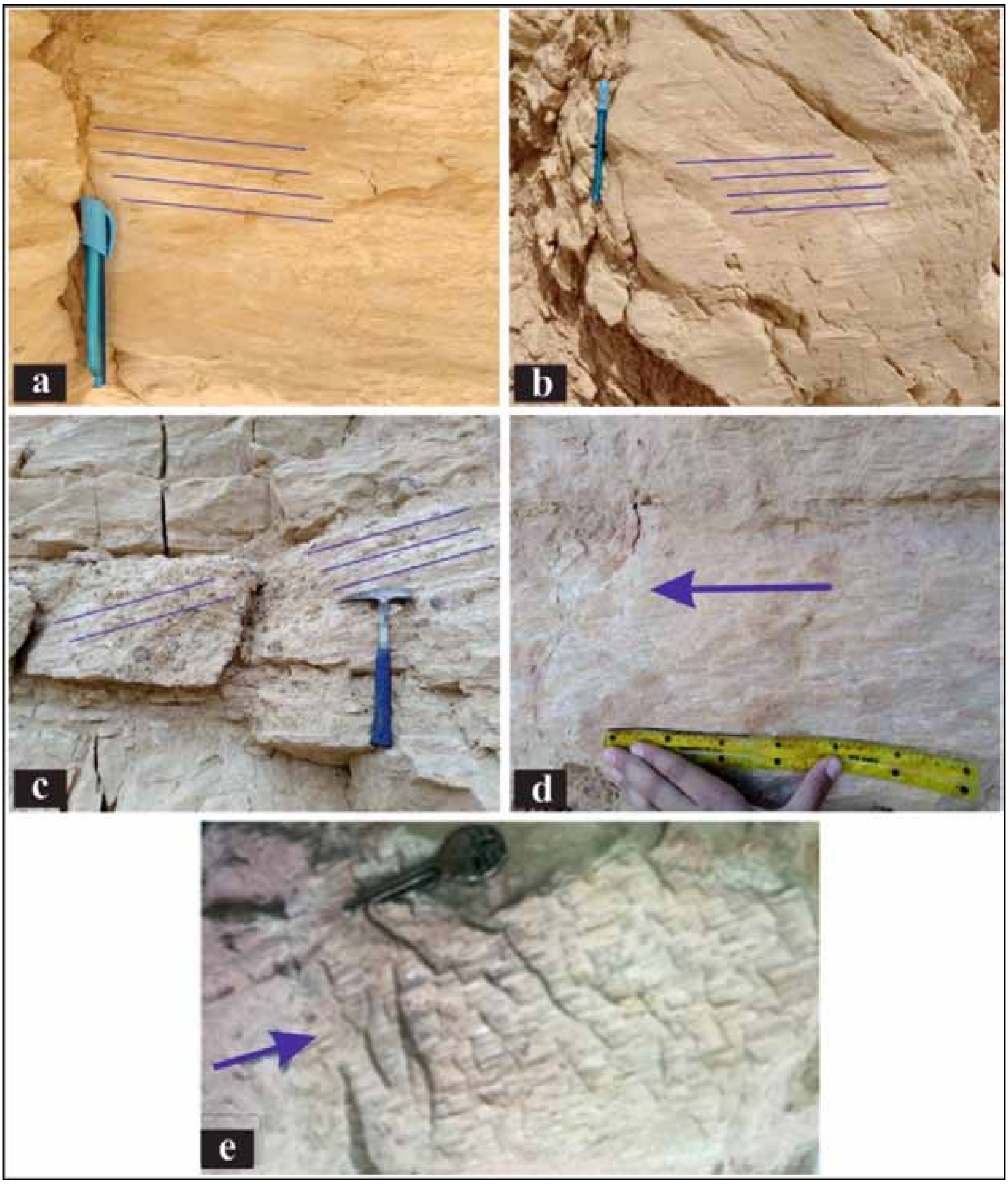

Figure 5. Kinematic indicators along the fault planes in the study area; (a and b) Horizontal slickenlines, (c) Oblique slickenlines, and (d & e) Mineral steps of dextral and sinistral movement, respectively.

4.1. Field station DC1

This station is situated at Wadi Saad (as it is known locally) (Figure 2b). In this station, ten fault-slip data measurements were performed. After applying the improved right dihedron and rotational optimization methods respectively, the consequences show that the stress tensor is characterized by σ1: 25/293, σ2: 65/100, and σ3: 05/ 201 with R = 0.25. It belongs to a pure strike-slip regime and indicates WNW–ESE compression NNE –SSW extension (Figures 6a and b). This stress tensor produced the N–S to NNW–SSE sinistral strike-slip faults in the studied area.

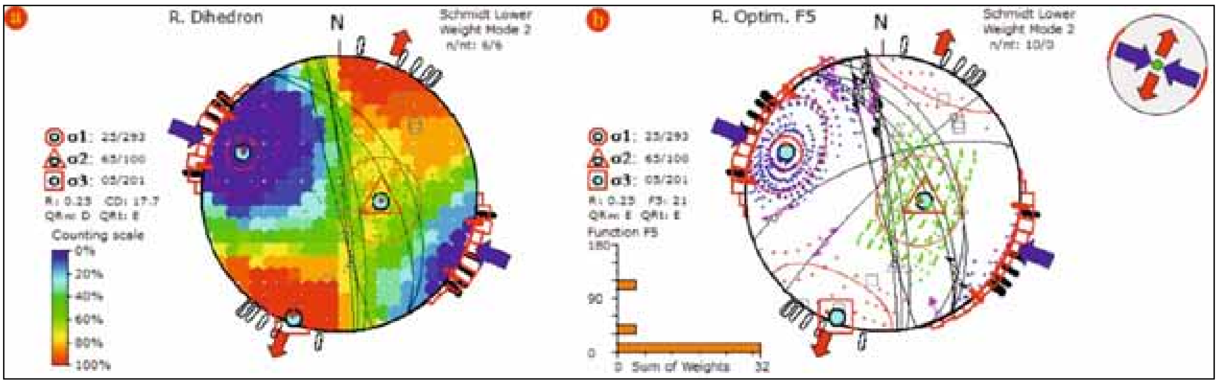

Figure 6. (a and b). Stress tensor shows WNW–ESE compression and NNE–SSW extension; Inward arrows represent compression, outward arrows denote tension, the circle is σ1, the triangle indicates σ2 and the square is σ3 orientation.

4.2. Field station DC2

The station lies about 220 m from Al-Karak- Dead Sea Road (Figure 2b). Nine fault-slip data measurements were performed in DC2. After applying the improved right dihedron and rotational optimization methods separately, the outcomes show that the stress tensor is characterized by σ1: 04/293, σ2: 80/179, and σ3: 09/ 024 with R = 0.56. It belongs to the pure strike-slip regime and indicates NNE–SSE extension and WNW– ESE compression (Figures 7a and b). This stress tensor is accountable for the formation of NNW–SSE sinistral strike-slip faults in the studied area.

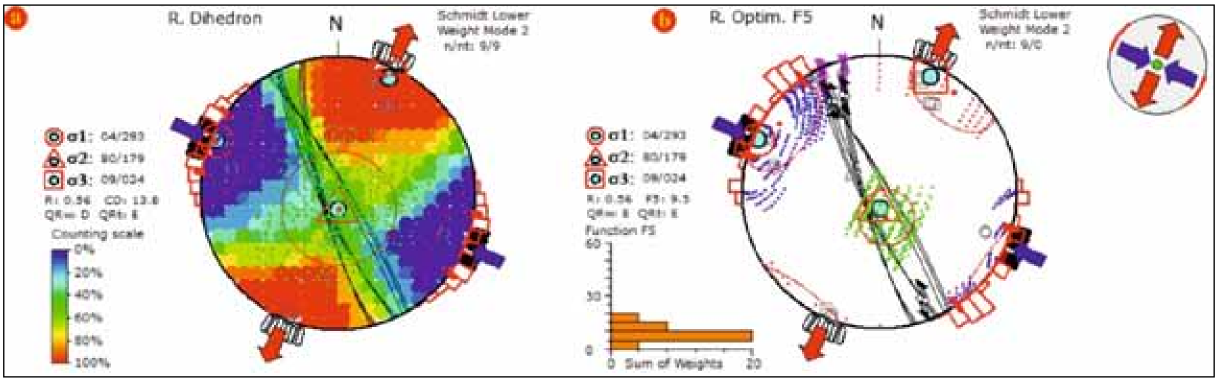

Figure 7. (a and b). Stress tensor shows NNE–SSE extension and WNW– ESE compression; Inward arrows denote compression, outward arrows represent tension, the circle is σ1, the triangle is σ2 and the square indicates σ3 orientation.

4.3. Field station DC3

This station is located at Wadi Wadeaa (as it is known locally) (Figure 2b). Here, twenty-five fault-slip data measurements were carried out in the analysis. After applying the improved right dihedron and rotational optimization methods, the result is the stress tensor which is characterized by σ1: 11/300, σ2: 67/182, and σ3: 20/ 034 with R = 0.54. It belongs to the pure strike-slip regime and indicates NNE–SSE extension and WNW – ESE compression (Figures 8a and b). This stress tensor is responsible for the formation of conjugated NNW–SSE sinistral strike-slip faults and ENE–WSW dextral strike-slip faults in the studied area.

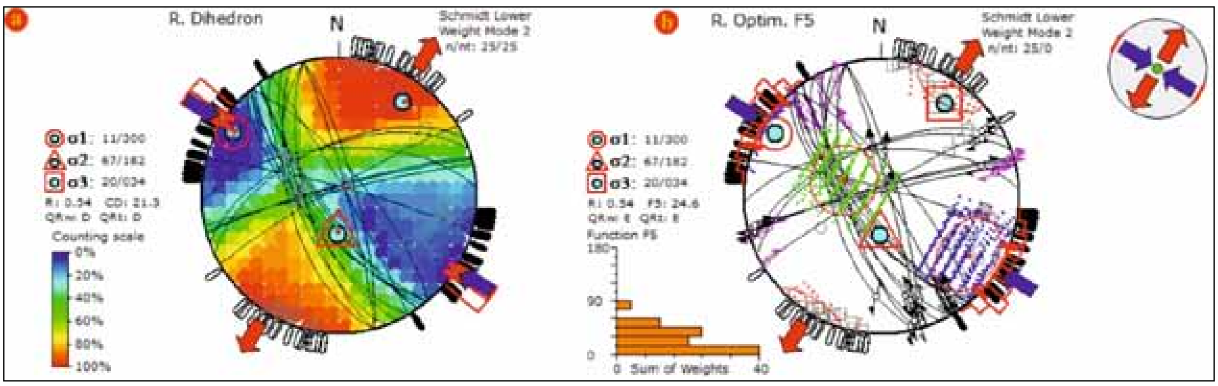

Figure 8. (a and b). Stress tensor shows NNE – SSE extension and WNW – ESE compression; Inward arrows represent compression, outward arrows denote tension, the circle is σ1, the triangle indicates σ2 and the square is σ3 orientation.

4.4. Field station DC4

The DC4 is situated at Wadi Ed-Dhira (Figure 2b). Nine fault-slip data measurements were performed at this location. After applying the improved right dihedron and rotational optimization methods separately, the outcomes show that the stress tensor is characterized by σ1: 23/308, σ2: 62/162, and σ3: 14/ 044 with R = 0.67. It belongs to the pure strike-slip regime and indicates NE–SE extension and NW – SE compression (Figures 9a and b). This stress tensor produced the N–S sinistral strike-slip faults in the studied area.

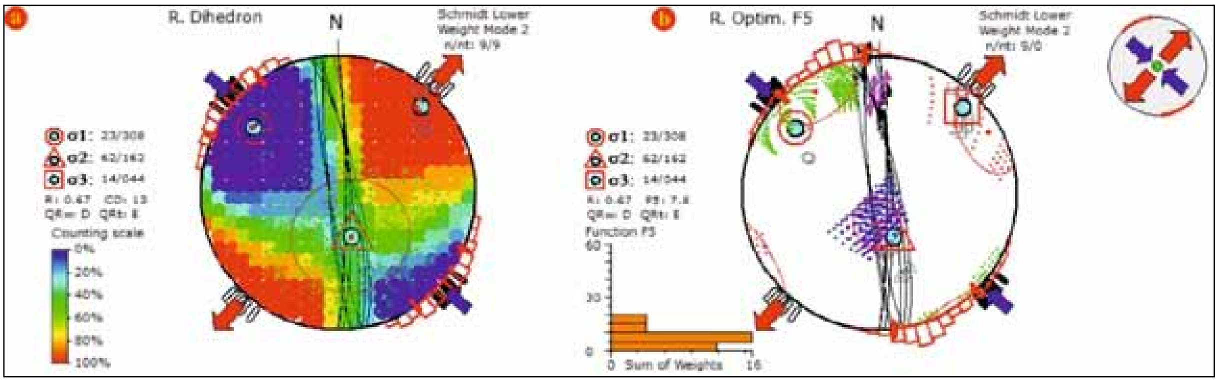

Figure 9. (a and b). Stress tensor shows extension and NW–SE compression; Inward arrows denote compression, outward arrows represent tension, the circle is σ1, the triangle is σ2 and the square indicates σ3 orientation.

4.5. Field station DC5

The station lies at Wadi Al-Karak, northwestern of the study area (Figure 2b). Twenty-two fault-slip data measurements were carried out. After applying the improved right dihedron and rotational optimization methods respectively, the results show that the stress tensor is characterized by σ1: 02/123, σ2: 85/236, and σ3: 04/ 033 with R = 0.45. It belongs to the pure strike-slip regime and indicates NNE–SSE extension and WNW – ESE compression (Figures 10a and b). This stress tensor is responsible for the development of conjugated NNW–SSE sinistral strike-slip faults and E–W to ENE–WSW in the studied area.

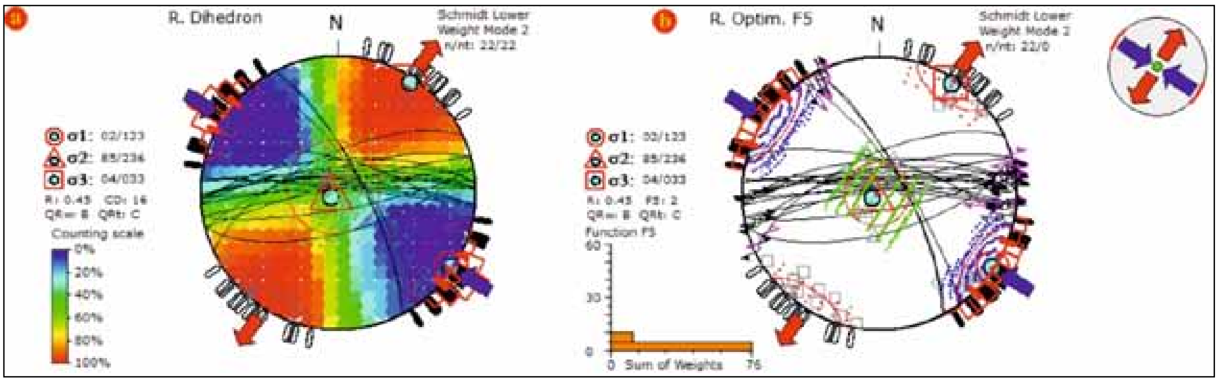

Figure 10. (a and b). The stress tensor shows NNE–SSE extension and WNW– ESE compression. Inward arrows represent compression, outward arrows denote tension, the circle is σ1, the triangle indicates σ2 and the square is σ3 orientation.

5. Discussion

From the data in Table 1 and Fig. 11, it is noticed that all of the stress tensors belong to the pure strike-slip regime as R ratios range between 0.25 – 0.67, and the stress index (R') ranges between 1.33 – 1.75. The calculated results of stress inversion indicate that σ1 (SHmax) and σ3 (SHmin) are generally sub-horizontal and σ2 is sub-vertical in all the previous stress tensors, which are belonging to the strike-slip system with σ1 swinging around NW-SE to WNW- ESE direction within a range of 15 degrees (113- 128). These stress tensors are mainly responsible for the conjugated NW sinistral with E–W dextral, N–S to NNW sinistral with ENE to E–W dextral strike-slip faults in the study area at the later stage of deformation (Figs 6-10).

Table 1. Shows the results of the reduced paleo stress tensors obtained from the fault-slip data.

Station. No	N	R	R'	Principal Stress axis			Tensor type	SHmax
				σ1	σ2	σ3		
1	10	0.25	1.75	25/293	65/100	05/201	Pure strike-slip	113
2	9	0.56	1.44	04/293	80/179	09/024	Pure strike-slip	113
3	25	0.54	1.46	11/300	67/182	20/034	Pure strike-slip	120
4	9	0.67	1.33	23/308	62/162	14/044	Pure strike-slip	128
5	22	0.45	1.55	02/123	85/236	04/033	Pure strike-slip	123

N= net data number representing the tensor.
R= (σ2- σ3)/ (σ1- σ3).
R'= tensor type index.
σ1, σ2, σ3 = plunge, and azimuth of principal stress axes.
SHmax= maximum horizontal compressive stress.

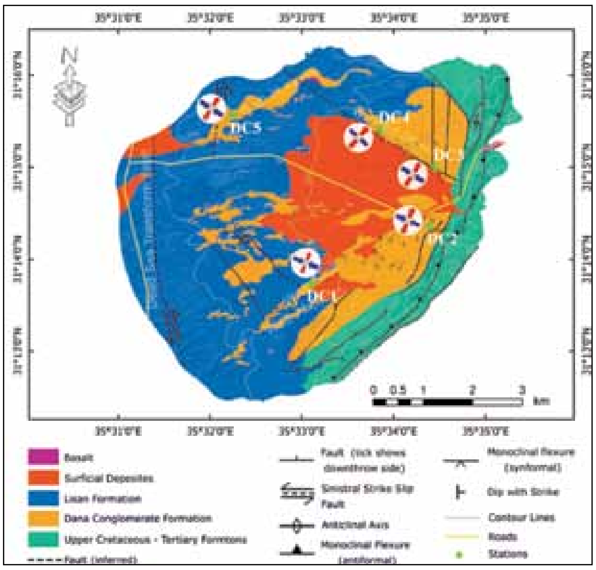

Figure 11. Results of the stress inversion are represented as SHmax (blue arrows) and SHmin (red arrows) in the study area displayed on the geological map.

The stress tensors of the study area revealed an anti-clockwise rotation of 10-20 degrees for σ1 (SHmax) compared with the Dead Sea stress field (Figure. 12).

Stress inversion results in the study area also reveal slight differences in the direction of the principal stresses between some stations. This reflects the stress changes due to the position along the main faults and to block rotation, or they may also be due to stress changes in time. So, the stress state at any point along the main faults is the superposition of the regional tectonic stresses, which are generally uniform over relatively large areas (compared to the length of the faults) for a distinct tectonic event and a distinct stress field. The local fault-related stresses are affected by the displacement along the main faults and depend upon the position around them (Diabat, 2007).

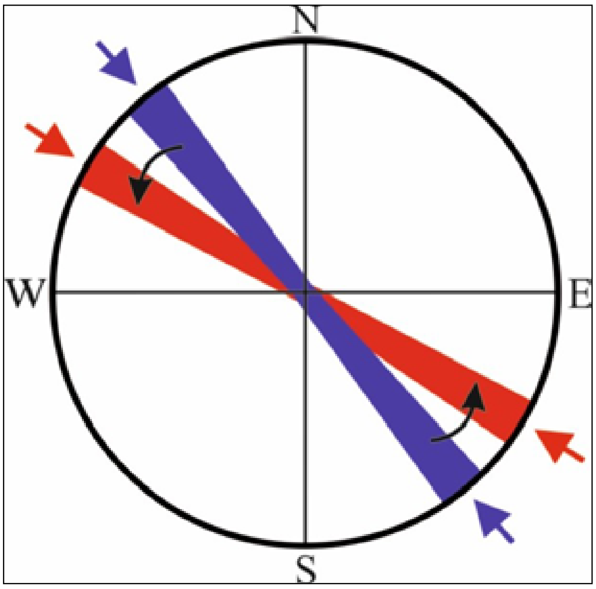

Figure 12. Directional model showing an anti-clockwise rotation of the maximum horizontal compression (SHmax); Dead Sea stress (blue), study area stress (red).

6. Conclusions

The current research has pointed out and elaborated on the state of paleo stress in the Ed Dhira area east of the Dead Sea. The results have shown that σ1 (SHmax) and σ3 (Shmin) are usually sub-horizontal and σ2 is sub-vertical in all stations, which are belonging to a major strike-slip system with σ1 SHmax swinging around the NW-SE to WNW-ESE direction. This revealed an anti-clockwise rotation of 10°-20°for σ1 (SHmax) compared with the Dead Sea stress field. The stress tensors are responsible for the formation of N–S to NNW–SSE sinistral strike-slip faults (e.g., DC1, DC2, and DC4), as well as the formation of conjugated NNW–SSE sinistral strike-slip faults with dextral E–W to ENE–WSW (e. g., DC3, and DC5) in the studied area.

References

Al- Adamat, M. and Diabat, A. (2021). Syndepositional extensional structures in Oligo–Pliocene Dana Conglomerate Formation at Ed Dhira area (Dead Sea, Jordan). Arabian Journal of Geosciences. 14: 309. https://doi.org/10.1007/s12517-021-06666-7.

Angelier, J. (1989). From orientation to magnitudes in paleostress determinations using fault slip data. Journal of Structural Geology, 11 (1–2): 37–50. https://doi.org/10.1016/0191-8141(89)90034-5.

Atallah, M. (1992). Tectonic evolution of northern Wadi Araba, Jordan. Tectonophysics, 204(1-2): 17– 26. https://doi.org/10.1016/0040-1951(92)90266-9.

Atallah, M., and Al-Taj, M. (2004). Active surface ruptures of the Dead Sea Transform in Wadi Araba, Jordan. Dirasat, series B: Pure Sciences, 31(1): 59 – 81.

Bender, F. (1974). Geology of Jordan. Bontrager, Berlin

Bott, M. H. P. (1959). The Mechanics of Oblique Slip Faulting. Geological Magazine, 96(2): 109 –117. https://doi.org/10.1017/S0016756800059987.

Delvaux, D. (2012). Release of program Win-Tensor 4.0 for tectonic stress inversion: statistical expression of stress parameters. In: Geophysical research abstracts,14. EGU General Assembly Vienna.

Delvaux, D. and Sperner, B. (2003). New aspects of tectonic stress inversion with reference to the TENSOR program. In: Nieuwland, D. A. (Ed). New Insights into Structural Interpretation and Modelling. Special Publications, Geological Society, London. Pp.75 –100.

Delvaux, D., Moeys, R., Stapel, G., Petit, C., Levi, K., Miroshnichenko, A., and San'kov, V. (1997). Paleostress reconstructions and geodynamics of the Baikal region, Central Asia, Part 2. Cenozoic rifting. Tectonophysics, 282(1-4): 1–38. https://doi.org/10.1016/S0040-1951(97)00210-2.

Diabat, A. A. (2007). Paleostress analysis of the Cretaceous-Tertiary rocks in central Jordan. Dirasat, Pure Sciences, 34(2):192–200.

Diabat, A., and Masri, A. (2005). Orientation of the principal stresses along the Zerqa-Ma'in Fault. Mu'tah Lil-Buhuth wad-Dirasat, 20(1): 57–71.

Fossen, H. (2016). Structural geology. 2nd Ed., Cambridge Univ. Press, Cambridge.

Garfunkel, Z. (1981). Internal structure of the Dead Sea leaky transform (rift) in relation to plate kinematics. Tectonophysics, 80(1–4): 81–108. https://doi.org/10.1016/0040-1951(81)90143-8.

Garfunkel, Z., Zak, I. and Freund, R. (1981). Active faulting in the Dead Sea rift. Tectonophysics, 80(1–4):1-26. https://doi.org/10.1016/0040-1951(81)90139-6

Hardy, C., Homberg, C., Eyal, Y., Barrier, É., and Müller, C. (2010). Tectonic evolution of the southern Levant margin since

Mesozoic. Tectonophysics, 494(3 – 4):211–225. https://doi.org/10.1016/j.tecto.2010.09.007.

Igwe, O., and Okonkwo, I. A. (2016). Application of paleostress analysis for the identification of potential instability precursors within the Benue Trough Nigeria. Geoenvironmental Disasters, 3(1): 1-15. https://doi.org/10.1186/s40677-016-0051-z

Khalil, B. (1992). The geology of Ar Rabba area, scale 1: 50,000, sheet no. 3152– I. Natural Resources Authority, Amman, Jordan.

Klinger, Y., Avouac, J. P., Dorbath, L., Karaki, N. A., and Tisnerat, N. (2000). Seismic behaviour of the Dead Sea fault along Araba valley, Jordan. Geophysical Journal International, 142(3): 769–782. https://doi.org/10.1046/j.1365-246x.2000.00166.x.

Kohn, B., Weissbrod, T., Chung, L., Farley, K., and Bodorkos, S. (2019). Low-temperature thermochronology of francolite: Insights into timing of Dead Sea Transform motion. Terra Nova, 31(3): 205–219. https://doi.org/10.1111/ter.12387.

Masri, I. A. (1997). The tectonic evolution of Ed Dhira Monocline-east of the Dead Sea. In Terra Nostra. Proceeding's 13th GIF Meeting on The Dead Sea rift as a Unique Global Site. Dead Sea, Israel.

Masson, F., Hamiel, Y., Agnon, A., Klinger, Y., and Deprez, A. (2015). Variable behavior of the Dead Sea Fault along the southern Arava segment from GPS measurements. Comptes Rendus Geoscience, 347(4):161–169. https://doi.org/10.1016/j.crte.2014.11.001.

Powell, J. H. (1988). The geology of the Karak area, scale 1: 50,000, sheet no. 3152– III. Natural Resources Authority, Amman, Jordan.

Radaideh, O. M., and Melichar, R. (2015). Tectonic paleostress fields in the southwestern part of Jordan: New insights from the fault slip data in the southeastern flank of the Dead Sea Fault Zone. Tectonics, 34(9):1863–1891. https://doi.org/10.1002/2015TC003919.

Simón, J. L. (2019). Forty years of paleostress analysis: has it attained maturity? Journal of Structural Geology, 125: 124–133. https://doi.org/10.1016/j.jsg.2018.02.011.

Wallace, R. E. (1951). The geometry of shearing stress and relation to faulting. The Journal of Geology, 59(2): 118– 130. https://doi.org/10.1086/625831.

Weinstein, Y., Nuriel, P., Inbar, M., Jicha, B. R., and Weinberger, R. (2020). The impact of the Dead Sea transforms kinematics on adjacent volcanic activity. Tectonics, 39(1): e2019TC005645. https://doi.org/10.1029/2019TC005645.

Yamaji, A. (2007). An Introduction to Tectonophysics: Theoretical Aspects of Structural Geology. Terrapub, Tokyo.

Zoback, M. L. (1992). First-and second-order patterns of stress in the lithosphere: The World Stress Map Project. Journal of Geophysical Research: Solid Earth, 97(B8): 11703–11728. https://doi.org/10.1029/92JB00132.

JJEES

Jordan Journal of Earth and Environmental Sciences

JJEES (2022) 13 (4): 286-297
ISSN 1995-6681

Assessment of Subsoil Suitability for Shallow Foundation Design at Part of Ibadan Area, Southwestern Nigeria, using Geophysical and Geotechnical Techniques

[1]Obini N., [2]Egware E. Abel, [3]Ekinne A. Olalekan, [4]Omietimi, J. Erepamo

[1]*Department of Geology, Federal University of Technology Owerri, Imo State, P.M.B 1526*
[2]*Department of Geology, University of Ibadan-Ibadan, Oyo State, P.M.B. 200285*
[3]*Department of Earth Sciences, Ajayi Crowther University, Oyo, Oyo State, 1066*
[4]*Department of Geology, University of Pretoria, South-Africa*

Received 15th October 2021; Accepted 12th May 2022

Abstract

In the present study, geophysical and geotechnical techniques were applied to investigate the suitability of the subsoil for foundation design in part of Ibadan, Southwestern Nigeria. Vertical electrical resistivity and cone penetration tests were performed at seven points, and two samples each at 0.5 m (disturbed) and 1.5 m (undisturbed) were randomly collected at five (5) locations within the site. Three geo-electric layers exhibiting H-type curve patterns were observed for the VES sections: top soil (89.10-253.80 m, 1.38 m), weathered basement (24.00-50.10 m, 8.62 m), and fractured/fresh basement (190.80-585.00 m, depth-rock head = 9.84 m). Based on their average resistivities, these layers were classified as moderately competent, incompetent, and competent. CPT data shows allowable bearing capacity, qa (190.89-594.00 KN/m^2), allowable bearing pressure, ABP (63.63-198.00 KN/m^2), and ultimate bearing capacity, qu (212.10-660.00 KN/m^2) >100 KN/m^2 between 8.0-1.4 m where clayey-sand dominates would serve well as foundation bases. Gradation test (GT) analysis shows that >35% of particles pass sieve #200 at 0.5 m, while average Liquid limit, Plasticity limit, Plasticity Index, and Natural moisture content are 34.2%, 15.0%, 19.0%, and 9.6%, respectively, indicating low plasticity and compressibility soils classified as low liquid limit clay (CL) and A-7 (A-7-6 and A-7-5) soils according to the Unified Soil Classification System and Association of American State and Highway Transport Official. Additionally, samples taken at 1.5 m depth exhibited an average bulk density of 2.10 Mg/m^3, compatible with materials that have osmotic swelling capabilities. Cohesion (C) and angle of internal friction (ϕ) averaged 72.6 KN/m^2 and 18.8°, respectively, indicating good shear strengths. Finally, under increasing pressures (50-100, 100-200, and 200-300 KN/m^2), the coefficient of volume compressibility and coefficient of consolidation stay reasonably constant, indicating a material with low to moderate deformation on loading.

Keywords: *VES, CPT, Foundation, Shear strengths, Consistency Limits, Ibadan, Southwestern Nigeria.*

1. Introduction

Foundation failure is one of the underlying causes of building collapses, implying that the major cause of foundation failures is a lack of awareness of the subterranean condition (Abam, 2018). Civil building failure has been a recurring problem in today's world, particularly in coastal areas where fine-grained soil aggregates in contact with groundwater bodies dominate the supporting grounds (foundation materials). Uncertainties related to structural design and planning, on the other hand, play a part in such failures. Unknown soil properties are among the most important design uncertainties (Bremmer, 1999), but others, such as the non-linear behavior of soil under stress, the difficulty of estimating soil properties in undisturbed or in-situ conditions, and high spatial variation, all add to the problem. To perform optimally, a foundation must be safe from overall shear failure in the soil that supports it and not experience excessive settlement in comparison to the proposed structure's tolerance. This necessitates pre-foundation studies with suitable safety factors before foundation design to minimize structural lapses in terms of loss of life, litigation, and/or property destruction.

Structures in civil engineering interact with the ground, and some are made of earth-derived materials (Imeokparia and Falowo, 2019). Soil and rocks are still widely used in foundations, dams, and embankments in their natural state. For structures such as foundations, roadways, and tunnels, soil-structure interaction must be studied; for earth structures such as earth dams and slopes, good concepts must be developed on which to base studies (Atkinson, 1993; Imeokparia and Falowo, 2019). One of the most essential difficulties in foundation engineering, for example, is determining bearing capacity and behavior under stress. Although a country's building code stipulates the maximum allowable settlement for a certain structure, differential settlement is nonetheless possible.

The structural requirements, subsurface conditions, site characteristics, and economics are all analyzed and determined when selecting a foundation (Imeokparia and Falowo, 2019). A solely geotechnical investigation will not be able to generate a sufficient dataset to adequately define foundation soils. When the geology is complicated, this is frequently the case. To develop a reliable subterranean model for a proposed building site, a rigorous step-by-step strategy

* Corresponding author e-mail: obininnamdi@gmail.com

of subsurface exploration comprising the integration of geophysical and geotechnical techniques is necessary.

Direct measurements of soil parameters, either in situ or on soil samples in the laboratory, are used in geotechnical site evaluations. The most often utilized dynamic and static in-situ penetration tests in geo-engineering investigations (Baldi et al., 1995) are the standard penetration test (SPT) and cone penetration test (CPT), which are usually followed by the determination of soil physical parameters. Geophysical methods, on the other hand, are low-cost and quick to implement (Savvaidis et al., 1999; Luna and Jadi, 2000; Venkateswara, 2004; Olorunfemi et al., 2005; Soupios et al., 2005; Aizebeokhai et al., 2017; Oyeyemi, et al., 2015a; Imeokparia and Falowo, 2019; Oyeyemi et al., 2020).

Such integration of subsoil geotechnical and geophysical investigation exercises is required to have adequate knowledge of the engineering properties of subsoil materials that would have direct interaction with the proposed structure in the study area (Oke et al., 2009), especially in areas with complex geology that can result in inhomogeneity in foundation soils and rocks, which a purely geotechnical approach cannot provide (Oke et al., 2009). As a result, the goal of this work is to define the subsurface geological sequences/structures, as well as their resistivities, geotechnical characteristics, and overall site integrity for a building project. Findings from this study will aid in making informed decisions about the depth and type of foundation that should be used on the site to avoid possible failure, loss of life, and environmental damage.

2. Geology and Description of the Study Area

The study area is bounded between latitude 7° 26' 30.9'' N to 7° 27' 15'' N and longitude 3° 55' 08'' E to 3° 56' 10.1'' E located within the Basement Complex (BC) of southwestern Nigeria, composed of four main lithological units (Anifowose and Borode, 2007; Ayodele, 2015). These units (Fig.1) include; quartzite, quartz-schist of the meta-sedimentary series, the migmatites complex (banded gneiss, augen gneisses, and granite-gneiss), and variably migmatized biotite-hornblende gneiss with intruded pegmatites, quartz veins, aplites and dolerite dykes (Burke et al., 1976). Structural discontinuities run perpendicular and across the general rock foliation (NNE-SSW), characterizing the basement rocks. Some of these fractures are filled with dark-grey, unmetamorphosed amphibolitic dykes or quartzitic and quartzo-feldspathic intrusions. The subsurface succession of a typical weathered profile (topsoil, lateritic soil, saprolitic horizon, sap-rock/fractured basement, and fresh basement) in Ibadan agrees with a typical Basement Complex environment (Olayinka and Yaramanci, 1999; Tijani et al., 2009).

In basement complex terrains, the occurrence of groundwater depends on thick weathered overburden and deeply fractured zones. Such weathered overburden provides high storativity while the fractures account for their high permeability (Guiheneuf et al., 2014). However, hydraulic permeability is likely to be low when the regolith is derived from rocks rich in ferromagnesian minerals, notably biotites and feldspars which convert quickly to hydrobiotite and clays, producing low permeability regolith (Graham et al., 2010). Locally, the study site is underlain by banded gneiss (Fig.1) and can host the groundwater in an unconfined condition; otherwise, they are semi-confined to confined conditions (Olayinka and Yaramanci, 1999).

The area with its characteristic rainforest vegetation exhibits a typical tropical climate of averagely high temperature, high relative humidity, and generally two rainfall maxima regimes during the rainfall period of March to October. The dry season extends from November to February, while the rainy season extends from March to October (Oyinloye and Modebola-Fadimine, 2013). The mean temperature is highest at the end of the Harmattan (averaging 28°C), from the middle of January to the onset of the rains in the middle of March (Iloeje, 1981).

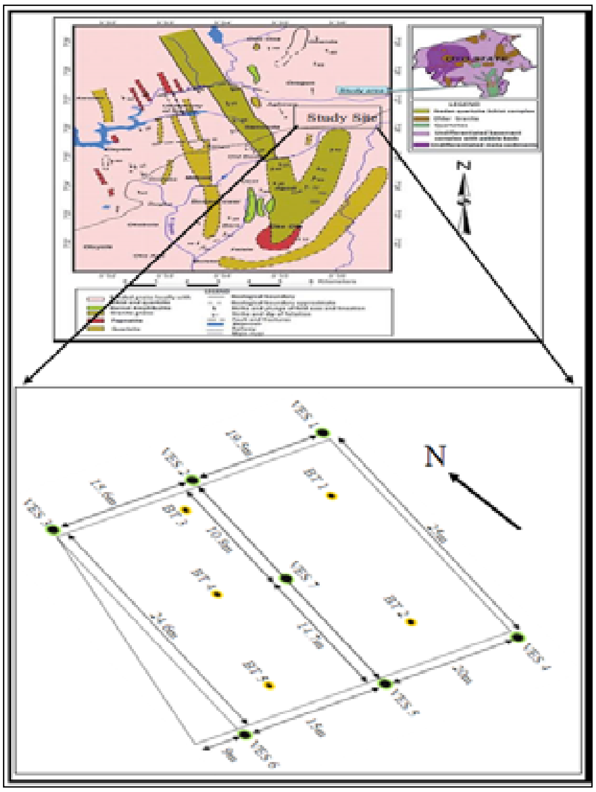

Figure 1. Geological Map *(Amanambu, 2015)* and Site Sketch showing VES/CPT and Sampling Points.

3. Data Acquisition and Analysis

3.1 Geophysical Survey

Earth materials' in-situ qualities and structural traits can be measured with surface geophysical methods (Lowrie, 2007). By reducing design uncertainty and lowering inquiry expenses, such strategies have demonstrated cost efficiencies (Willian, 2010).

The Allied Omega geophysical Terrameter was used to probe seven (7) vertical electrical sounding (VES) stations (Fig.1) in conjunction with the cone penetrometer test (CPT) stations. The Schlumberger array (Fig. 2) was adopted, with maximum AB/2 = 80 m and MN/2 = 5 m however, MN≤1/5AB was maintained as the geometric relationship between MN and AB. On bi-logarithmic graph sheets, the measured apparent resistivities, ρa, were plotted against AB/2 on ordinate and abscissa respectively. To obtain the layer parameters, ρa was first manually processed and quantitatively analyzed using a partial curve matching technique. To obtain the layered apparent resistivity and estimated thickness, the resultant curves were interpreted qualitatively through a visual examination and quantitatively through a partial curve matching technique using Win-RESIST software (Vander-Velpen, 2004).

Furthermore, interpretation was done keeping in mind the ideal depth of investigation equal to one-third (1/3) of the current electrode spacing at the inflection point (Tijani et al., 2021). Finally, geoelectric sections were constructed from the generated layer parameters for in-depth characterization of the subsurface environment and correlation.

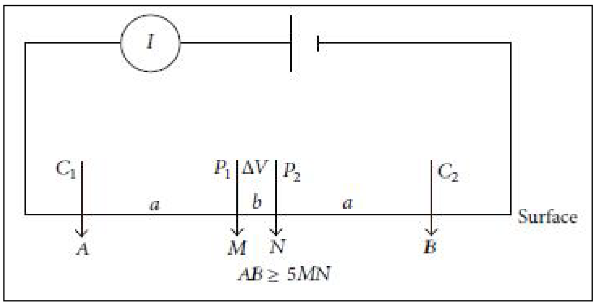

Figure 2. Schematic display of the Schlumberger electrode arrangement

3.2 Cone Penetration Test (CPT)

CPT is a quasi-static penetration test that uses a 60 % steel cone to determine the ground's penetration resistance at a specific point. A ten (10) ton capacity testing machine was deployed here. A cylindrical probe with a cross-sectional area of 1000 mm^2 and a conic head with a 60^o apex angle make up the equipment. The test was conducted by anchoring the winch frame to the earth, providing the necessary power to push the cone into the earth (Coerts, 1966). By exerting pressure on the outer sounding tube, the probe is pushed down into the earth at a continuous pace of around 2 cm/s in the closed position. At the same time, the penetration resistance is measured at predetermined intervals from the existing ground level down to refusal depths. Resistance to the penetration of the cone registered on the pressure gauge connected to the pressure capsule is recorded. The tube is then pushed down, and the procedure described above is repeated. Tests are usually terminated when dense sands or rock unit is encountered or when there is an excessive vertical misalignment, and the support anchors of the machine lift off the ground. Equation (1) which covers all foundations irrespective of the width according to Meyerhof (1974) was adopted for the estimation of allowable bearing capacity from the cone tip resistance value, qc:

$q_a = 2.7\ q_c$ (KN/m^2) …………………………………………. (1)

Where; q_a is the allowable bearing capacity;

And qc is the cone penetration resistance value.

The allowable bearing pressure (ABP) was calculated by multiplying the factor of safety (equal 3) on the allowable bearing capacity, while the ultimate bearing capacity (qu) was calculated by multiplying the allowable bearing capacity by three (3) (Skempton and MacDonald, 1956). Using Microsoft Office Excel 2010, a resistance profile was created by plotting successive cone resistance readings against depth. The inflection points of the obtained penetrometer curves were interpreted as the boundary between the distinct lithologies, whereas layer sequences were interpreted from variations in cone tip resistance with depth.

The results of the geophysical surveys were used to choose the CPT points/locations. VES and CPT were followed by a random collection of two samples per pit at 0.5 m (disturbed) and 1.5 m (undisturbed) depths for five (5) sampling points to ensure a thorough exploration of the study site (Fig.1). Manual sampling was carried out with a pick axe and shovel, as well as a sealable polyethylene bag (for disturbed samples) and PVC pipe measuring 76 mm x 38 mm (undisturbed samples).

The water level was not monitored because no groundwater was intercepted. The sampling process and specification outlined by British Standard Institute (BSI 1377, 1990) for geotechnical soil sampling were properly followed. All sampling took place between January and February, during the dry season.

3.3 Geotechnical Laboratory Tests (GLT)

The soil samples were subjected to the following laboratory tests: consistency limits (liquid limit, LL; plastic limit, PL; and plasticity index, PI), grain size distribution (dry sieving) analysis, unit weight determination (bulk density, γB), moisture content, the undrained triaxial test was performed to compute shear strength parameters (angle of internal friction, ϕ; and cohesion, C) of the soil samples were obtained from the relationship between the principal stresses at failure. At 50-100 KN/m^2, 100-200 KN/m^2, and 200-300 KN/m^2 stress ranges, an Oedometer consolidation test was performed to measure the coefficient of volume compressibility, Mv; and coefficient of consolidation, Cv for settlement characteristics. These tests were carried out adhering to the British Standard Institution 1377 (1990) for testing material used for all laboratory tests.

4. Results and Discussion

Table 1 summarizes the findings of an interpreted geophysical research, whereas tables 4 and 5 indicate theoretically estimated levels of bearing capacity based on cone resistance, qc values, and geotechnical data, respectively.

4.1 Geophysical Studies

Table 1 depicts the subsurface lithology it penetrates (Sattar *et al*., 2004), with small differences expected in a normal geophysical result (Tijani et al., 2021). Three subsurface layers (top soils, weathered basements, and fractured/fresh basements) with distinct H-curve patterns were shown by VES curves (Fig.3). Top soil revealed relatively high resistivity materials (89.10-253.80 Ωm), indicating reworked/artificially compacted top soils, whereas the weathered basement revealed low resistivities (24.00-50.10 Ωm), indicating a very saturated medium composed of clay materials (Arora, 2008), potentially linked to poor drainage conditions (Giza and Igwe, 2018). Resistivity values in the fractured/fresh basement ranged from 190.80

to 585.00 Ωm. The first layers (top soil) are slightly thicker than 1.0 m for VES 2 and 4 (Table 1), and primarily consist of clay, sandy clay, and lateritic lithologies whose constituent minerals (silicates, feldspar, micas, iron, and aluminum) may not readily favour foundation founding due to expansion (seasonal volume fluctuations). Except where an appreciable thickness of lateritic materials is encountered, basic ground improvement by ripping off and backfilling with a more admixture of granulated and cohesive materials to aid drainage and increase shear strength is required to erect structures on/within the first layers. Laterites are rich in iron and aluminum, and thus are firm and physically resistant (Hill et al., 2000; Agada et al., 2017). Furthermore, the weathered basement or saprolitic horizon, which has an average thickness of 8.62 m, may not serve well because it may exacerbate excessive pore pressure development caused by poor drainage, resulting in significant effective stress decreases and foundation instability in the study site. A typical depth-rock head in the range of 6.7-13.9 m was discovered for the fractured/fresh basement (ave. 9.84 m). Therefore, based on their average resistivities, top soils (163.68 Ωm) are fairly competent, weathered units are incompetent (35.49 Ωm), and fresh/fractured basements are competent (378.00 Ωm) as per Sherrif (1991) classification for foundation materials (Table 2).

The topsoil is relatively competent but very thin (Fig.4a and b), which is consistent with a previous study in Akure Metropolis by Ojo et al., (2015), which found topsoil thickness ranging from 0.3 to 5.2 m and resistivity of 15.0-7,133 Ωm. Although the thickness of the soil layer, among other things, affects bearing capacity (Mosallanezhad and Moayedi, 2017), the measured mean thickness (8.6 m) of the overburdened/weathered soil on the basement will nevertheless help to distribute the foundation load evenly.

4.1.1 Evaluation of Soil Corrosivity

Electrical current-carrying materials used in civil engineering projects, whether at the beginning or end, are prone to deterioration, necessitating proper soil assessments to minimize corrosion. Soil corrosivity in the research site range from "moderately" to "slightly" to "practically non-corrosive" (Oladapo et al., 2004; Mosura et al., 2017), (Table 3). Table 3 shows that the second geoelectric layers of VES 1-7 have a moderately corrosive potential, whereas VES 4-7 has a slightly corrosive rating associated with its first geoelectric layer, and a non-corrosivity potential is attributed to the third geoelectric layers linked to VES 1-7, except for VES 1 and 2, which have non-corrosivity potentials associated with the first (1) and second (2) geoelectric layers, respectively.

Table 1. Geoelectrical layer properties and inferred lithological units

VES No.	Resistivity (ohm-m)	Layer Parameters		Layers	Curve Type	Inferred Lithology
		Thickness (m)	Depth (m)			
1	298.00	1.70	1.70	1	H	Top soil
	27.40	5.00	6.70	2		Weathered basement
	190.80	-	-	3		Fractured/Fresh basement
2	253.80	0.70	0.70	1	H	Top soil
	50.00	7.00	7.70	2		Weathered basement
	268.00	-	-	3		Fresh/fractured basement
3	205.70	1.00	1.00	1	H	Top soil
	50.10	6.10	7.10	2		Weathered basement
	306.00	-	-	3		Fractured/Fresh basement
4	149.70	0.60	0.60	1	H	Top soil
	24.00	8.70	9.30	2		Weathered basement
	466.90	-	-	3		Fractured/Fresh basement
5	117.80	1.50	1.50	1	H	Top soil
	34.60	9.90	11.90	2		Weathered basement
	343.90	-	-	3		Fractured/Fresh basement
6	89.10	1.80	1.80	1	H	Top soil
	30.30	12.10	13.90	2		Weathered basement
	487.30	-	-	3		Fractured/Fresh basement
7	166.00	1.70	1.70	1	H	Top soil
	32.00	11.60	12.30	2		Weathered basement
	585.00	-	-	3		Fractured/Fresh basement

The corrosivity potentials of the soils in the site differ among the various geoelectric layers, making metallic pipes buried inside the slightly (second layers) to moderately (first layers) corrosive layers more sensitive to corrosion and eventual failure. As a result, underground metal storage tanks galvanized pipes, and steel pipes can be buried at the third layer (>180 Ω m) without the risk of possible chemical corrosion, as metal or steel structures within this layer are mostly unaffected by corrosion.

Clay materials have low electrical resistivity and great electrical conductivity, with resistivity values ranging from

1 to 100 Ωm. At 1-6 m depth below the surface within which the electrical materials could be earthed have resistivity values ranging from 27.40-50.10 Ωm (Table 1). These clayey soils are a good medium for earthen depth to absorb any excess charge.

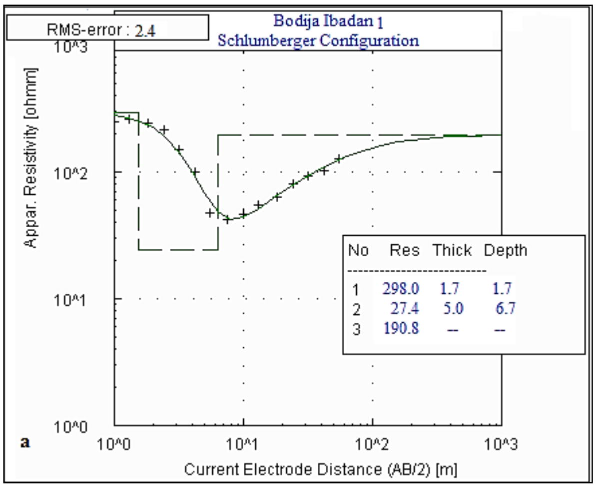

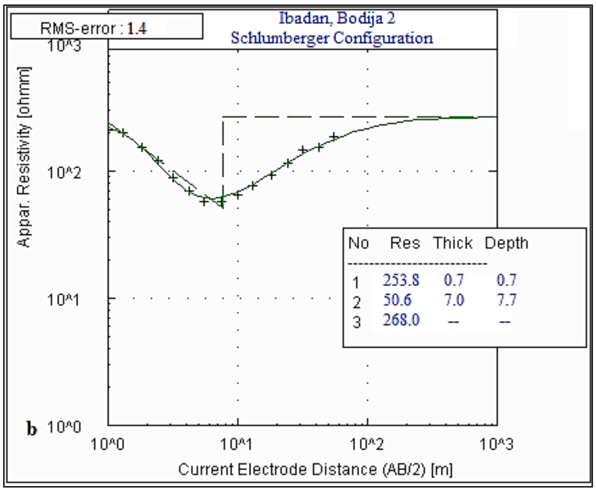

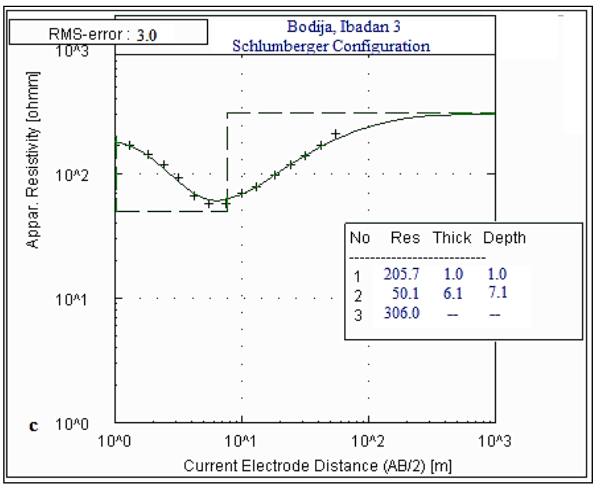

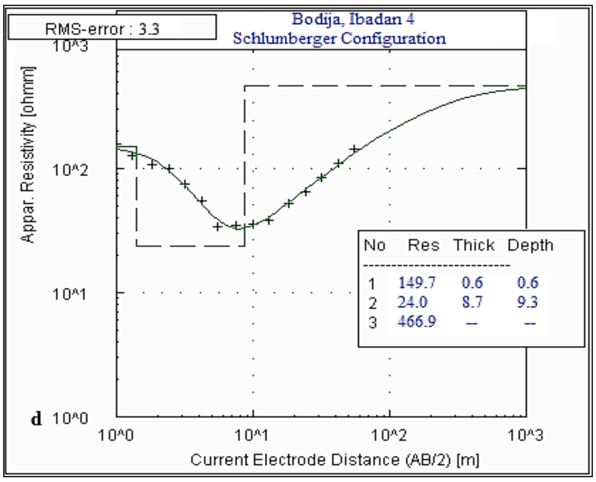

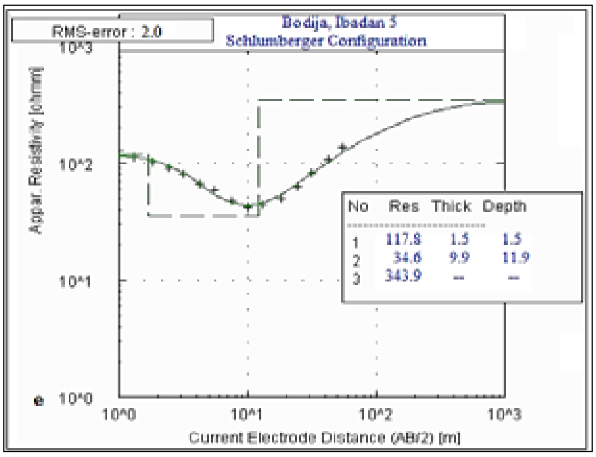

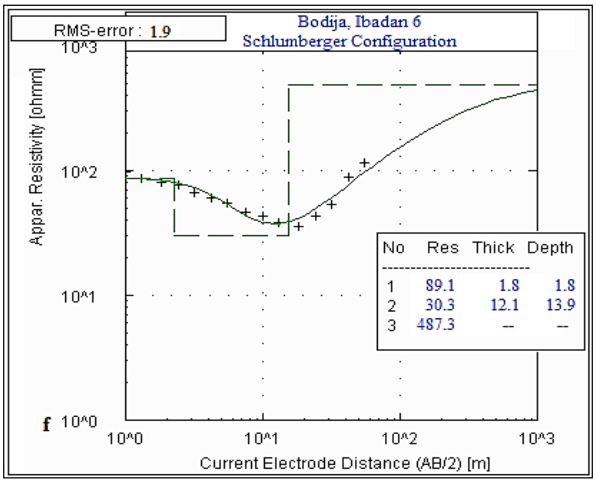

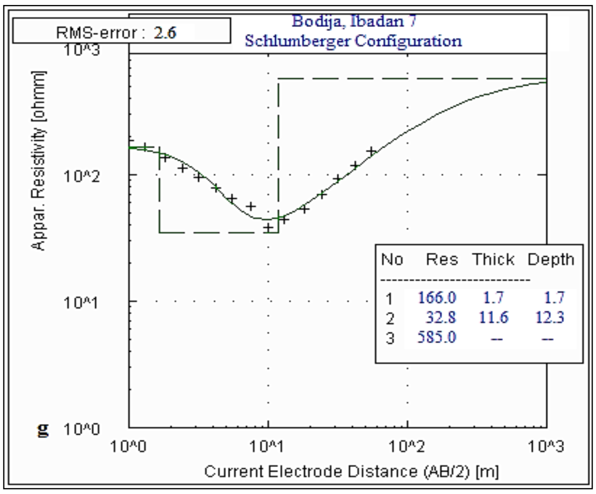

Figure 3. a-g. Inverted VES models associated with their RMS error for the Investigated points

4.2 Cone Penetration Test (CPT) and Geotechnical Studies

4.2.1 Cone Penetrometer Test (CPT)

The cone penetrometer test is a simple, accurate, and quick way of measuring various degrees of bearing capacity, stratigraphic correlation, and soil deformation characteristics. A further inspection of the displayed CPT data revealed outlines/curves that corresponded to three to four geologic layers (Fig.5a-g).

Table 1. Lithologic competence rating in terms of apparent values (Sherrif, 1991)

ρ_a rating (Ωm)	Lithology	Competence rating
<100	Clay	Incompetent
100- 350	Sandy clay	Moderately competent
350-750	Clayey sand	Competent
>750	Sand/laterite/bedrock	Highly competent

Here, Fig.5a depicts a subsurface environment with clay materials at the surface (0.0-0.2 m), clay/silty clay at 0.2-0.4 m, sandy clay with a thickness of 0.18 m (0.4-0.58 m), and clayey sand material at 0.6 m down to the refusal depth (1.0 m).

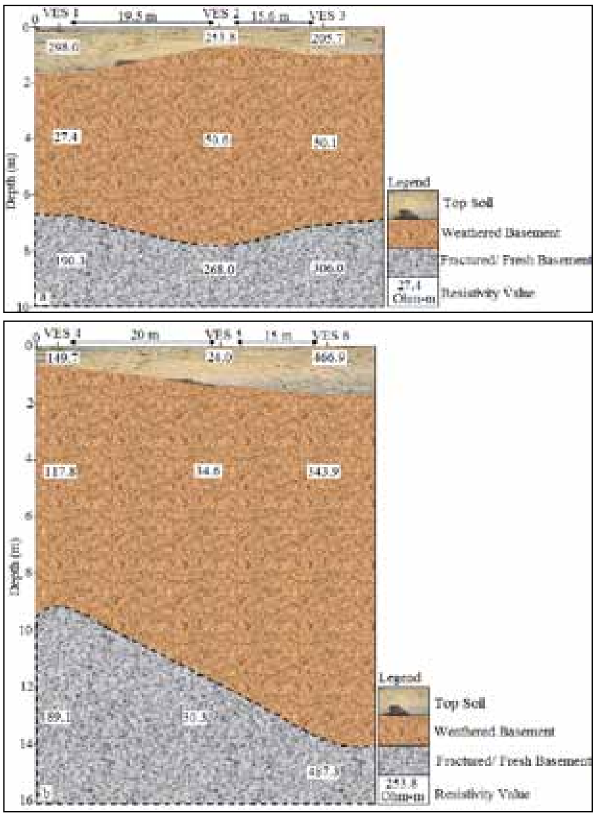

Figure 4. Constructed Geoelectric Sections of the Study Site

Table 3. Soil Corrosivity Ratings According to Oladapo et al., (2004) and Mosura et al., (2017)

S/N	Soil Resistivity Range (Ωm)	Soil Corrosivity	VES Points	Geoelectric Layers
1	<10	Very Strongly	Nil	-
2	10-60	Moderate	1, 2.3, 4, 5, 6, and 7	2, 2, 2, 2, 2, 2 and 2
3	60-180	Slightly	4, 5, 6 and 7	1, 1, 1, 1
4	>180above	Practically noncorrosive	1, 2, 3, 4, 5, 6 and 7	1 and 2, 3, 3, 3, 3, 3

Table 4. Theoretically Estimated levels of Bearing Capacities from Cone Tip Resistance, qc

S/N	Depth (m)	Average qc (kg/cm^2)	Average q_a (KN/m^2)	Average ABP (KN/m^2)	Average q_u (KN/m^2)
1	0.00	0.00	0.00	0.00	0.00
2	-0.20	26.40	71.28	23.76	79.20
3	-0.40	33.50	90.45	30.15	100.5
4	-0.60	59.30	160.11	53.37	177.90
5	-0.80	70.70	190.89	63.63	212.10
6	-1.00	157.10	424.17	141.39	471.30
7	-1.20	148.30	400.00	133.47	444.90
8	-1.40	220.00	594.00	198.00	660.00

q_c = cone tip resistance, q_a=allowable bearing capacity, ABP= allowable bearing pressure, q_u=ultimate bearing capacity, and factor of safety = 3

At 1 m, clayey sand lithology is competent and would be suitable for laying a shallow foundation. Similarly, CPT 2 revealed clay/silt clay material at 0-0.2 m, clay-silt with 0.6 m thickness at 0.2-0.4 m, sandy clay at 0.4-1.0 m, and clayey sand material with a thickness of 0.4 m at 0.4 to maximum depth (1.4 m), all of which could support shallow foundations within the site. The CPT curve in Fig.5c indicated three geologic layers: clay/clay silt at 0-0.4 m, clayey silt at 0.4-0.6 m, and sandy clay and clayey sand at 0.6-0.8 m and 0.8-1.2 m, respectively, which support the results of other CPTs. The fourth (4th) CPT point (Fig.5d) revealed a 0.2 m thick clay top soil, followed by silty clay in the range of 0.2-0.8 m, sandy clay at 0.8-1.0 m, and clayey sand at 1.0-1.4 m below the surface. Similarly, CPT 5 exhibits a four-layer zonation, with clay/silty clay at 0-0.4 m, clay silt at 0.4-0.6 m, sandy clay at 0.6-1.0 m, and the last horizon (clayey sand material) with a thickness of 0.4 m lying at 1.0-1.2 m deep (Fig.5e). Further analysis found that CPT 6 has a subsurface soil profile defined by silt/silty clay top soil, sandy clay, and sand/clayey sand lithologies below the surface in the range of 0-0.2 m, 0.2-0.4 m, and 0.4-1.4 m, respectively (Fig.5f). Figure 5g (CPT 7) showed a subsurface soil profile with clay at a depth of 0-0.2 m, silty clay at 0.2-0.8 m, sandy clay at 0.8-1.0 m, and clayey sand at 1.0-1.4 m.

Although, except CPT 3, which was characterized by three sequences, the CPT results were associated with low to high allowable bearing capacities (71.3-594.0 KN/m^2), allowable bearing pressures (23.8-198.0 KN/m^2), and ultimate bearing capacities (79.2-660 KN/m^2) according to Bell (2007), revealing appropriate founding depths and supporting bases/ media for shallow foundations in the study site (Table 4). The allowable bearing capacities, allowable bearing pressures, and ultimate bearing capacities estimated at various depths (Table 4) corresponded to material strengths at such depths, such that ground penetration resistance decreases (<100 kg/cm^2) near the surface (0-0.8 m), but increases significantly (100 kg/cm^2-200 kg/cm^2) beyond 0.8 m where targeted CPT values exist. The allowable bearing capacities, allowable bearing pressures, and ultimate bearing capacities estimated at various depths (Table 4) corresponded with material strengths at such depths, such that ground penetration resistance decreases (100 kg/cm2) near the surface between 0-0.8 m, but increases significantly (100 kg/cm^2-200 kg/cm^2) beyond 0.8 m where targeted CPT values exist. The consequence is that where competent materials are available, foundations in the research site can be securely built beyond 0.8 m. Because there is no near-surface groundwater table, this is advantageous. As a result, the depth of footings subject to 25 mm total settlement as a frequently accepted basis for designs (Bell, 2007) should be at least 0.8 m below the surface.

4.2.2 Geotechnical Studies

The determination of a soil's physical property aids in the identification and classification of soils. Because particle size and distribution of pores within a soil matrix considerably influence soil stability (Bidyashwari et al., 2017) the particle size distribution of soil is an important predictor of its geotechnical features (Falowo, 2018). Table 5 shows that the proportions of particles passing sieves No. 4 (4.76 mm), 6 (3.36 mm), and 200 (0.075 mm) vary as 40.0-47.0, 13.0-25.0, 71.0-84.0, with average values of 44.0 %, 20.0 %, and 80.0 %, indicating high clayey material greater than 35 % recommended by British Standard (1990) as foundation support.

The soil's consistency limits in terms of Liquid limit, LL, Plastic limit, PL, and Plasticity index, PI, vary from 30.0-37.0, 12.0-17.0 %, and 17.0-21.0 %, with respective means of 34.2, 15.0 % and 19.0 % (Table 5). For natural soils, LL is a useful predictor of the shrink-swell potential (Sherrif, 1991). LL, PL, and PI all fall within the Federal Ministry of Works and Housing's foundation material restrictions (LL= 50 %, PL= 30 %, and PI= 20 %).

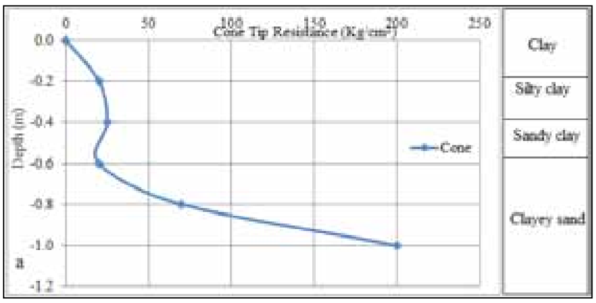

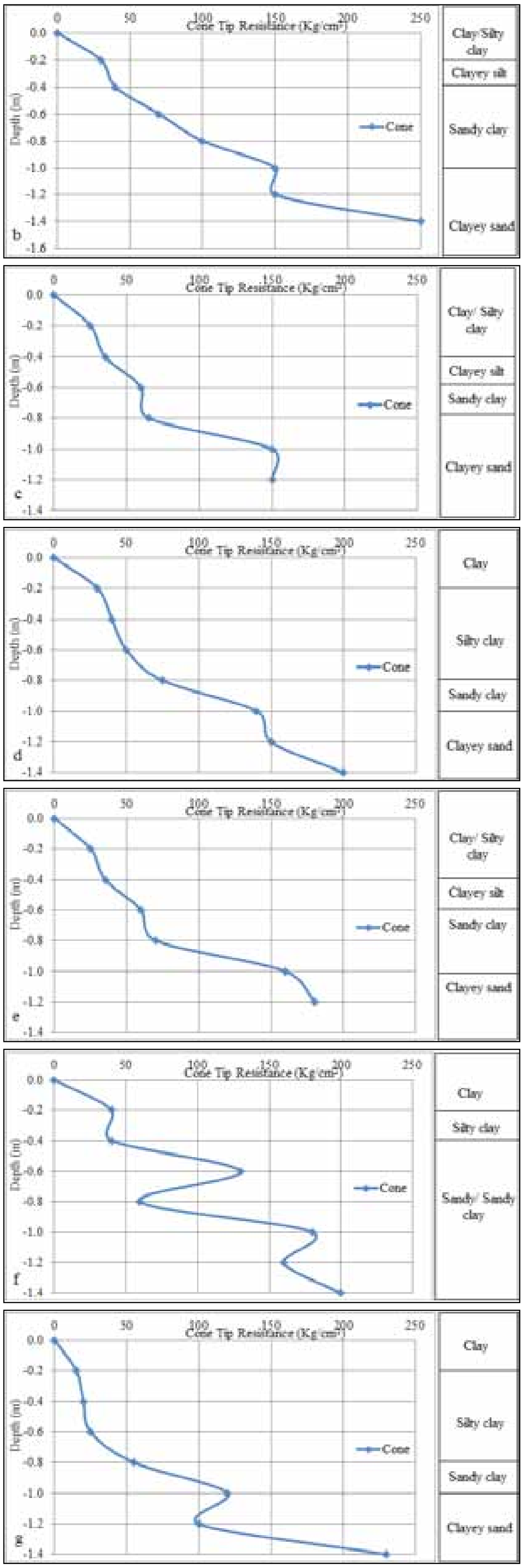

Figure 5. Depth (m) against Cone tip Resistance (kg/cm2)

Table 5. A Summary of Geotechnical Results

<table>
<tr><th colspan="10">Disturbed Sample (0.5 m)</th></tr>
<tr><th rowspan="2">Sample</th><th colspan="3">% passing Sieves</th><th colspan="3">Atterberg Limits (%)</th><th rowspan="2">NMC</th><th rowspan="2">AASHTO</th><th rowspan="2">UCS</th><th rowspan="2">Rating</th></tr>
<tr><th>No.4</th><th>No.6</th><th>No.200</th><th>LL</th><th>PL</th><th>PI</th></tr>
<tr><td>BT1</td><td>42.0</td><td>13.0</td><td>84.0</td><td>30.0</td><td>12.0</td><td>18.0</td><td>17.0</td><td>A-7-5</td><td>CL</td><td>Poor</td></tr>
<tr><td>BT2</td><td>47.0</td><td>21.0</td><td>82.0</td><td>37.0</td><td>17.0</td><td>20.0</td><td>11.0</td><td>A-7-6</td><td>CL</td><td>Poor</td></tr>
<tr><td>BT3</td><td>46.0</td><td>18.0</td><td>84.0</td><td>36.0</td><td>16.0</td><td>20.0</td><td>6.0</td><td>A-7-6</td><td>CL</td><td>Poor</td></tr>
<tr><td>BT4</td><td>40.0</td><td>23.0</td><td>71.0</td><td>31.0</td><td>14.0</td><td>17.0</td><td>11.0</td><td>A-7-6</td><td>CL</td><td>Poor</td></tr>
<tr><td>BT5</td><td>45.0</td><td>25.0</td><td>80.0</td><td>37.0</td><td>16.0</td><td>21.0</td><td>13.0</td><td>A-7-6</td><td>CL</td><td>Poor</td></tr>
<tr><td>Ave.</td><td>44.0</td><td>20.0</td><td>80.2</td><td>34.2</td><td>15.0</td><td>19.2</td><td>15.4</td><td></td><td></td><td></td></tr>
<tr><th colspan="11">Undisturbed Sample (1.5 m)</th></tr>
<tr><th rowspan="2">Sample</th><th rowspan="2">Bulk Density (Mg/m^3)</th><th colspan="4">Shear strength Parameters</th><th colspan="5">Consolidation parameters</th></tr>
<tr><th colspan="2">C (KN/m^2)</th><th colspan="2">Φ (°)</th><th colspan="2">Stress range</th><th>Mv (m^2/MN)</th><th colspan="2">Cv (m^2/yr)</th></tr>
<tr><td rowspan="3">BT1</td><td rowspan="3">2.2</td><td colspan="2" rowspan="3">72.0</td><td colspan="2" rowspan="3">21.0</td><td colspan="2">50-100</td><td>0.137</td><td colspan="2">3.90</td></tr>
<tr><td colspan="2">100-200</td><td>0.125</td><td colspan="2">3.90</td></tr>
<tr><td colspan="2">200-300</td><td>0.107</td><td colspan="2">3.90</td></tr>
<tr><td rowspan="3">BT2</td><td rowspan="3">2.1</td><td colspan="2" rowspan="3">73.0</td><td colspan="2" rowspan="3">19.0</td><td colspan="2">50-100</td><td>0.135</td><td colspan="2">3.60</td></tr>
<tr><td colspan="2">100-200</td><td>0.122</td><td colspan="2">3.70</td></tr>
<tr><td colspan="2">200-300</td><td>0.104</td><td colspan="2">3.60</td></tr>
<tr><td rowspan="3">BT3</td><td rowspan="3">2.1</td><td colspan="2" rowspan="3">73.0</td><td colspan="2" rowspan="3">18.0</td><td colspan="2">50-100</td><td>0.134</td><td colspan="2">3.50</td></tr>
<tr><td colspan="2">100-200</td><td>0.120</td><td colspan="2">3.50</td></tr>
<tr><td colspan="2">200-300</td><td>0.102</td><td colspan="2">3.50</td></tr>
<tr><td rowspan="3">BT4</td><td rowspan="3">2.1</td><td colspan="2" rowspan="3">72.0</td><td colspan="2" rowspan="3">18.0</td><td colspan="2">50-100</td><td>0.135</td><td colspan="2">3.60</td></tr>
<tr><td colspan="2">100-200</td><td>0.121</td><td colspan="2">3.60</td></tr>
<tr><td colspan="2">200-300</td><td>0.102</td><td colspan="2">3.70</td></tr>
<tr><td rowspan="2">BT5</td><td rowspan="2">2.1</td><td colspan="2" rowspan="2">73.0</td><td colspan="2" rowspan="2">18.0</td><td colspan="2">50-100</td><td>0.131</td><td colspan="2">3.60</td></tr>
<tr><td colspan="2">100-200</td><td>0.119</td><td colspan="2">3.60</td></tr>
<tr><td>Ave.</td><td>2.10</td><td colspan="2">72.60</td><td colspan="2">18.80</td><td colspan="2">200-300</td><td>0.102</td><td colspan="2">3.60</td></tr>
</table>

Sowers and Sowers (1970) characterized soils with a PI greater than 31% as extremely plastic, highly compressible, with low permeability, and low hydraulic conductivity. As a result, all samples analyzed from the study site fit into this category, and they would be ideal as supporting materials for shallow foundations, according to PI. Many attributes of clay and silt can be matched with the consistency limit using the plasticity chart (Fig.6), used in classifying fine-grain materials. The plasticity chart revealed a CL soil class above the A-line (Fig.6), indicating that the soils are primarily composed of inorganic materials with intermediate plasticity and compressibility and would have medium expansive potential (Chen, 1975; Peck et al., 1974) as a result of associated clay mineral content (Kalinski, 2011). This is in sync with Imeokparia and Falowo, (2019) studies carried out in a similar basement complex area of Owo, southwestern Nigeria. This is consistent with the findings of Imeokparia and Falowo (2019) in a comparable basement complex area in Owo, southwestern Nigeria. Inorganic clay elements of low-medium plasticity are also generally found in these soils, according to the Unified Soil Classification System (USCS). Moreso, according to the AASHTO (1982) classification system, these soils were similarly categorized as poor (A-7; A-7-5 to A-7-6) foundation materials with shrink-swell potential with moisture changes. Moisture content (NMC) depicts the clay content and type of soil material, by measuring the water-holding capability of soils (Sowers and Sowers, 1970). The soil's NMC soil range from 6.0-13.0 %, with an average of 9.6 %, indicative of a moderately plastic material (Underwood, 1967), also accords with the soil's plasticity (intermediate).

Similarly, the physical qualities of disturbed soil (bulk density, and shear strengths) have a significant impact on its stability (Kitutu, 2009). These soil properties were employed by Bidyashwari et al., (2017) to characterize the nature and behavior of soils. Table 5 shows that the bulk density (ɣB) ranges from 2.1 to 2.2 Mg/m^3, with an average value of 2.1 Mg/m^3. The ɣB values obtained here are consistent with (Seedman, 1986) observations that osmotic swelling of clay-composed materials occurs in samples with a bulk density of less than 2.45 Mg/m^3.

A material's shear strength refers to its capacity to withstand shearing deformational pressures (Sowers, 1963). C range from 72 KN/m^2-73 KN/m^2, while ϕ range from 18.0°-21.0°, averaging 72.6 KN/m^2 and 18.8° respectively (Table 5). The high values of C and ϕ are owing to an excellent clay-sand mixture, in which the clays supply the requisite cohesiveness (C) and the sands provide good frictional contact between the particles-thus, higher frictional strength is achievable by combining both C and ϕ (Idris and Igwe, 2018).

Consolidation has long been thought to be a fundamental phenomenon that effectively explains soil behavior in foundation issues (Adebisi and Adeyemi, 2012). Table 5 shows the results of the consolation test under various stress levels. Mv and Cv, which are the consolidation parameters, remain fairly constant with applied pressure such that at stress ranges of 50-100, 100-200, and 200-300 KN/m^2, Mv range from $1.31x10^{-1}$-$1.37x10^{-1}$ m/MN, $1.20x10^{-1}$-$2.51x10^{-1}$ m/MN and 1.02-$1.07x10^{-1}$ m/MN, indicating very low compressibility (Mckinlay, 1996), with no likelihood for differential settlement of the structure while Cv also remains fairly constant (3.50-3.90 m^2/yr) at all pressure range. The implication is that when the site is loaded, the soil will have a modest consolidation settlement.

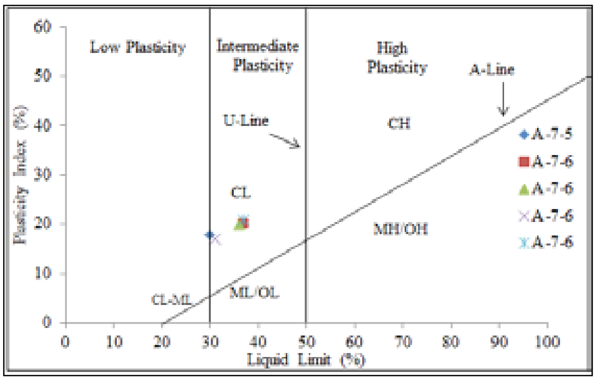

Figure 6. Plasticity chart showing the study soil samples.

Table 6. Soil Expansion Relative to Liquid and Plasticity Index.

S/N	Chen, (1975)		Peck *et al.*,(1974)		Expansion	Samples
	Liquid limit	Plasticity Index	Plasticity Index	Swelling Potential		
1	<30	0-15	0-15	Low	Low	Nil
2	30-40	10-35	10-35	Medium	Medium	1, 2, 3, 4 and 5
3	40-60	20-55	20-35	High	High	Nil
4	>60	>35	Above 35	Very High	Very high	Nil

Furthermore, the compressibility index (Eqn. 2), Cc expression given by (Terzaghi and Peck, 1969) for naturally cemented clays of low to moderate sensitivity modified after (Skempton and Northey, 1952), was used to hypothetically predict the susceptibility of these soils to settlement.

$$Cc = 0.009\ (W_L - 10) \quad \text{………………………….........…} (2)$$

Where Cc = Compressibility index

WL= Liquid limit in percentage

Here in this study, Cc has been found to range from low to moderate (Table 7) however, some of the soils have a moderate LL, which may cause a moderate amount of foundation settling. Compaction can improve the soil's suitability as a foundation because compaction minimizes void spaces, pore pressure, and its implications in construction projects, boosting its applicability, notably as fills (Aghamelu *et al.*, 2011).

Table 7. Soil Compressibility Analyses According to Terzaghi and Peck (1969).

S/N	Liquid Limit (%)	Compressibility Index; Cc	Class
1	30.0	0.18	Low
2	37.0	0.24	Moderate
3	36.0	0.23	Moderate
4	31.0	0.19	Low
5	37.0	0.24	Moderate

5. Conclusion and Recommendation

To define the sub-soil environment suitability for a proposed building foundation design, geophysical (vertical electrical sounding; VES) and geotechnical techniques (Cone penetration test; CPT, consistency test, gradation, shear strength, and consolidation analysis) were used. The VES data revealed three (3) geoelectric layers with distinctive H-curve patterns: topsoil (89.10-253.80 Ωm, 1.38 m), weathered basement (24.00-50.10 Ωm, 8.62m), and fractured/fresh basement (190.80-585.00 Ωm, depth-rock head = 9.84 m). However, the top soils (163.68 Ωm), weathered basement (35.49 Ωm), and fractured/fresh basement units (378 Ωm) were classed as somewhat competent, incompetent, and competent, respectively, based on mean resistivities. Although the topsoil is moderately competent but has a thin thickness (only 2 m), the weathered materials in the basement have a massive thickness (9.8 m) that may aid in the even distribution of foundation loads.

The CPT curves reflected a subsurface environment with clay, silty clay, sandy clay, and clayey sand lithologies of varying thicknesses and penetration resistances, as well as different ranges of allowable bearing capacities, qa allowable bearing pressures, ABC and ultimate bearing capacities, such as 79.2-660 KN/m^2, 71.3-594.0 KN/m^2, and 23.8-198.0 KN/m^2. From 0.8 m depth, clayey-sand materials with reasonable bearing capacity values that would optimally function as foundation materials were discovered, with qc >100 kg/cm^2. Grain size distribution indicates clay-dominated materials with >35% particles passing the No.200 sieve) recommendation for materials for use as foundation support by the Federal Ministry of Works and Housing (1972). The typical results for LL, PL, PI, and NMC were 34.2 percent, 15.0 percent, 19.0 percent, and 9.6 percent, indicating a low plastic and high metal content, respectively.

Materials formed of osmotic swelling potentials with B 2.45 Mg/m^3 have a bulk density of 2.1 Mg/m^3. C and ϕ denote a large proportion of clay-sand admixture, resulting in increased shear strength. Finally, the consolidation parameter; Mv remains fairly constant with changes in applied pressure (50-100, 100-200, and 200-300 KN/m^2) as $1.31x10^{-1}$-$1.37x10^{-1}$ m/MN, $1.20x10^{-1}$-$2.51x10^{-1}$ m/MN and 1.02-$1.07x10^{-1}$ m/MN respectively indicating low compressible soils. Also, at all pressures, Cv is pretty stable (3.50-3.90 m2/yr). The implication is that when the soils are loaded, they will be prone to low to moderate deformation (low compressibility and consolidation).

As a result, where earth materials with suitable permitted such as qa, ABP and qu exist, a shallow foundation depth with a base of 0.8 m or above is advised.

References

Abam, T. K. S., 2018. Exploring Ground Conditions for Sustainable Building Foundation Design. In: Tijani, M. N. (Eds.): Proceedings of First and Second International Conferences of the Nigerian Association for Engineering Geology and the Environment (NAEGE), Lagos, Nigeria, 2016 and 2017.1.

Adebisi, N.O. and Adeyemi, G.O., 2012. Assessment of compressibility characteristics of residual laterised soils in southwestern Nigeria. International Journal of Biological and Physical Sciences 17:198-208.

Agada, I., Ibuot, J.C., Ekpa, M., and Obiora, D.N., 2017. Investigation of subsurface for construction purposes in Makurdi, Benue State, Nigeria, using electrical resistivity method. Journal of Geology and Mining Research 9:9-17.

Aghamelu, O.P., Odoh, B.I., and Ezeh, H.N., 2011. Use of Accelerated Procedure to Estimate the Behaviour of Shallow Foundation. International Journal of Basic and Applied Sciences 11:82-88.

Aizebeokhai, A.P., Oyeyemi, K.D., 2017. Geoelectrical characterization of basement aquifers: The case of Iberekodo, Southwestern Nigeria. Hydrogeology Journal 26:651–664. doi:10.1007/s10040-017-1679-9.

Akintorinwa, O. J. and Adesoji, J. I., 2009. Application of geophysical and geotechnical investigations in engineering site evaluation. International Journal of Physical science 4:443-454.

American Association of State Highway and Transportation Officials (AASHTO) 2982. Materials, part 1, specifications, Washington.

Amanambu, A. C. (2015). Geogenic Contamination: Hydrogeochemical processes and relationships in Shallow Aquifers of Ibadan, South-West Nigeria. Bulletin of Geography. Physical Geography Series, 9:5–20. http://dx.doi.org/10.1515/bgeo-2015-0011.

Anifowose, A.Y.B. and Borode, A.M., 2007. Photogeological study of the fold structure in Okemesi area, south-western Nigeria. J. Min Geol. 43:125–130.

Arora, K.R., 2008. "Soil Mechanics and Foundation Engineering" 8th edn. Standard Publishers Distributors, Delhi. pp.69-356.

Atkinson, J. 1993. An introduction to the mechanics of soils and foundations. McGraw-Hill, New York.

Ayodele, S.O., 2015. The geology, geochemistry, and petrogenetic studies of the Precambrian Basement rocks around Iworoko, Are, and Afao area, Southwestern Nigeria. J Environ Earth Sci. 5:58–66.

Baldi, G., Bellotti, R., Ghionna, V.N., and Lo Presti, D.C.F., 1995. Modulus of sands from CPT and DMT: Proceedings of the 12th International Conference on Soil Mechanics and Foundation Engineering. 165–170.

Bell, F.G., 2007. Engineering geology. Elsevier, Amsterdam.

Bidyashwari, H., Kushwaha, 1. R.S., Chandra, M., Okendro, M., 2017. Physical Properties of Soil and Its Implication to Slope Stability of Nungbi Khunou, NH-150, Manipur. International Journal of Geosciences 8:1332-1343. https://doi.org/10.4236/ijg.2017.811077.

Bremmer, C.N., 1999. Developments in geomechanical research for infrastructural projects, in 12th European Conference on Soil Mechanic and Geotechnical Engineering: Geotechniek, Special Issue: 52–55.

B.S.I., 1990. Methods of test for soil for civil engineering purposes. BS1:377, London.

Burke, K.C., Freeth, S.J., Grant, N.K., 1976 The Structure and Sequence of Geological Events in the Basement Complex of Ibadan Area, Western Nigeria, Prec. Res. 3(6).

Chen, H., 1975. "Foundations on Expansive Soils" Elsevier Scientific Publishing Co. New York.

Coerts, A., 1996. Analysis of static cone penetration test data for subsurface modeling. A methodology-Ph.D. thesis, Netherlands geophysical studies. 210–263.

Falowo, O.O., 2018. Geochemical and engineering properties of selected lateritic deposits in Akure Metropolis as highway subgrade foundation material. Asian J Geol Res. 1:1–14; Article No. AJOGER.41867.

Federal Ministry of Works and Housing (FMWH), 1972. Highway manual part 1, road and bridge design. Federal Ministry of Works and Housing, Lagos.

Graham, R.C., Rossi, A.M., Hubbert, K.R., 2010. Rock to regolith conversion: producing hospitable substrates for terrestrial ecosystems. The Geological Society of America. 20:4–9.

Guihéneuf, N., Boisson, A.O., Bour, O., Dewandel, B., Perrin, J., Dausse, A., 2014. Groundwater flows in weathered crystalline rocks: Impact of piezometric variations and depth-dependent fracture connectivity. Journal of Hydrology. 511320–334.

Hill, I.G., Worden, R.H. and Meighan, I.G., 2000. Geochemical evolution of palaeolaterite: the interbasaltic formation, Northern Ireland. J. Chem. Geol.166:65-84.

Idris, I.G. and Igwe, O., 2018. Assessment of Foundation Instability Using Integrated Geotechnical and Geophysical Techniques: A Case Study of Giza, Keana LGA, Nasarawa State, North Central Nigeria. American Scientific Research Journal for Engineering, Technology, and Sciences 41:85-108.

Iloeje, M.P., 1981. New geography of Nigeria. Longman, Nigeria. 26–28.

Imeokparia, E.G. and Falowo, O.O., 2019. Subsoil Foundation Support Assessment in Owo Area of Ondo State, Southwestern Nigeria.Geotech. Geol. Eng. https://doi.org/10.1007/s10706-019-01144-0.

Jun-Jie, H., Ya-guang, Q., Wei, W., Lei, W., 2017. "Strength Response Characteristics and Coupling Support of Deep Roadway in Soft Rock Masses" Cogent Engineering.

Kalinski, M.E., 2011. "Soil Mechanic Lab Manual" 2ndedn. Wiley E-Text. 7-23.

Kitutu, M.G., Muwanga, A., Poesen, J., Deckers, J.A., 2009. Influence of Soil Properties on Landslide Occurrence in Bududa District, Eastern Uganda. African Journal of Agricultural Research 4:611-620.

Lowrie, W., 2007. Fundamentals of geophysics, 2nd edn. Cambridge University Press, Cambridge.

Luna, R. and Jadi, H., 2000. Determination of dynamic soil properties using geophysical methods Proc. 1st Int. Conf. on the Application of Geophysical and NDT Methodologies to Transportation Facilities and Infrastructure Geophysics(Federal Highway Administration, Saint Louis, MO). 3:1–15.

Mckinlay, D.G., 1996. Civil Engineering Materials. Macmillan Education Ltd. 340p.

Meyerhof, G.G., 1974. General report: state-of-the-art of penetration testing in countries outside Europe. In: Proceedings of the 1st European symposium on penetration testing 2.1:40–48.

Mosallanezhad, M. and Moayedi, H., 2017. "Comparison Analysis of Bearing Capacity Approaches for the Strip Foundation on Layered Soils. "Arabian Journal for Sciences and Engineering 42:3711-3722.

Mosuro, G.O., Omosanya, K.O., Bayewu, O.O., and Oloruntola, M.O., 2017. Assessment of groundwater vulnerability to leachate infiltration using electrical resistivity method. Appl. Water Sci.7:2195-2207. https://doi.org/10.1007/s13201-016-0393-4.

Ojo, J.S., Olorunfemi, M.O., Akintorinwa, O.J., Bayode, S., Omosuyi, G.O., and Alinluyi, F.O., 2015. Subsoil competence characterization of the Akure metropolis, southwest Nigeria. J. Geogr. Environ Earth Sci. Int. 3:1-14. https://doi.org/10.9734/JGEESI/2015/15851.

Oke, S.A., Okeke, O.E., Amadi, A.N., and Onoduku, U.S., 2009. Geotechnical properties of the sub-soil for designing shallow foundations in some selected parts of Chanchaga area, Minna, Nigeria. J Environ Sci. 1:45–54.

Oladapo, M.I., Mohammed, M. O.O. and Adetola, B.A., 2004. Geo-electrical Investigation of Ondo State Housing Corporation Estate Ijapo, Akure, South Western Nigeria. J. Mining Geol. 40:41–48.

Olayinka, A.I. and Yaramanci, U., 1999. Choice of the best model in 2-D geoelectrical imaging: a case study from a waste dump site. Eur J Environ Eng Geophys 3:221–244.

Olorunfemi, M.O., Ojo, J.S., Idornigie, A.I. and Oyetoran, W.E., 2005. Geophysical investigation of structural failure of a factory site in Asaba area, Southern Nigeria. Journal Of Mining and Geology 41:111 – 121.

Oyeyemi, K.D., Aizebeokhai, A.P. and Oladunjoye, M.A., 2015a. Integrated geophysical and geochemical investigations of saline water intrusion in a coastal alluvial terrain, southwestern Nigeria. International Journal of Applied Environmental Sciences 10:1275–1288.

Oyeyemi, K.D., Olofinnade, O.M., Aizebeokhai, A.P., Sanuade, O.A., Oladunjoye, M.A., Ede, A.N., 2020. Geoengineering site characterization for foundation integrity assessment, CogentEngineering 7:1,1711684.https://doi.org/10.1080/23311916.2020.1711684.

Oyinloye, M.A., Modebola-Fadimine, F.T., 2013. Geo-information for urban waste disposal and management. The case study of Owo LGA, Ondo State, Nigeria. Int. J. Eng. Sci. 2:19–31.

Peck, R.B., Hanson, W.F. and Thornburn, T.H., 1974. Foundation Engineering (2nd edition), John Wiley & Sons, New York.

Sattar, G.S., Keramat, M., and Shahid, S., 2004. Deciphering transmissivity and hydraulic conductivity of the aquifer by vertical electrical sounding (VES) experiments in Northwest Bangladesh. J Appl. Water Sci. 6:35–45.

Savvaidis, A., Tsokas, G., Soupios, P., Vargemezis, G., Manakou, M., Tsourlos, P., 1999. Geophysical prospecting in the Krousovitis dam (N Greece) by seismic and resistivity geophysical methods J. Balkan Geophys. Soc. 2:128–39.

Seedman, R., 1986. The behavior of clay shales in water; Canadian Geotech. J. 23:18–22.

Sheriff, R.E., 1991. "Encyclopedic Dictionary of Exploration Geophysics" Society of Exploratory Geophysicists, Tulsa.

Skempton, A.W., and MacDonald, D.H., 1956. The allowable settlement of buildings. Proc Inst Civ Eng. 3:727–784.

Skempton, A.W., and Bjerrum, L., 1957 A contribution to the settlement analysis of foundation on clay, Geotechnique 7:168-178.

Skempton, A.W., and Northey, R.D., 1952. The sensitivity of clays. Geotechnique 30:30–53.

Soupios, P.M., Papazachos, C.B., Vargemezis, G., Fikos, I., 2005. Application of modern seismic methods for geotechnical site characterization Proc. Int. Workshop in Geoenvironment and Geotechnics (Milos Island, Greece, 12–14 September), 163–70.

Sowers, G.B. and Sower, G.E., 1970 "Introductory Soil Mechanics and Foundations" Macmillan Book Publishing Company, London. 337p.

Sowers, G.E., 1963. Strength testing of soils; laboratory shear testing of soils. ASTM Special Technical Publication 361, American Society for Testing and Materials, Philadelphia.

Terzaghi, K. and Peck, R.B., 1969. Soil mechanics in engineering practice. Wiley, New York.

Tijani, M.N., Alichi, U.A. and Diop, S., 2009. Impact of Bedrock types on the hydraulic characteristics of weathered basement aquifers: a case study from Southwestern Nigeria. Joint International convention of 8th IAHS Scientific Assembly and 37th IAH Congress, Hyderabad, India.

Tijani, M.N., Obini N. and Inim, I.J., 2021. Estimation of aquifer hydraulic parameters and protective capacity in basement aquifer of south-western Nigeria using geophysical techniques. Environmental Earth Sciences.80:466. https://doi.org/10.1007/s12665-021-09759-4.

Underwood, L.B., 1967. Classification and identification of shales. J. Soil Mech. Found. Div. ASCE. 93: 97-116.

Vander-Velpen, B.P.A. 2004. Win-RESIST Version 1.0 Resistivity Depth Sounding Interpretation Software. M.Sc Research Project, ITC, Delft, the Netherlands.

Venkateswara, V. R., Srinivasa, R., Prakasa, R. B. S and Koteswara, R P., 2004. Bedrock investigation by seismic refraction method-a case study J. Ind. Geophys. Union 8:223–8.

Willian, M., 2010. Geophysical methods for determining the geotechnical engineering properties of earth materials. Preliminary investigations: Caltrans Division of Research and Innovation, Prepared by William Owen Office of Geotechnical Support.

JJEES

JJEES (2022) 13 (4): 298-306
ISSN 1995-6681

Jordan Journal of Earth and Environmental Sciences

Bioremediation of Cassava, Cocoa, and Palm Oil Industrial Effluents Using Indigenous Bacteria and Fungi

Stephen Ojodale*, Adewale Olalemi, Felix Akinyosoye

Department of Microbiology, Federal University of Technology, P.M.B 704, Akure, Ondo State, Nigeria

Received 13th May 2021; Accepted 15th May 2022

Abstract

Release of untreated or partially treated industrial effluents into aquatic systems may pose significant risks to human, animal, and environmental health. This study investigated the bioremediation potentials of indigenous bacteria and fungi in some agro-based industrial effluents. Effluent samples (n=90) from cassava, cocoa, and palm oil industries in Ondo State, Nigeria were collected for five weeks. Bacteria and fungi in the effluent samples were isolated and identified using standard microbiological methods. The physicochemical characteristics of the effluent samples were determined using standard methods. Bacterial and fungal isolates with a high rate of utilization of the effluents were selected for the bioremediation assay. Results revealed that effluent samples from the palm oil industry had the highest bacterial and fungal counts, while effluents from the cocoa industry had the least. In all the effluent samples, *Bacillus*, *Lactobacillus,* and *Pseudomonas* were the most prevalent bacteria, while *Aspergillus* was the most prevalent fungi. The mean values of pH in cassava, cocoa, and palm oil effluent samples were 5.4, 6.4, and 4.4, respectively. High levels of cyanide and oil were detected in cassava and palm oil effluent samples, respectively. In terms of reduction of biological oxygen demand (BOD) and chemical oxygen demand (COD) in all the effluent samples, treatments containing the consortium of the isolates exhibited the highest bioremediation potential followed by treatments containing *Corynebacterium manihot* in cassava effluents; *Lactobacillus delbrueckii* in cocoa effluents; and *Penicillium notatum* in palm oil effluents. The findings of the study suggest that a consortium of the isolates, *C. manihot, L. delbrueckii,* and *P. notatum* represent promising microorganisms for bioremediation of cassava, cocoa, and palm oil industrial effluents.

Keywords: *bioremediation, environmental protection, agro-allied industrial effluents, microorganisms, pollution.*

1. Introduction

The threat to human and aquatic lives posed by industrial liquid and gaseous effluents cannot be over-emphasized, because industrial effluents are major sources of toxic contaminants in any environment (Kanu and Achi, 2011). Rapid industrialization and urbanization have enhanced the level of organic contaminants in the environment (Ethan *et al.,* 2003). Rivers and streams are constantly exposed to health-related risks as a result of indiscriminate discharge of untreated or partially treated industrial effluents (Adekunle and Eniola, 2008; Dash *et al.,* 2009; Kanu and Achi, 2011). The increased importance of cassava in agricultural and economic development as well as in food security particularly in Nigeria should give its processing and waste handling more attention (Arimoro *et al.,* 2008). During processing, three major waste streams are generated, these are liquid (cassava mill effluents), solid (cassava peels and sieves), and gaseous emissions. Cassava mill effluents are produced from various stages such as washing, grating, and moisture extraction processes. The quality of cassava mill effluents is assessed based on their physical, chemical, and biological constituents. Studies have shown that the physical and chemical constituents of cassava mill effluents released from different processing facilities often contaminate soils at the point of discharge i.e., the organic components in the effluents may negatively impact the soil ecosystem (Ogboghodo *et al*., 2006; Igbinosa, 2015).

The total installed cocoa processing capacity of Nigerian firms is at least 105,000 tons per annum while at least 45,000 tons is processed into intermediate products for local beverage industries or export. In Ondo State, one of the major tree crops is cocoa, its production and processing have earned the region an economic boost in recent years. Effluents from cocoa processing factories have been demonstrated to contain microorganisms and heavy metals that may pose a significant risk when discharged into the environment (Akinnusotu and Arawande, 2016). In addition, the palm oil industry has been growing rapidly as a result of the rising global demand for fats and oil, thus becoming a major contributor to the economy of several tropical countries, including Nigeria. Palm oil mill effluent (POME) is a brown slurry of organic solids (4-5%), residual oil (0.5-1.0%), and water (95%) which is generated during the multiple processing steps of crude oil production (Wu *et al*., 2009). POME has high organic content, biological oxygen demand (BOD), and chemical oxygen demand (COD) and is known to cause environmental problems such as eutrophication and water pollution (Osunbitan *et al.,* 2000; Kanu and Achi, 2011).

Generally, these effluents from cassava, cocoa, and palm oil processing factories contain substances that may be

* Corresponding author e-mail: ojodalestephen@gmail.com

lethal, mobile in soil, affect biodiversity, cause the extinction of benthic macroinvertebrates and other aquatic lives, inhibit germination of cereal seed and alter microbial communities (Arimoro *et al.,* 2008; Wu *et al*., 2009; Akinnusotu and Arawande, 2016). It is important to subject these effluents to various treatment processes before discharging them into the environment (Shah, 2017). Bioremediation is a process in which beneficial microorganisms such as yeast, fungi, or bacteria are used to clean up contaminated soil or water. It is defined as the elimination, attenuation, or transformation of polluting or contaminating substances through the application of biological processes. It provides a technique for cleaning up pollution by enhancing the natural biodegradation processes (Enerijiofi *et al*., 2017; Ganapathy *et al*., 2019).

This study was aimed at determining the bioremediation potentials of indigenous bacteria and fungi in some agro-based industrial effluents. The specific objectives of this study were to isolate and identify bacteria and fungi from cassava, palm oil, and cocoa industrial effluents; assess the rate of utilization of the effluents by the isolates; determine the physicochemical characteristics of the effluent samples, and evaluate the bioremediation potentials of selected isolates on the effluent samples.

2. Materials and Methods

2.1 Description of the study area

Cassava effluents were collected from Matna Foods Company Limited, Akure – Owo expressway. Cocoa effluents were collected from Plantation Nigeria Limited, Akure and palm oil effluents were collected from Tohkl Palm Oil Mill, Aule Village, Akure. The agro-based industries are all located in Ondo State, Nigeria (Figure 1).

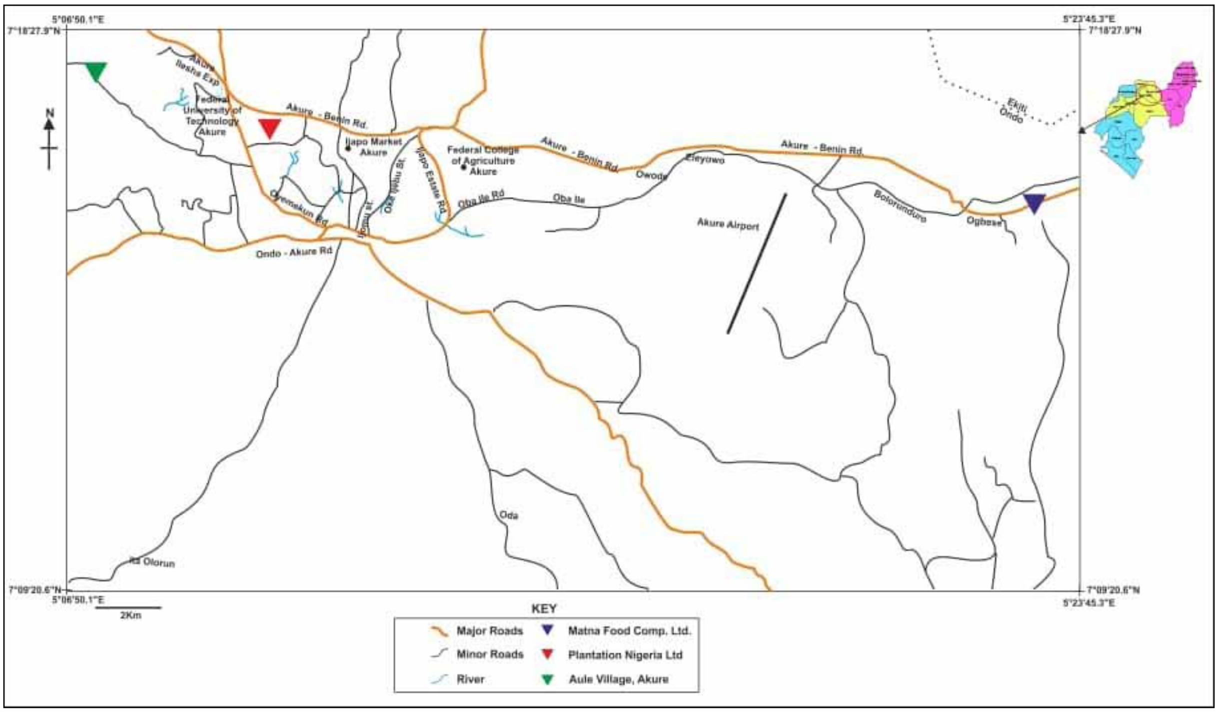

Figure 1. Map showing the sampling points of cassava, cocoa, and palm oil effluents.

2.2 Collection of effluent samples

Cassava, cocoa, and palm oil effluent samples were collected weekly over five (5) weeks to monitor trends and variations in microbial and physicochemical properties of the effluents. On each sampling occasion, effluents (1 L) were collected in duplicates at 10 am from their respective processing factories into sterile screw-capped bottles from each sampling point. The samples were stored in a cool box with ice packs and were transported to the laboratory within one (1) hour.

2.3 Enumeration and identification of bacterial and fungal populations in effluent samples

Serial dilutions were carried out weekly on each of the effluent samples and were cultured using the pour plate method. Nutrient agar (NA), Manitol Salt agar (MSA), Eosin Methylene Blue agar (EMB), De Manrogosa agar (MRS), Potato Dextrose agar (PDA), and mineral salt medium supplemented with 1% v/v of effluent samples were used for the enumeration of bacteria and fungi in the effluent samples. The agar plates were incubated at 35°C for 24 hours (NA, EMB, MSA, and MRS); and 25°C for 48 - 72 hours (PDA). Discrete colonies of bacteria and fungi were counted and expressed as colony-forming units per milliliter (CFU/ml) and spore-forming unit per milliliter (SFU/ml) respectively. The isolates were sub-cultured repeatedly to obtain pure isolates and were characterized further using morphological, physiological, and biochemical properties that included Gram reaction, catalase test, motility test, oxygen relation, sulphide test, indole production test, and carbohydrates (glucose, lactose, fructose, dextrose, maltose, tryptose, and sucrose) utilization test. Thereafter, the bacterial isolates were identified using Bergey's Manual of Determinative Bacteriology, and fungal isolates were identified using Practical Mycology: Manual for Identification of Fungi.

2.4 Determination of the rate of utilization of effluent samples by the isolates

The method of Enerijiofi *et al.* (2017) was adopted. The mineral salt medium (MSM) (oil agar medium) for palm oil utilizing bacteria was prepared to contain; 4 g NH_4Cl, 1.8 g K_2HPO_4, 1.2 g KH_2PO_4, 0.2 g $MgSO_4.7H_2O$, 0.1 g NaCl, 0.01 g $FeSO_4$, 15 g agar and 1000 ml distilled water. For fungi, the medium had 10 g NaCl, 0.42 g $MgSO_4.7H_2O$, 0.29 g KCl, 0.83 g KH_2PO_4, 1.25 g Na_2HPO_4, 0.42 g $NaNO_3$, 20 g agar, 1000 ml distilled water and pH of 7.2. The medium was supplemented with 1% v/v of effluent as a carbon and nitrogen source. One milliliter of the serially diluted effluent sample was pure-plated on the media. Agar plates for bacteria and fungi were incubated appropriately and colonies were counted and recorded.

2.5 Determination of physicochemical characteristics of effluent samples

The temperature of the effluent samples was determined on-site using a mercury-in-glass thermometer. Electrical conductivity was determined using a conductivity meter (YSI Model 34). The pH, dissolved oxygen (DO), total dissolved solids, biological oxygen demand (BOD), chemical oxygen demand (COD), oil, cyanide, and total carbohydrate and ash content in the effluent samples were measured weekly using standard methods.

2.6 Determination of bioremediation potential of isolates on effluent samples

Shake Flask Degradation test as described by Enerijiofi *et al.* (2017) was adopted. An aliquot of 0.2 ml (standardized to 10^6 CFU/ml for bacteria and SFU/ml for fungi) of the inoculum of bacteria and fungi was dispensed into the flask containing 200 ml of sterilized cassava, palm oil, and cocoa mill effluents, separately in each treatment and mixed to form a consortium. All flasks were incubated at room temperature (28±2°C) on a rotary shaker at 120 rpm for 5 days. During the incubation period, temperature, pH, COD, BOD, and bacterial and fungal load were monitored at 24 hours intervals for five days.

2.7 Statistical analysis

Data obtained from this study were subjected to descriptive statistics. One-way Analysis of Variance was carried out and means were separated by Duncan's New Multiple Range test using SPSS version 22, at $P \leq 0.05$ level of significance. Values were presented as mean values ± standard deviation.

3. Results

3.1 Detection of bacteria and fungi in effluent samples

The total viable count of bacteria in cassava effluent samples ranged from 7.6×10^2 to 1.13×10^3 CFU/ml; 3.3×10^2 to 5.3×10^2 CFU/ml in cocoa effluent samples and 7.4×10^3 to 8.5×10^3 CFU/ml in palm oil effluent samples (Figure 2).

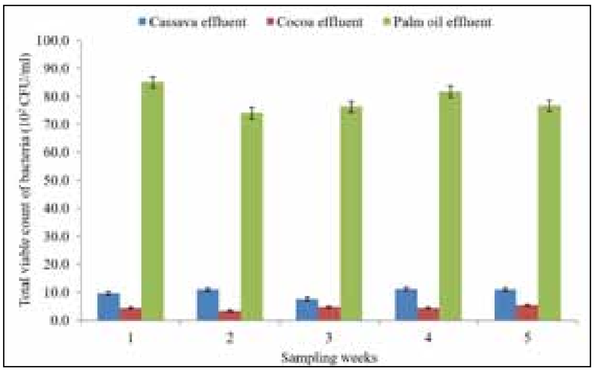

Figure 2. Total viable count of bacteria in effluent samples.

The total count of fungi in cassava effluent samples ranged from 2.3×10^3 to 5.3×10^3 SFU/ml; 2.0×10^3 to 4.6×10^3 SFU/ml in cocoa effluent samples and 9.0×10^3 to 1.06×10^4 SFU/ml in palm oil effluent samples (Figure 3).

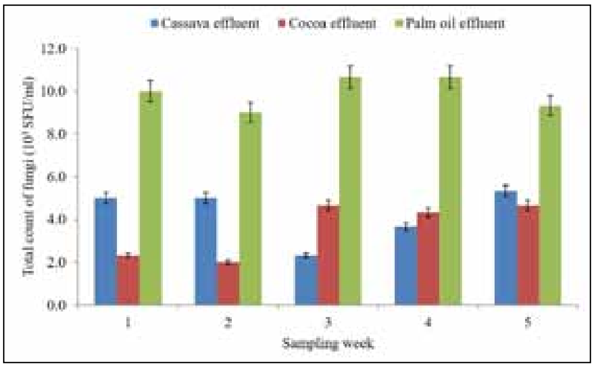

Figure 3. Total count of fungi in effluent samples.

Based on morphological and biochemical characteristics, the bacterial isolates detected in cassava effluent samples were *Pseudomonas aeruginosa*, *Micrococcus luteus*, *Bacillus subtilis*, *Staphylococcus aureus*, *Corynebacterium manihot*, *Morganella morganii*, *Lactobacillus acidophilus,* and *Lactobacillus fermentum*. In cocoa effluent samples, *L. delbrueckii*, *P. fluorescence*, *Proteus mirabilis,* and *B. subtilis* were isolated, whereas, in palm oil effluent samples, *S. aureus*, *B. cereus*, *M. luteus*, *Klebsiella pneumonia*, *Providencia vermicola*, *L. delbrueckii,* and *P. aeruginosa* were isolated. Of all the isolates, *Bacillus*, *Lactobacillus* and *Pseudomonas* were the most prevalent bacteria in cassava, cocoa, and palm oil effluent samples (Table 1).

The fungal isolates detected in cassava effluent samples were *Rhizopus stolonifer, Aspergillus fumigatus, A. niger, Saccharomyces cerevisiae,* and *Candida tropicalis.* In cocoa effluent samples, *S. cerevisiae, Penicillium notatum, A. fumigatus,* and *C. pelliculosa* were isolated, whereas, in palm oil effluent samples, *A. fumigatus, A. niger,* and *P. notatum* were isolated. Of all the isolates, *Aspergillus* species were the most prevalent fungi in cassava, cocoa, and palm oil effluent samples (Table 2).

Table 1. Frequency of occurrence of bacterial isolates in the effluent samples.

Effluent	Bacteria	Weeks					Occurrence (%)
		1	2	3	4	5	
Cassava	P. aeruginosa	+	+	+	-	-	13.0
	M. luteus	+	+	-	-	-	8.7
	B. subtilis	+	-	+	-	-	8.7
	S. aureus	-	+	-	+	-	8.7
	C. manihot	-	-	-	+	+	8.7
	M. morganii	-	+	+	+	+	17.4
	L. acidophilus	-	+	+	+	+	17.4
	L. fermentum	-	+	+	+	+	17.4
Cocoa	L. delbrueckii	+	+	+	-	-	27.3
	P. fluorescence	+	+	-	-	-	18.2
	P. mirabilis	-	+	+	+	+	36.3
	B. subtilis	-	-	-	+	+	18.2
Palm oil	S. aureus	+	+	-	-	+	18.8
	B. cereus	+	+	-	-	-	12.5
	M. luteus	-	-		+	+	12.5
	K. pneumoniae	-	-	+	+	+	18.8
	P. vermicola	-	+	-	-	-	6.2
	L. delbrueckii	-	+	-	+	+	18.8
	P. aeruginosa	+	-	+	-	-	12.5

Key: + = Present, - = Absent; Percentage of occurrence of each isolate was calculated by dividing the number of times an isolate was detected in the effluent samples by the total number of times all isolates were detected in the effluent samples over the five weeks multiplied by 100.

Table 2. Frequency of occurrence of fungal isolates in the effluent samples

Effluent	Fungi	Weeks					Occurrence (%)
		1	2	3	4	5	
Cassava	R. stolonifer	-	-	-	+	+	11.8
	A. fumigatus	+	-	+	-	+	17.7
	A. niger	-	+	+	+	+	23.5
	S. cerevisiae	-	+	+	+	+	23.5
	C. tropicalis	-	+	+	+	+	23.5
Cocoa	S. cerevisiae	+	+	+	-	-	27.3
	A. fumigatus	+	+	-	-	-	18.2
	P. notatum	-	+	+	+	+	36.3
	C. pelliculosa	-	-	-	+	+	18.2
Palm oil	A. fumigatus	+	+	-	-	+	42.9
	A. niger	-	+	-	-	-	14.3
	P. notatum	-	+	-	+	+	42.8

Key: + = Present, - = Absent; Percentage of occurrence of each isolate was calculated by dividing the number of times an isolate was detected in the effluent samples by the total number of times all isolates were detected in the effluent samples over the five weeks multiplied by 100.

3.2 Rate of the utilization of effluent samples by the isolates

The total count of bacteria and fungi on mineral salt medium (MSM) supplemented with the cassava, cocoa, and palm oil effluent samples were lower than the mean load of bacteria and fungi from the effluent samples cultured on general-purpose media (Table 3). *M. morganii*, *C. manihot*, *P. aeruginosa, C. tropicalis,* and *S. cerevisiae* demonstrated higher rates of utilization of cassava effluents. *P. fluorescence, L. delbrueckii, C. pelliculosa,* and *S. cerevisiae* showed higher rates of utilization of cocoa effluents, whereas *P. aeruginosa, M. luteus, P. vermicola* and *P. notatum* exhibited higher rates of utilization of palm oil effluents.

Table 3. Total count of bacteria and fungi on mineral salt medium and general-purpose media.

Effluent samples	Bacteria on MSM (CFU/ml × 10^4)	Bacteria on NA (CFU/ml × 10^6)	Fungi on MSM (SFU/ml × 10^2)	Fungi on PDA (SFU/ml × 10^3)
Cassava	2.57 ± 0.8^a	1.02 ± 1.3^b	3.7 ± 0.2^b	4.3 ± 0.6^b
Cocoa	2.07 ± 0.0^b	0.44 ± 0.7^c	4.3 ± 0.1^b	3.6 ± 0.6^c
Palm oil	2.24 ± 0.4^b	7.84 ± 1.6^a	6.2 ± 0.3^a	9.9 ± 0.4^a

Key: NA = nutrient agar, PDA = potato dextrose agar, CFU = colony forming unit, SFU = spore forming unit, ml = milliliter, MSM = mineral salt medium. Data presented as Mean ± SD, values in the same column with the same superscript are not significantly different ($p \leq 0.05$)

3.3 Physicochemical characteristics of effluent samples

The mean values of pH in cassava, cocoa, and palm oil effluent samples were 5.4, 6.4, and 4.4, respectively. The mean values of temperature of cassava, cocoa, and palm oil effluent samples were 30.2, 28.9, and 29.4 °C, respectively. The mean values of electrical conductivity in cassava, cocoa, and palm oil effluent samples were 1794.2, 473.1, and 572.2 µs/cm, respectively. Similarly, the mean values of total dissolved solids in cassava, cocoa, and palm oil effluent samples were 4635.1, 327.9, and 3728.3 mg/ml, respectively. The mean values of biochemical oxygen demand and chemical oxygen demand in cocoa effluent samples were lower than those observed in cassava and palm oil effluent samples. In addition, the mean values of total carbohydrate and ash content in palm oil effluent samples were higher than those observed in cassava and cocoa effluent samples. High levels of cyanide and oil were detected in cassava and palm oil effluent samples, respectively (Table 4).

Table 4. Physicochemical characteristics of effluent samples.

Parameters	Cassava effluent	Cocoa effluent	Palm oil effluent	FEPA Guideline
pH	5.4 ± 0.3^b	6.4 ± 0.5^a	4.4 ± 0.2^c	6-9
Conductivity (µs/cm)	1794.2 ± 0.9^a	473.1 ± 0.7^c	572.2 ± 0.6^b	750.5
Temperature (°C)	30.2 ± 0.2^a	28.9 ± 1.4^a	29.4 ± 0.2^a	25-28
Biochemical oxygen demand (mg/l)	1236.1 ± 12.1^b	22.2 ± 0.5^c	4362.0 ± 0.5^a	10
Chemical oxygen demand (mg/l)	1694.5 ± 14.0^b	98.7 ± 0.9^c	8615.1 ± 11.4^a	40
Total dissolved solids (mg/l)	4635.1 ± 1.4^b	327.9 ± 2.3^c	3728.3 ± 2.6^a	2000
Oil (mg/l)	ND	ND	9620.1 ± 3.4	10
Total carbohydrate (mg/l)	973.5 ± 3.0^b	629.1 ± 4.4^c	18443.1 ± 2.4^a	
Ash content (mg/l)	726.3 ± 0.5^b	6.8 ± 0.7^c	3928.1 ± 1.9^a	
Cyanide (mg/l)	21.0 ± 1.2	ND	ND	0.2

Key: ND = Non-detect; FEPA – Federal Environmental Protection Agency (1991); Data presented as Mean ± SD (n = 5), values in the same row with the same superscript are not significantly different ($p \leq 0.05$)

3.4 Bioremediation potential of isolates on cassava, cocoa, and palm oil effluents

In the bioremediation process of cassava effluents, the counts of bacteria, fungi, and their consortium in the treatments increased significantly ($p < 0.05$). The highest cell count was observed in the consortium (2.27×10^6 CFU/ml) followed by treatments containing *C. manihot* (1.59×10^6 CFU/ml) and *P. aeruginosa* (1.27×10^6 CFU/ml) (Table 5). As the bioremediation process progressed, the values of pH decreased steadily in all the treatments except the control, from slightly acidic to more acidic. In terms of the reduction of COD and BOD in the cassava effluents, the consortium exhibited the highest potential (COD – 39%; BOD – 35%) followed by treatments containing *C. manihot* and *P. aeruginosa* (Figure 4). Treatments containing bacterial isolates demonstrated higher bioremediation potential of cassava effluents compared to those containing fungal isolates.

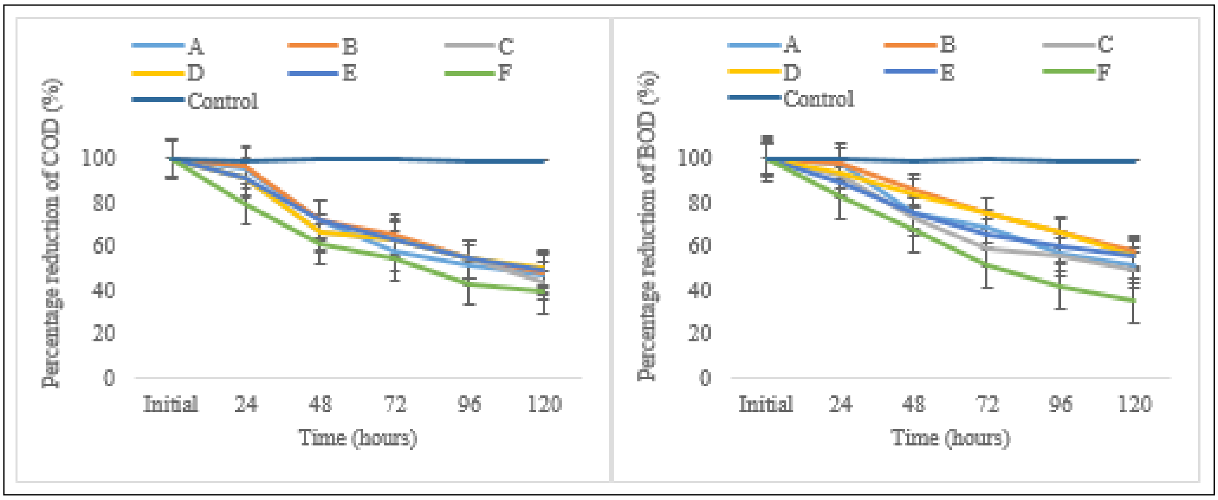

Figure 4. Percentage reduction of COD and BOD in cassava effluents over time (Treatments: A – *P. aeruginosa*; B – *M. morganii*; C – *C. manihot*; D – *S. cerevisiae*; E – *C. tropicalis*; F – consortium).

Table 5. Bioremediation potential of isolates on cassava effluents.

Treatments	Parameters	Time (h)					
		Initial	24	48	72	96	120
A	Count (×10^4 CFU/ml)	-	11	31	53	92	127
	pH	5.4	5.3	5.1	4.9	4.7	4.3
	Temperature (°C)	30.2	32.2	33.5	33.2	33.6	33.8
B	Count (×10^4 CFU/ml)	-	12	22	39	61	82
	pH	5.4	5.2	4.8	4.8	4.7	4.5
	Temperature (°C)	30.2	32	33.0	33.6	33.2	33.2
C	Count (×10^4 CFU/ml)	-	15	48	67	104	159
	pH	5.4	5.2	5.0	4.3	4.3	3.9
	Temperature (°C)	30.2	32.1	34.4	34.5	34.8	34.9
D	Count (×10^4 SFU/ml)	-	8	20	28	43	67
	pH	5.4	5.0	4.7	4.4	4.2	4.0
	Temperature (°C)	30.2	33.3	33.5	33.6	33.6	33.8
E	Count (×10^4 SFU/ml)	-	8	21	37	51	72
	pH	5.4	5.0	4.8	4.5	4.1	3.9
	Temperature (°C)	30.2	32.8	33.0	32.8	33.2	33.2
F	Count (×10^4 CFU/ml)	-	31	79	133	176	227
	pH	5.4	5.0	4.8	4.31	4.26	3.9
	Temperature (°C)	30.2	33.2	34.4	35.0	36.1	36.7
Control	Count	-	-	-	-	-	-
	pH	5.4	5.4	5.4	5.4	5.4	5.4
	Temperature (°C)	30.2	30.2	29.9	30	29.8	29.7

Key: Treatments: A – *P. aeruginosa*; B – *M. morganii*; C – *C. manihot*; D – *S. cerevisiae*; E – *C. tropicalis*; F – consortium

In the bioremediation process of cocoa effluents, the counts of bacteria, fungi, and their consortium in the treatments also increased significantly ($p < 0.05$). The highest cell count was observed in the consortium (1.43×10^6 CFU/ml) followed by treatments containing *P. fluorescence* (9.8×10^5 CFU/ml) and *L. delbrueckii* (8.4×10^5 CFU/ml). As the bioremediation process progressed, the values of pH decreased steadily in all the treatments except the control, from near neutral to slightly acidic (Table 6). In terms of the reduction of COD and BOD in the cocoa effluents, the consortium exhibited the highest potential (COD – 32%; BOD – 65%) followed by treatments containing *L. delbrueckii* and *P. fluorescence* (Figure 5). Similarly, treatments containing bacterial isolates demonstrated higher bioremediation potential of cocoa effluents compared to those containing fungal isolates.

Table 6. Bioremediation potential of isolates on cocoa effluents.

Treatments	Parameters	Time (h)					
		Initial	24	48	72	96	120
A	Count (×10^4 SFU/ml)	3	7	17	24	37	46
	pH	6.4	6.4	5.9	5.6	5.1	4.8
	Temperature (°C)	29	29	30	29	29	29
B	Count (×10^4 SFU/ml)	3	4	9	13	17	22
	pH	6.4	6.2	5.6	4.7	4.6	4.5
	Temperature (°C)	29	29	30	29.7	29.8	29.7
C	Count (×10^4 CFU/ml)	3	13	23	46	59	84
	pH	6.4	6.4	5.4	4.6	4.6	4.3
	Temperature (°C)	29	29	30	30	29.5	29.6
D	Count (×10^4 CFU/ml)	3	12	27	49	71	98
	pH	6.4	6.4	5.8	4.8	4.8	4.5
	Temperature (°C)	29	29	30	29.7	29.8	29.9
E	Count (×10^4 CFU/ml)	5	23	47	69	93	143
	pH	6.4	6.2	5.2	4.8	4.8	4.2
	Temperature (°C)	29	29	30	29.7	29.8	29.9
Control	Count	-	-	-	-	-	-
	pH	6.4	6.5	6.2	6.4	6.4	6.4
	Temperature (°C)	29	29	29	29	29	28.9

Key: Treatments: A – *S. cerevisiae*; B – *P. notatum*; C – *L. delbrueckii*; D – *P. fluorescence*; E – consortium

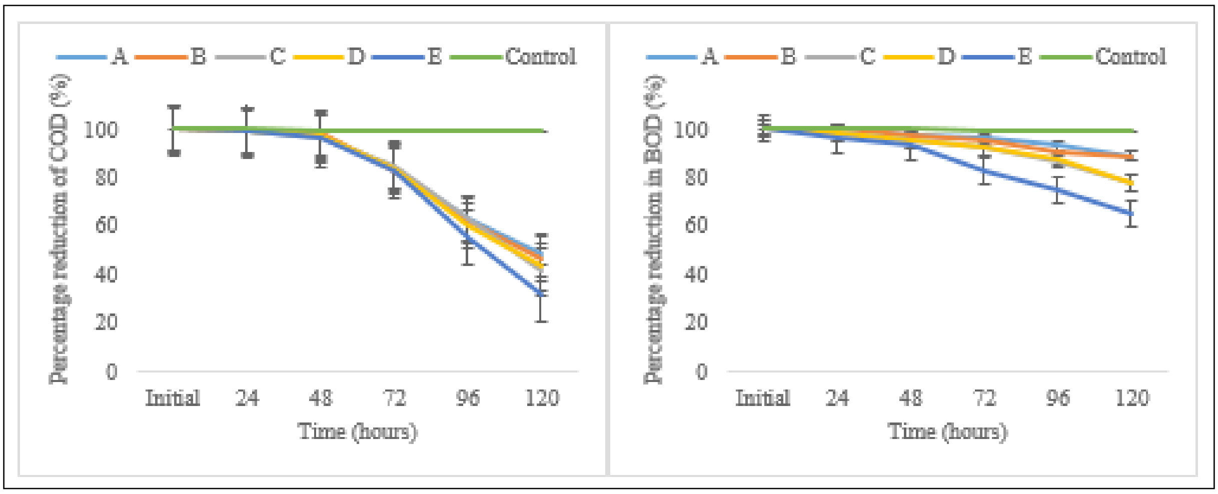

Figure 5. Percentage reduction of COD and BOD in cocoa effluents over time (Treatments: A – *S. cerevisiae*; B – *P. notatum*; C – *L. delbrueckii*; D – *P. fluorescence*; E – consortium).

In the bioremediation process of palm oil effluents, the counts of bacteria, fungi, and their consortium in the treatments increased significantly ($p < 0.05$). Again, the highest cell count was observed in the consortium (1.27×10^6 CFU/ml) followed by treatments containing *M. luteus* (8.8×10^5 CFU/ml) and *P. aeruginosa* (5.6×10^5 CFU/ml). As the bioremediation process progressed, the values of pH decreased slightly in all the treatments except the control (Table 7). In terms of the reduction of COD and BOD in the palm oil effluents, the consortium exhibited the highest potential (COD – 39%; BOD – 29%) followed by treatments containing *P. notatum* and *M. luteus* (Figure 6). Although the treatment containing *P. notatum* had the least count after 120 h, it demonstrated a higher bioremediation potential of palm oil effluents compared to those containing bacterial isolates.

Table 7. Bioremediation potential of isolates on palm oil effluents.

Treatments	Parameters	Time (h)					
		Initial	24	48	72	96	120
A	Count ($\times 10^4$ CFU/ml)	3	7	13	21	34	47
	pH	4.4	4.2	4.1	4.3	4.3	4.3
	Temperature (°C)	29.4	29.5	29.7	29.7	29.8	29.9
B	Count ($\times 10^4$ CFU/ml)	3	13	23	49	66	88
	pH	4.4	4.2	4.1	4.1	4.1	4.1
	Temperature (°C)	29.4	29.7	29.7	29.9	30.2	30.6
C	Count (CFU/ml)	3	9	13	25	37	56
	pH	4.4	4.4	4.4	4.3	4.3	4.2
	Temperature (°C)	29.4	29.5	29.5	29.6	29.7	29.8
D	Count (SFU/ml)	3	4	13	23	31	46
	pH	4.4	4.2	4.1	4.1	4.1	4.0
	Temperature (°C)	29.4	29.8	29.9	30.1	30.6	30.7
E	Count ($\times 10^4$ CFU/ml)	3	21	44	79	92	127
	pH	4.4	4.2	4.1	4.0	3.9	3.8
	Temperature (°C)	29.4	29.8	30.3	30.7	31.0	31.1
Control	Count	-	-	-	-	-	-
	pH	4.4	4.4	4.4	4.4	4.4	4.4
	Temperature (°C)	29.4	29.0	28.7	28.4	28.5	28.6

Key: Treatments: A – *P. vermicola*; B – *M. luteus*; C – *P. aeroginosa*; D – *P. notatum*; E – consortium

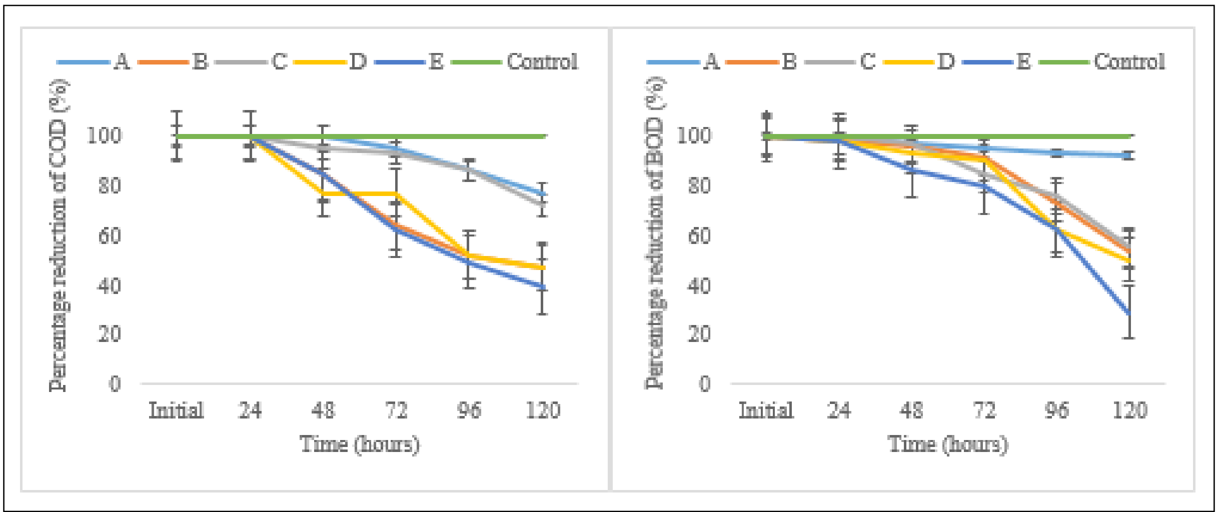

Figure 6. Percentage reduction of COD and BOD in palm oil effluents over time (Treatments: A – *P. vermicola*; B – *M. luteus*; C – *P. aeroginosa*; D – *P. notatum*; E – consortium).

4. Discussion

The bioremediation potentials of indigenous bacteria and fungi in some agro-based industrial effluents were examined. The total viable counts of bacteria and fungi that were higher in palm oil effluents compared to the counts in cassava and cocoa effluents may be a result of higher concentrations of carbohydrates, ash, and oil in the palm oil effluents. The presence of cyanide in cassava effluents may have also contributed to the observed lower counts of bacteria and fungi (Ogboghodo *et al*., 2006; Dash *et al*., 2009). The array and range of counts of bacteria and fungi observed in this study were similar to those reported by Akinnusotu and Arawande (2016) and Enerijiofi *et al.* (2017). The high prevalence of *Bacillus*, *Lactobacillus*, *Pseudomonas,* and *Aspergillus* observed in cassava, cocoa, and palm oil effluents may likely be because of the favorable pH and available nutrients in the effluents.

Enerijiofi *et al.* (2017) had earlier reported that growth media must be supplemented to isolate indigenous microorganisms from effluent. This may be responsible for the higher load of bacteria and fungi observed on mineral salt medium (MSM) supplemented with the cassava and cocoa effluents compared with their growth on general-purpose media. However, this trend was not observed on mineral salt medium (MSM) supplemented with palm oil effluents, as a load of bacteria and fungi was lower than those on general-purpose media. Again, this may be a result of higher concentrations of carbohydrates, ash, and oil in the palm oil effluents. Bacteria and fungi that demonstrated higher rates of utilization of cassava, cocoa, and palm oil effluents suggest that the isolates had the potential in utilizing effluents as their carbon and energy source (Enerijiofi *et al*., 2017; Shah, 2017; Ganapathy *et al*., 2019).

The pH of cocoa effluent was within the reference standard while the pH of cassava and palm oil effluents was lower than the standard value set by FEPA (1991) on National Guidelines and Standards for Industrial Effluents in Nigeria. The low pH of cassava effluent may be due to the high cyanide content while the low pH observed in palm oil may be a result of organic and free fatty acids arising from the partial degradation of palm fruits before processing. The electrical conductivity in cassava effluents that was above the recommended standard FEPA (1991) may be due to high levels of anions in cassava tubers (Enerijiof *et al*., 2017). The concentration of total dissolved solids in cassava and palm oil effluents was above FEPA standard (1991), this may be due to the contribution of inherent components of the product to the effluents during processing (Wu *et al*., 2009; Enerijiofi *et al.* 2017).

The temperature of all the effluents was higher than the standard limit, this could be a result of the temperature of the environment, especially in the tropics. The observed temperature is optimum for microbial growth and may be responsible for the array of bacteria and fungi isolated from the effluents (Akinnusotu and Aranwade, 2016; Shah, 2017). The levels of BOD and COD of all the effluents were above the standard limit, this may be attributed to the presence of high organic matter in the effluents (Okunade and Adekalu, 2013). The effluents may cause environmental problems such as eutrophication, water pollution loss of biodiversity, and soil fertility when discharged directly into the environment without treatment (Ogboghodo *et al*., 2006; Ezeigbo *et al*., 2014; Igbinosa, 2015). Bioremediation entails utilizing microorganisms to clean up contaminants in the environment and some of the microorganisms employed include members of the genera *Pseudomonas, Flavobacterium, Bacillus*, and *Serratia* (Enerijiofi *et al.,* 2017). The process is cost-effective and immobilizes contaminants in a manner that protects human health and the environment (Wu *et al.,* 2009; Bala *et al*., 2014). In the bioremediation process, the highest cell counts were observed in the treatments containing the consortium of indigenous microorganisms, this is in agreement with the report of Jameel and Olanrewaju (2011) where the authors observed that the right consortium is central to optimizing degradation activity. Counts of *C. manihot, P. aeruginosa,* and *M. morganii* were higher than other microorganisms in cassava effluents, counts of *P. fluorescence* and *L. delbrueckii* were higher than others in cocoa effluents, whereas, counts of *M. luteus* and *P. aeruginosa* were higher than others in palm oil effluents. These growth patterns suggest that the isolates and consortium effectively utilized the effluent as nutrient or energy sources (Vijayaraghavan *et al*., 2007; Jameel and Olanrewaju, 2011; Enerijiofi *et al*., 2017).

The pH of all the effluents was reduced during the bioremediation process with indigenous microbial isolates and their consortium. This may be a result of the conversion of the organic compounds in the effluents to organic acids (Bala *et al.,* 2014; Jameel and Olanrewaju, 2011; Enerijiofi *et al*., 2017). Treatments containing the consortium of isolates exhibited the highest reduction in BOD and COD values in all the effluents. Improved pollutants remediation using bacterial and fungal consortiums had previously been reported (Jameel and Olanrewaju, 2011). In cassava effluents, treatments containing *C. manihot* and *P. aeruginosa* reduced the BOD and COD more effectively than other isolates. In cocoa effluents, *L. delbrueckii* and *P. fluorescence* reduced the BOD and COD more effectively than other isolates, whereas in palm oil effluents *P. notatum* and *M. luteus* were more effective than other isolates.

5. Conclusions

The findings of this study demonstrate the bioremediation potentials of *C. manihot, L. delbrueckii, and P. notatum* and their consortium on cassava, cocoa, and palm oil effluents, respectively. The mean percentage reduction of COD and BOD in the three effluents was approximately 37% and 43%, respectively. Increasing the concentration of the isolates in the treatments and improving the strains of the isolates may increase the efficiency of the bioremediation process. Treatment of agro-based industrial effluents with these promising isolates before discharge may offer an improved way of eliminating organic contaminants in the receiving soils, rivers, or streams, thereby protecting human and environmental health.

Acknowledgment:

The authors are grateful to the Department of Microbiology, School of Life Sciences, The Federal University of Technology, Akure, Ondo State, Nigeria for providing appropriate support in terms of equipment and laboratory used for the study.

References

Adekunle, A.S. and Eniola, I.T.K. (2008). Impact of industrial effluents on quality of segment of Asa River within an industrial estate in Ilorin, Nigeria. New York Science Journal, 1, (1): 17B21.

Akinnusotu A. and Aranwade J.O. (2016). Qualities of effluent from three cocoa processing factories in Ondo State, southwest Nigeria. International Journal of Environment and Bioenergy, 11(1): 24-35.

Arimoro, F.O., Iwegbue, C.M.A. and Enemudo, B.O. (2008). Effects of cassava effluent on benthic macroinvertebrate assemblages in a tropical stream in southern Nigeria. Acta Zoologica Lituanica, 18: 147–156.

Bala, J.D., Lalung, J. and Ismail N. (2014). Biodegradation of palm oil mill effluent (POME) by bacterial strains. International Journal of Scientific Research Publication, 4(3): 2250–3153.

Dash, R., Gaur, A and Balomajumder, C. (2009). Cyanide in industrial wastewaters and its removal: A review on biotreatment. Journal of Hazardous Materials. 152: 387–396.

Enerijiofi, K.E., Ekhaise, F.O. and Ekomabasi, I.E. (2017). Biodegradation potentials of cassava mill effluent (CME) by indigenous microorganisms. Journal of Applied Sciences and Environmental Management, 21(6): 1029-1034.

Ethan, J.N., Richard, W.M., Michael, G.K. (2003). The effect of industrial effluent on an urban stream benthic community: water quality vs. habitat quality. Environmental Pollution, 123(1):1-13.

Ezeigbo, O.R., Ike-Amadi, C.A., Okeke, U.P. and Ekaiko, M.U. (2014). The effect of cassava mill effluent on soil microorganisms in Aba, Nigeria. International Journal of Current Research in Biosciences and Plant Biology, 1(4): 21-26.

FEPA (Federal Environmental Protection Agency). (1991). Guidelines to standards for environmental pollution control in Nigeria, FG Press, Lagos, Nigeria. 238pp.

Ganapathy, B., Yahya, A. and Ibrahim, N. (2019). Bioremediation of palm oil mill effluent (POME) using indigenous *Meyerozyma guilliermondii*. Environmental Science Pollution Research, 26: 11113–11125.

Igbinosa, E.O. (2015). Effect of cassava mill effluent on biological activity of soil microbial community. Environmental Monitoring and Assessment, 187:418-427.

Jameel A.T. and Olanrewaju A.A. (2011). Aerobic biodegradation of oil and grease in palm oil mill effluent using a consortium of microorganisms. In: Alam MDZ, Jameel AT, Amid A (eds) Current research and development in biotechnology engineering at International Islamic University Malaysia (IIUM) Vol. III. II UM Press, Kuala Lumpur, pp 43–51.

Kanu, I. and Achi, O.K. (2011). Industrial effluents and their impact on water quality of receiving rivers in Nigeria. Journal of Applied Technology in Environmental Sanitation, 1(1): 75-86.

Ogboghodo, I.A., Oluwafemi, A.P. and Ekeh, S. M. (2006). Effects of polluting soil with cassava mill effluent on the bacteria and fungi populations of a soil cultivated with maize. Environmental Monitoring and Assessment, 116: 419–425.

Okunade, D.A. and Adekalu, K.O. (2013). Physicochemical analysis of contaminated water resources due to cassava wastewater effluent disposal. European Journal of Science and Technology, 2:75-84.

Osunbitan, J.A., Olushina, J.O., Jeje, J.O., Taiwo, K.A., Faborode, M.O. and Ajibola, O.O. (2000). Information on micro-enterprises involved in cassava and palm oil processing in Osun and Ondo States of Nigeria. Technovation, 20(10): 577-585.

Shah M.P. (2017). Environmental bioremediation of industrial effluent. Journal of Molecular Biology and Biotechnology, 165(1): 382-395.

Vijayaraghavan, K., Ahmad, D., Ezani Bin Abdul Aziz, M. (2007). Aerobic treatment of palm oil mill effluent. Environmental Management, 82(1): 24–31.

Wu, T.Y., Mohammad, A.W., Jahim, J.Md. and Anuar, N. (2009). A holistic approach to managing palm oil mill effluent (POME): Biotechnological advances in the sustainable reuse of POME. Biotechnology Advances, 27: 40–52.

المملكة الأردنية الهاشمية

صندوق دعم البحث العلمي

الجامعة الهاشمية

المجلة الأردنية لعلوم الأرض والبيئة

JJEES

مجلة علمية عالمية محكمة

المجلد (١٣) العدد (٤)

http:// jjees.hu.edu.jo/

ISSN 1995-6681

المجلة الأردنية لعلوم الأرض والبيئة

مجلة علمية عالمية محكمة

المجلة الأردنية لعلوم الأرض والبيئة : مجلة علمية عالمية محكمة ومفهرسة ومصنفة، تصدر عن عمادة البحث العلمي في الجامعة الهاشمية وبدعم من صندوق البحث العلمي - وزارة التعليم العالي والبحث العلمي، الأردن.

ترسل البحوث إلكترونيا إلى البريد الإلكتروني التالي:

رئيس تحرير المجلة الأردنية لعلوم الأرض والبيئة

jjees@hu.edu.jo

لمزيد من المعلومات والأعداد السابقة يرجى زيارة موقع المجلة على شبكة الانترنت على الرابط التالي:

www.jjees.hu.edu.jo

المملكة الأردنية الهاشمية   صندوق دعم البحث العلمي   الجامعة الهاشمية

JJEES

المجلة الأردنية لعلوم الأرض والبيئة

المجلد (13) العدد (4)

مجلة علمية عالمية محكمة تصدر بدعم من صندوق دعم البحث العلمي

ISSN 1995-6681   jjees.hu.edu.jo   كانون الأول 2022